DNA-TR-88-239-V1

LONG WAVE ATMOSPHERIC NOISE MODEL—PHASE I

Volume I—Lightning Occurrence Rates and Propagation Theory

C. R. Warber
L. R. Kies
E. C. Field, Jr.
Pacific-Sierra Research Corporation
12340 Santa Monica Boulevard
Los Angeles, CA 90025-2587

14 October 1988

Technical Report

CONTRACT No. DNA 001-87-C-0171

Approved for public release;
distribution is unlimited.

THIS WORK WAS SPONSORED BY THE DEFENSE NUCLEAR AGENCY
UNDER RDT&E RMC CODE B466D RB RB 00141 3200 25904D.

Prepared for
Director
Defense Nuclear Agency
Washington, DC 20305-1000

Destroy this report when it is no longer needed. Do not return to sender.

PLEASE NOTIFY THE DEFENSE NUCLEAR AGENCY, ATTN: CSTI, WASHINGTON, DC 20305-1000, IF YOUR ADDRESS IS INCORRECT, IF YOU WISH IT DELETED FROM THE DISTRIBUTION LIST, OR IF THE ADDRESSEE IS NO LONGER EMPLOYED BY YOUR ORGANIZATION.

DISTRIBUTION LIST UPDATE

This mailer is provided to enable DNA to maintain current distribution lists for reports. We would appreciate your providing the requested information.

☐ Add the individual listed to your distribution list.

☐ Delete the cited organization/individual.

☐ Change of address.

NAME: _____

ORGANIZATION: _____

OLD ADDRESS	CURRENT ADDRESS
_____	_____
_____	_____
_____	_____

TELEPHONE NUMBER: ( ) _____

SUBJECT AREA(s) OF INTEREST:

_____ _____

_____ _____

_____ _____

DNA OR OTHER GOVERNMENT CONTRACT NUMBER: _____

CERTIFICATION OF NEED-TO-KNOW BY GOVERNMENT SPONSOR (if other than DNA):

SPONSORING ORGANIZATION: _____

CONTRACTING OFFICER OR REPRESENTATIVE: _____

SIGNATURE: _____

CUT HERE AND RETURN

REPORT DOCUMENTATION PAGE

1a REPORT SECURITY CLASSIFICATION UNCLASSIFIED	1b RESTRICTIVE MARKINGS
2a SECURITY CLASSIFICATION AUTHORITY N/A since Unclassified	3 DISTRIBUTION/AVAILABILITY OF REPORT Approved for pubic release; distribution is unlimited.
2b DECLASSIFICATION/DOWNGRADING SCHEDULE N/A since Unclassified	
4 PERFORMING ORGANIZATION REPORT NUMBER(S) PSR Report 1877	5. MONITORING ORGANIZATION REPORT NUMBER(S) DNA-TR-88-239-V1
6a. NAME OF PERFORMING ORGANIZATION Pacific-Sierra Research Corporation 6b. OFFICE SYMBOL (if applicable)	7a. NAME OF MONITORINNG ORGANIZATION Director Defense Nuclear Agency
6c. ADDRESS (City, State, and ZIP Code) 12340 Santa Monica Blvd. Los Angles, CA 90025-2587	7b. ADDRESS (City, State, and ZIP Code) Washington, DC 20305-1000
8a. NAME OF FUNDING/SPONSORING ORGANIZATION 8b. OFFICE SYMBOL (if applicable) RAAE/Emmes	9. PROCUREMENT INSTRUMENT IDENTIFICATION NUMBER DNA 001-87-C-0171
8c. ADDRESS (City, State, and ZIP Code)	10. SOURCE OF FUNDING NUMBERS PROGRAM ELEMENT NO. 62715H; PROJECT NO. RB; TASK NO. RB; WORK UNIT ACCESSION NO. DH870171

11. TITLE (Include Security Classification)
LONG WAVE ATMOSPHERIC NOISE MODEL— PHASE I
Volume I— Lightning Occurrence Rates and Propagation Theory

12. PERSONAL AUTHOR(S)
Warber, Chris R.; Kies, Lynda R.; Field, Edward C., Jr.

13a. TYPE OF REPORT	13b. TIME COVERED	14. DATE OF REPORT (Year, Month, Day)	15. PAGE COUNT
Technical	FROM 870918 TO 881014	881014	112

16. SUPPLEMENTARY NOTATION
This work was sponsored by the Defense Nuclear Agency under RDT&E RMC Code B466D RB RB 00141 3200 25904D.

17. COSATI CODES			18. SUBJECT TERMS (Continue on reverse if necessary and identyfy by block number)
FIELD	GROUP	SUB-GROUP	ELF Communications, ELF Noise, Lightning, LF Communications, LF Noise, VLF Communications, VLF Noise
12	1		
4	2		

19. ABSTRACT (Continue on reverse if necessary and identify by block number)

Progress on a model that predicts how long wave atmospheric noise is affected by distortions in the earth-ionosphere waveguide caused by high-altitude nuclear bursts is described. When complete, the model will also represent worldwide noise under ambient conditions. The model comprises two submodels: source, which describes the occurrence rate of lightning flashes throughout the world; and propagation, which describes the propagation of energy radiated from centers of lightning activity. The new model is an improvement over existing ones in several respects. First, it uses recent data on the actual occurrence rate of lightning flashes as a function of time of day, latitude, and season. Such data circumvent the need to infer those rates from records of thunderstorm days. Second, it includes extremely low frequency and low frequency noise. Third, it uses new data on the altitude and orientation of individual strokes to model transverse-electric noise. Finally, the model incorporates new propagation algorithms that are nearly as accurate as full-wave algorithms,

20. DISTRIBUTION/AVAILABILITY OF ABSTRACT ☐ UNCLASSIFIED/UNLIMITED ☒ SAME AS REPORT ☐ DTIC USERS	21. ABSTRACT SECURITY CLASSIFICATION UNCLASSIFIED
22a. NAME OF RESPONSIBLE INDIVIDUAL Bennie F. Maddox	22b. TELEPHONE (Include Area Code) (202) 325-7042 22c. OFFICE SYMBOL DNA/CSTI

DD FORM 1473, 84 MAR 83 APR edition may be used until exhausted. All other editions are obsolete.

19. ABSTRACT (Continued)

but they reduce computer running time by as much as fivefold. It would be costly to recalculate mode parameters for the earth-ionosphere waveguide each time the model is exercised. Instead, attenuation rate, excitation factor, phase velocity, and eigencosine are precalculated and stored for a wide range of modes, frequency, ground conductivity, and spread-debris nuclear environments. Those data are of general interest and are presented in graphs in handbook format in Vol. II.

SUMMARY

This report describes progress on a model that predicts how long wave atmospheric noise is affected by distortions in the earth-ionosphere waveguide caused by high-altitude nuclear bursts. The model will also represent worldwide noise under ambient conditions. It comprises two submodels: the source submodel, which describes the occurrence rate of lightning flashes throughout the world; and the propagation submodel, which describes propagation of energy radiated from centers of lightning activity. The new model is an improvement over existing ones in several respects. First, it uses recent data on the actual occurrence rate of lightning flashes as a function of time of day, latitude, and season. Such data circumvent the need to infer those rates from records of thunderstorm days. Second, it includes extremely low frequency and low frequency noise. Third, it uses new data on the altitude and orientation of individual strokes to model transverse-electric noise. Finally, the model incorporates new propagation algorithms that are nearly as accurate as full-wave algorithms, but they reduce computer running time by as much as fivefold. It would be costly to recalculate mode parameters for the earth-ionosphere waveguide each time the model is exercised. Instead, attenuation rate, excitation factor, phase velocity, and eigencosine are precalculated and stored for a wide range of modes, frequency, ground conductivity, and spread-debris nuclear environments. Those data are of general interest and are presented graphically in handbook format in Vol. II.

PREFACE

This two-volume report describes progress made during the first year of a three-year Defense Nuclear Agency program to model long wave atmospheric noise in ambient and nuclear environments. Most of the year's efforts have been spent developing fast-running approximate algorithms to compute propagation of energy radiated by lightning flashes. That portion of the program is virtually complete. In addition, a literature search was conducted to locate recent data on the occurrence rate of worldwide lightning and on the altitude and orientation of typical discharges. Future work will include incorporating model current moments for several flash types, combining the propagation algorithms and source data into a cohesive noise model, and testing that model against available noise data.

CONVERSION ABLE

Conversion factors for U.S. Customary to metric (SI) units of measurement

MULTIPLY → / TO GET ←	BY → / BY ←	TO GET / DIVIDE
angstrom	1.000 000 X E -10	meters (m)
atmosphere (normal)	1.013 25 X E +2	kilo pascal (kPa)
bar	1.000 000 X E +2	kilo pascal (kPa)
barn	1.000 000 X E -28	meter^2 (m^2)
British thermal unit (thermochemical)	1.054 350 X E +3	joule (J)
calorie (thermochemical)	4.184 000	joule (J)
cal (thermochemical)/cm^2	4.184 000 X E -2	mega joule/m^2 (MJ/m^2)
curie	3.700 000 X E +1	*giga becquerel (GBq)
degree (angle)	1.745 329 X E -2	radian (rad)
degree Fahrenheit	$t_k = (t°f + 459.67)/1.8$	degree kelvin (K)
electron volt	1.602 19 X E -19	joule (J)
erg	1.000 000 X E -7	joule (J)
erg/second	1.000 000 X E -7	watt (W)
foot	3.048 000 X E -1	meter (m)
foot-pound-force	1.355 818	joule (J)
gallon (U.S. liquid)	3.785 412 X E -3	meter^3 (m^3)
inch	2.540 000 X E -2	meter (m)
jerk	1.000 000 X E +9	joule (J)
joule/kilogram (J/kg) (radiation dose absorbed)	1.000 000	Gray (Gy)
kilotons	4.183	terajoules
kip (1000 lbf)	4.448 222 X E +3	newton (N)
kip/inch^2 (ksi)	6.894 757 X E +3	kilo pascal (kPa)
ktap	1.000 000 X E +2	newton-second/m^2 ($N-s/m^2$)
micron	1.000 000 X E -6	meter (m)
mil	2.540 000 X E -5	meter (m)
mile (international)	1.609 344 X E +3	meter (m)
ounce	2.834 952 X E -2	kilogram (kg)
pound-force (lbs avoirdupois)	4.448 222	newton (N)
pound-force inch	1.129 848 X E -1	newton-meter (N-m)
pound-force/inch	1.751 268 X E +2	newton/meter (N/m)
pound-force/foot^2	4.788 026 X E -2	kilo pascal (kPa)
pound-force/inch^2 (psi)	6.894 757	kilo pascal (kPa)
pound-mass (lbm avoirdupois)	4.535 924 X E -1	kilogram (kg)
pound-mass-foot^2 (moment of inertia)	4.214 011 X E -2	kilogram-meter^2 ($kg-m^2$)
pound-mass/foot^3	1.601 846 X E +1	kilogram/meter^3 (kg/m^3)
rad (radiation dose absorbed)	1.000 000 X E -2	**Gray (Gy)
roentgen	2.579 760 X E -4	coulomb/kilogram (C/kg)
shake	1.000 000 X E -8	second (s)
slug	1.459 390 X E +1	kilogram (kg)
torr (mm Hg, 0° C)	1.333 22 X E -1	kilo pascal (kPa)

*The becquerel (Bq) is the SI unit of radioactivity; 1 Bq = 1 event/s.
**The Gray (Gy) is the SI unit of absorbed radiation.

TABLE OF CONTENTS

LIST OF ILLUSTRATIONS

LIST OF ILLUSTRATIONS (Concluded)

LIST OF TABLES

SECTION 1
INTRODUCTION

Before predictions can be made about how well long-wave communication links would perform in nuclear environments, it is necessary to know how those environments affect atmospheric noise as well as communication signals. Because no data exist for atmospheric noise under nuclear-disturbed conditions, a predictive noise model must be developed that accounts for distortions in the earth-ionosphere waveguide caused by high-altitude nuclear bursts. That model must, of course, also accurately represent worldwide noise under ambient conditions. This report describes Pacific-Sierra Research Corporation's (PSR) progress on such a model.

Although man-made or extraterrestrial sources might contribute to long-wave noise at certain times or locations, the model is based on the assumption that long-wave noise is caused solely by lightning, which radiates strongly in the extremely low frequency (ELF), very low frequency (VLF), and low frequency (LF) bands. The model therefore consists of two submodels. The first, the source submodel, describes the occurrence rate of lightning flashes throughout the world and the electromagnetic radiation from those flashes. The second, the propagation submodel, describes how the energy radiated from numerous worldwide centers of lightning activity propagates in the earth-ionosphere waveguide to the location of a long-wave receiver.

Two decades ago, the Westinghouse Georesearch Laboratory (WGL) [1972] used the structure just described to develop a model to predict ambient VLF noise throughout the world. The WGL model was state of the art at the time of its development, but is now obsolete in several respects. First, data on actual lightning flash occurrence rates were scarce, so WGL inferred the rates from records of thunderstorm days (TD), thus introducing an inaccuracy of unknown magnitude. Second, WGL modeled only radiation and propagation at frequencies between 10 and 30 kHz, thus omitting ELF and LF noise of importance to systems deployed during the past two decades. Third, the understanding of

lightning flash structure has advanced over the past 20 years. Fourth, the WGL model neglected horizontal lightning and hence omitted transverse electric (TE) noise, which is important for airborne receivers. Finally, the propagation algorithms used by WGL are crude by present-day standards, particularly when the ground or ionosphere changes along the direction of propagation; and they cannot account for ionospheric disturbances.

Section 2 of the present report describes the results of a literature search to locate data on the actual occurrence rate of lightning strokes as a function of latitude, time of day, and season. Such data circumvent the need to infer lightning occurrence statistics from TDs, and therefore remove a major uncertainty from the modeling process. Section 2 also describes recent data on the structure, elevation, and orientation of individual strokes. Ongoing lightning studies will provide more data in the future. The PSR model will be constructed so such improved data can be incorporated easily.

Section 3 and Appendix A describe the propagation algorithms that will be used in the model. It extends the work of Warber and Field [1987], who developed approximate methods to calculate coupling between waveguide modes over geologically complex regions like Canada and Greenland. They took advantage of the relatively slow lateral variations of conductivity, and applied a high-order Wentzel-Kramers-Brillouin (WKB) approximation. Such approximate methods are necessary because full-fledged propagation codes such as WAVEGUID (developed by the Naval Ocean Systems Center, San Diego, California) and WAVEPROP (developed by PSR) would require excessive computer time if used for a worldwide noise model treating propagation between hundreds of sources and receiver locations. Whereas Warber and Field addressed lateral transitions in ground conductivity, the present report treats changes in the waveguide height, such as between an undisturbed and nuclear-disturbed region of the ionosphere. It also develops a simple method to account for the anisotropy in propagation caused by the geomagnetic field, thereby alleviating the need to perform separate and detailed calculations for each propagation direction under undisturbed nighttime propagation.

As an aid, we have collected the acronyms used in the report, their definitions, and the page on which they are first used in Appendix B. Appendix C is a similar list of all the symbols used in the mathematical derivation in the report.

Rather than perform full calculations each time the model is exercised, it is preferable to precalculate and store waveguide mode parameters for a wide range of frequency, ground conductivity, and spread-debris nuclear environments. Those parameters can be retrieved rapidly, when needed. The precalculation of attenuation rate, excitation factor, phase velocity, and eigen cosine for all important modes has been performed. Because such data are useful in their own right to analysts, they are presented graphically in handbook format in Vol. II of this report.

SECTION 2
LIGHTNING OCCURRENCE DATA

Lightning discharges are the major source of global radio-frequency (RF) noise. Different types of lightning, as well as different stages within a lightning discharge, radiate significantly different spectra. The noise source submodel therefore comprises three major elements: a representation of the number of lightning discharges for a given area during a specified interval; "modifiers," which are used to discriminate between the various types of lightning discharges; and "model flashes," which describe the typical power spectrum emitted by each lightning type.

Because of the large uncertainties inherent in the WGL data base, that model required a complicated mix of algorithms, modifiers, and ad hoc adjustments to produce agreement with experimental results. Satellite-borne instruments have recently been used to measure lightning occurrence rate and flash density, which provide the basis for a substantially improved source submodel. Besides replacing the obsolete data base, recent data will permit a modular set of data-base modifiers to be incorporated in the new model. Each modifier will be sequentially applied to the source to account for the influence of an individual parameter (for example, storm severity). Although data to quantify the effects of certain parameters--such as ocean versus land mass--are still scarce, we will use separate modular algorithms that account for each parameter, thereby allowing the modifiers to be easily updated. New model flashes will be based on up-to-date theories that account for the nonverticality of lightning channels, which is important since the new model must represent sources of both TE and transverse magnetic (TM) noise.

In order to define the terminology, we first review lightning processes. Much of this review is taken from current literature, such as Uman and Krider [1982] and Fitzgerald [1985]. We then describe the old WGL source maps and present the data on which the new source maps will be based. Finally, we describe both the old and new source

modifiers. Development of the emission spectra for the various lightning discharge components has not begun.

LIGHTNING DISCHARGE PROCESSES.

Lightning is a complex, propagating, gas breakdown process which results in a transient, high-current electrical discharge. Small volumes of intense space charge in the presence of a strong electric field appear to initiate the breakdown. A discharge typically neutralizes some tens of coulombs of cloud charge over a path length measured in kilometers. The total discharge, also called a "flash," is made up of various components, among which are several high-current pulses called "strokes." A stroke is defined as the movement of charge in a given direction. Each stroke acts as an individual RF source, so basic stroke types must be identified and modeled. The model flashes are made up of combinations of model strokes.

Lightning is often classified into one of two categories. Cloud-to-ground (C-G) discharges (also called earth flashes) have discharge channels that contact the earth. In-cloud (I-C) lightning channels do not reach the earth and are composed of several subtypes: intercloud (between two clouds); cloud-to-air (between a cloud and clear air); and intracloud (within a cloud), which is by far the most common. Past models have addressed only this last category of I-C lightning, because it is by far the most prevalent. We will reevaluate the assumption that cloud-to-air and intercloud lightning can be ignored.

The likelihood that a discharge will produce a channel to ground depends on: the intensity of the charged regions; the height of the charge separation aboveground; and the charge sign which initiates the breakdown. Other factors, such as updraft velocity, may also play a role. We discuss the development and phases of I-C and C-G lightning separately.

In-Cloud Lightning.

In-cloud lightning flashes occur between positive and negative pockets of space charge. Although the discharge can be initiated by either charge sign, positive regions initiate some 75 percent of all

I-C breakdowns. The discharge is thought to consist of one or more branched, continuously propagating "leaders." The leader breakdowns generate five or six recoil streamers (called "K-changes") when they contact regions of space charge opposite their own. The development of a typical I-C flash is depicted in Fig. 1.

A typical cloud discharge is commonly believed to neutralize 10 to 30 C of charge over a total path length of 5 to 10 km and last approximately 0.5 s. Data from recent studies of lightning channels performed by Richard et al. [1987] suggest that I-C flashes consist of many propagating leaders and may have total path lengths longer than the widely accepted 5 to 10 km. Cloud discharges have not been studied as extensively as discharges to ground, because they are not as hazardous to personnel and equipment. Furthermore, since the charged channels are at altitude, they are difficult to study. As a result, less is known about them than C-G discharges.

Cloud-to-Ground Lightning.

The "preliminary breakdown" phase of a C-G flash initiates in the cloud much the same way as an I-C discharge, except that most C-G flashes originate from regions of negative space charge. The channel then extends below cloud level and toward ground in a series of short luminous steps called the "stepped leader." As the leader nears the ground, the large potential at the leader tip induces a discharge channel originating from the ground. The two channels connect and the "main return stroke" discharges the entire ionized channel. After the return-stroke current has ceased to flow, the flash may end. If, however, "K processes" make additional charge available to the channel, a continuous "dart leader" may propagate down the primary portion of the residual first-stroke channel. The dart leader differs from the stepped leader in that it is usually not branched. The dart leader again initiates contact with the earth, resulting in another return stroke. Often several dart leaders and subsequent return strokes occur before the flash ends. A slow electric field change (called the "final phase") then restores the field in the vicinity of the discharge to ambient. Some leaders begin as dart leaders but

a. Step 1--"Preliminary breakdown leader." When leader contacts pocket of space charge of opposite sign,

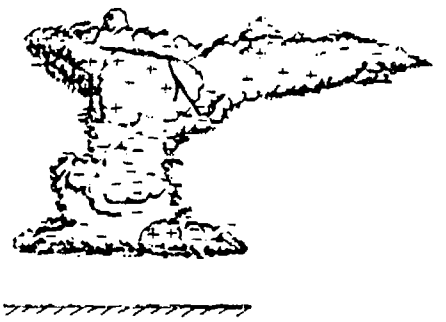

b. Step 2--a "recoil streamer" or "K-change" discharges the leader channel.

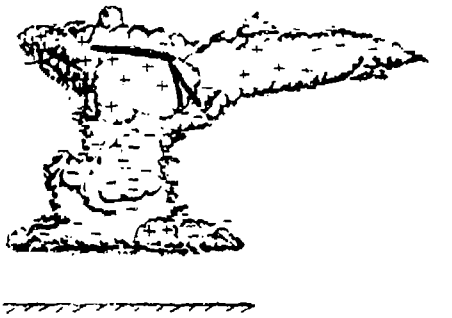

c. Step 3--Charge at source of channel causes leader to propagate further,

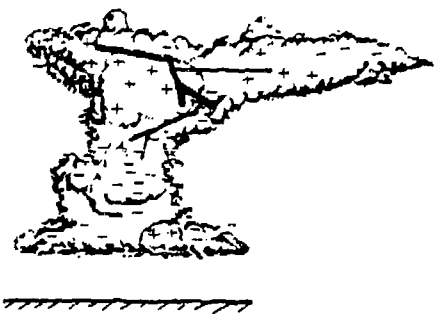

d. Step 4--resulting in second K-change which again discharges entire leader channel.

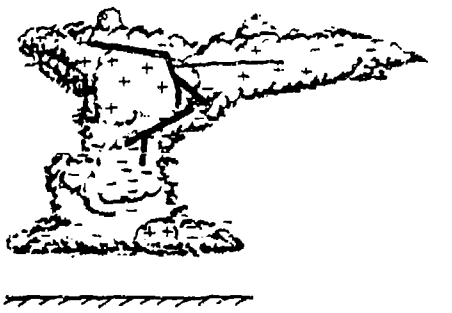

e. Steps 5 and 6--Process continues until the source charge is depleted. Notice multiple channels developing in steps 3 through 6.

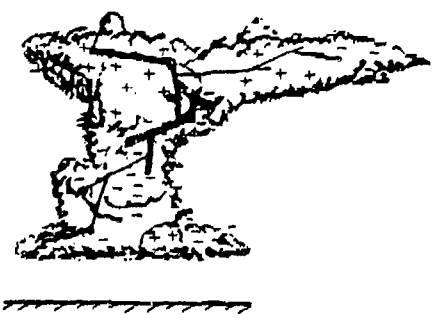

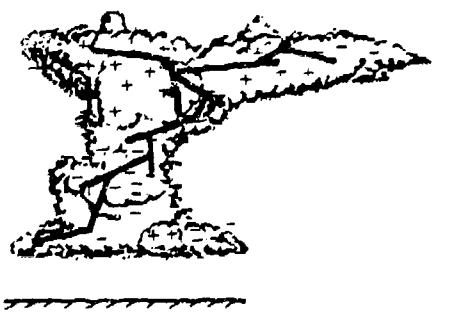

Note: Fine lines depict propagating leaders, heavy lines show discharges due to K-changes. Notice horizontal structure apparent in discharge path.

Figure 1. Typical I-C flash.

become stepped leaders as they near the ground. These processes are known as "dart-stepped leaders," which often precede the most intense return stroke in a flash. The phases of a C-G flash are shown in Fig. 2.

A typical C-G discharge lasts between 0.1 and 1.0 s, with the majority lasting approximately 0.5 s. Each stroke of the flash lasts about 1 ms, and the separation time between strokes is typically 40 to 80 ms. The return stroke generates the most energetic natural radio signals found on earth, with a spectral peak in the 4 to 8 kHz portion of the VLF band. Although most flashes neutralize negative cloud charge, positive flashes also occur. The duration and intensity of positive flashes are usually much greater than for negative discharges. Two model flashes therefore may be required to describe C-G discharges.

NOISE SOURCE MAPS.

The noise source map specifies the number of lightning discharges per unit area over the surface of the earth. Maps are prepared for monthly or seasonal periods, and for specific time periods over the course of a day. The well-known CCIR 322 [1963] set the standard as six 4-h daily time blocks and four seasons. We next review the WGL source maps, then present the data and format for the new global lightning occurrence (GLO) maps.

WGL Thunderstorm Day Maps and Conversion Algorithms.

The WGL source submodel is based on TD maps that depict the number of days in which thunder is heard in a particular region. The TD data were provided by the World Meteorological Organization (WMO). The WGL converted other types of data into TDs to improve the accuracy of the WMO maps, particularly in regions where data were scarce. The model also incorporated an algorithm which attempted to relate the number of TDs in a month to a total number of lightning discharges. Since the distribution of thunderstorms over the course of a day is not uniform, a table of hourly diurnal modifiers was then applied to allocate the percentages of a day's discharges to each hourly time block.

a. Step 1--"Preliminary breakdown" occurs within the cloud.

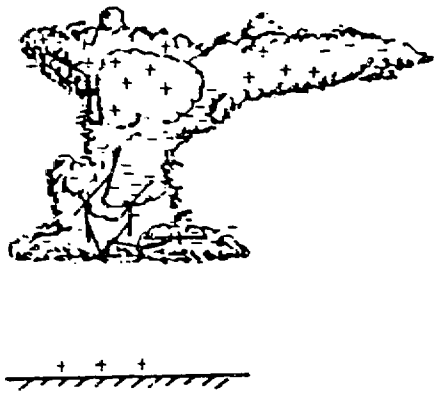

b. Step 2--The negatively charged "stepped leader" progresses from cloud toward ground.

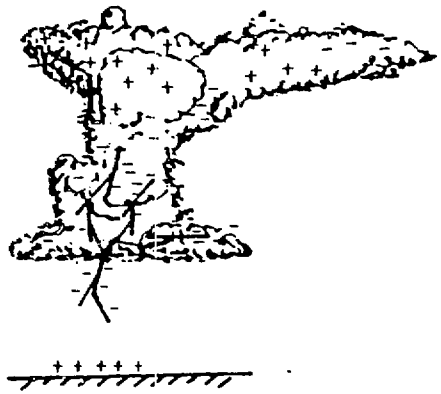

c. Step 3--As leader tip nears ground, an upward-moving positive streamer initiates.

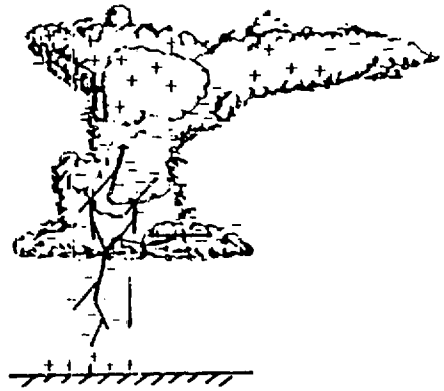

d. Step 4--Contact between the two channels results in the main "return stroke" which discharges the entire ionized channel.

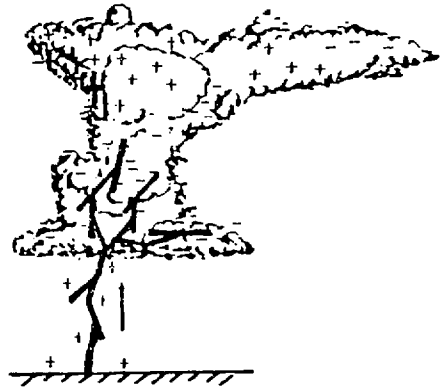

e. Step 5--K-changes make additional cloud charge available at the top of the leader channel,

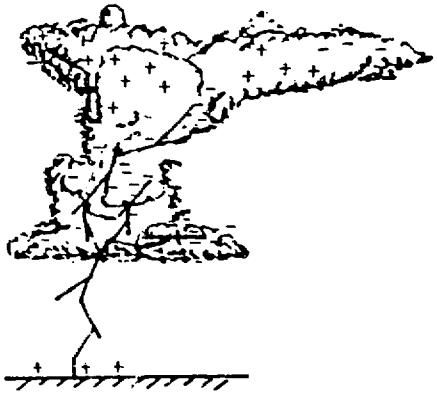

f. Step 6--causing a "dart leader" which follows the main path of the previous stepped leader channel.

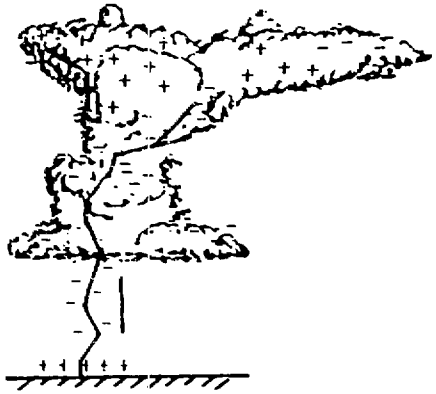

g. Step 7--Contact with the earth results in a subsequent "return stroke".

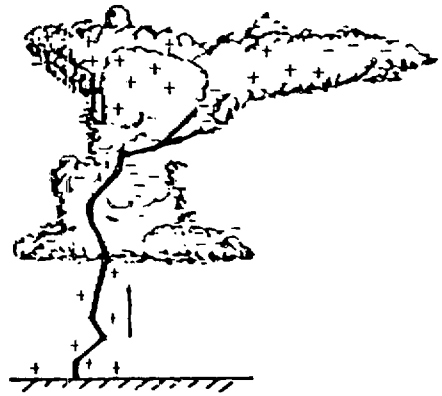

h. Steps 5-7--Repeat until all available cloud charge is neutralized. The "final phase" restores the ambient electric field.

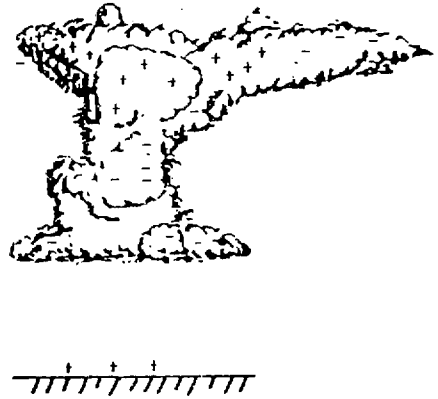

Note: Arrows indicate direction of stroke progression.

Figure 2. Typical C-G flash.

The WGL maps consisted of global contours of the number of TDs occurring each month. An empirical relationship (admitted by WGL to be imprecise) was proposed to convert TDs to the number of lightning flashes per square kilometer per month. That relationship was

$$N_{\ell d} = 0.06\ N_{TD}^{1.5} \qquad (1)$$

where $N_{\ell d}$ = number of lightning discharges/square kilometer/month,

N_{TD} = number of thunderstorm days/month.

The maps were divided into sectors of 5 deg latitude by 5 deg longitude. The number of lightning discharges for each sector (on each monthly map) was calculated, as was the centroidal location of the lightning. Each sector was then modeled by a single noise transmitter located at the lightning centroid.

Although once the only format for worldwide data available, the TD is not a good measure of lightning activity. Empirical relations exist for the average number of lightning flashes that occur in a typical storm, but those relationships could not be used because the TD does not specify the number of storms per day. The WGL attempted to correlate the number of thunderstorms per day with the density of TDs, but such a correlation is, at best, a crude approximation.

New Global Lightning Occurrence Maps.

The advent of satellites to measure lightning occurrence rates and flash density eliminates the need to use an algorithm to convert TDs to lightning occurrence. Since recent satellite studies have measured global lightning occurrence at all times of day, diurnal variations are incorporated into the raw data, and no diurnal model is required. We present samples of such satellite data and discuss their inclusion in the new source submodel.

OSO-2 and OSO-5 Satellites. The first satellite studies of lightning used optical intensity detectors, which limited observation

to periods of low light level. Initial studies, conducted with the OSO-2 and OSO-5 satellites, were reported by Vorpahl, Sparrow, and Ney [1970]. Observations were restricted to the 2000 to 0400 time block (around local midnight), and further limited to periods of new moon. Those studies recorded the positions of nighttime storms from February to September 1969 and January to July 1970. Figure 3 shows data from OSO-5. The points represent thunderstorms, which must be converted to lightning occurrence. This method is an improvement over the TD because it provides an actual storm count. Although not complete enough to fully replace the TD maps, these data will be used in conjunction with other recent measurements, described below.

Defense Meteorological Satellite Program. Subsequent measurements were made with more sophisticated equipment, carried aboard the Defense Meteorological Satellite Program (DMSP) flights 2 and 3. Although that study still used an optical intensity detector, it recorded actual lightning flash counts at local dawn and dusk. It thereby provided data for two time periods and eliminated the need for a conversion between thunderstorms and number of lightning flashes. Turman and Edgar [1982] accumulated the data into 10 deg latitude by 10 deg longitude sectors and presented it as sector flash rate maps for six periods: August, September-October, November-December, January-March, April, and May-June. Figure 4a* shows a sample of the flash rate maps at dawn for the month of April.

The sensors were operated in a triggered mode where two criteria had to be met. The irradiance had to (1) exceed 5×10^{-8} W/cm^2 (an unattenuated source power of 4×10^9 W) and (2) remain above that threshold for a minimum of five sample periods (a pulse length greater than 169 μs for the sampling rate of 31.2 kHz). The first criteria represent a very high trigger threshold, which was necessary to avoid false counts from sources other than lightning. Since the duration of a typical lightning flash is approximately 0.5 s, the counter could have been triggered several times by multiple strokes within a single flash. However because the trigger threshold was so high, only a very

*Longitudes are positive east of Greenwich and negative west, latitudes are positive north of the equator and negative south.

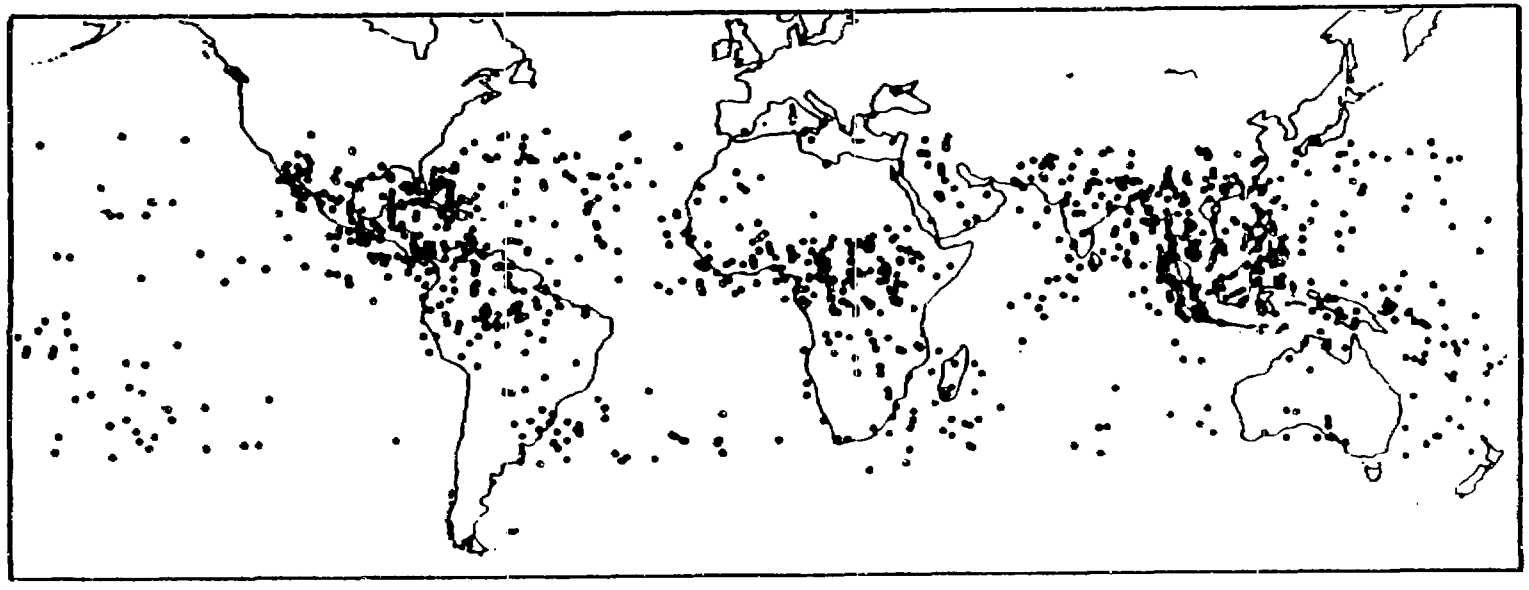

Source: Vorpahl, Sparrow, and Ney (1970).

Figure 3. Nighttime distribution of thunderstorms observed by OSO-5.

a. Dawn, April.

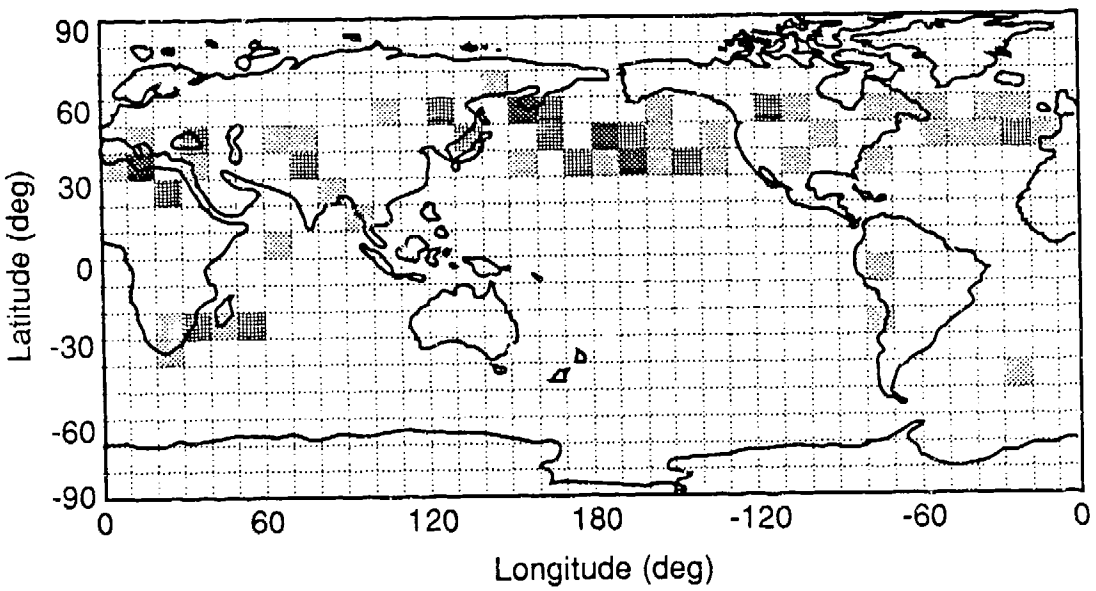

b. Dusk, April.

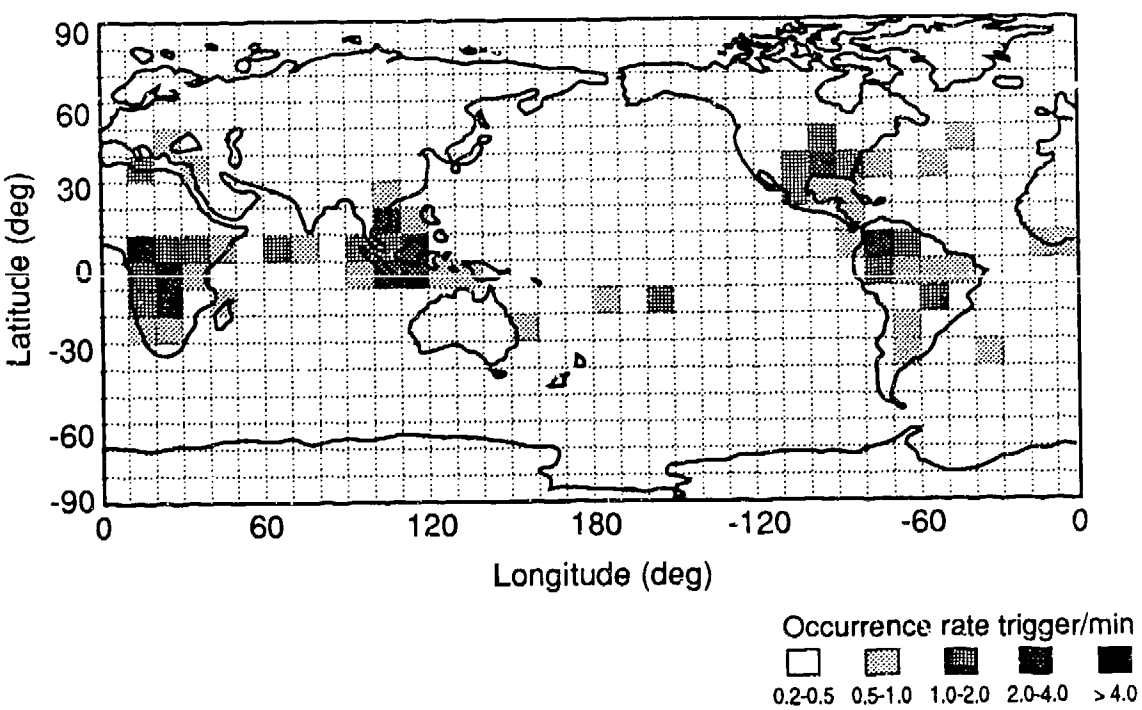

Figure 4. DMSP measured lightning flash occurrence rate maps for April at dawn and dusk.

small fraction of the total strokes triggered the counter. Since the first stroke in a flash is usually by far the strongest, when the sensor was triggered it was by a first stroke in most cases. Turman and Edgar found that in approximately 10 to 20 percent of the records, subsequent strokes had also triggered the counter. They decided that since less than 20 percent of the data presents any ambiguity between stroke counting and flash counting, they would ignore the distinction and assume that the sensor count rate was linearly related to the lightning *flash* rate.

To determine how many flashes were detected by the sensors, the data were correlated with published ground-based records at several locations. Various analyses yielded approximately the same correlation factor: the DMSP sensors detected 2 percent (± 1 percent) of all flashes (both I-C and C-G). Therefore to obtain the true flash rate, we must multiply DMSP map data by a factor between 33 and 100. Thus the bias introduced by the assumption that the sensor was triggered only by flashes is smaller than the error in the correlation factor. Because of the large spread of these data, they cannot completely replace the old WGL maps; however they can be used to improve weak areas of the old maps and update the diurnal modifiers.

The diurnal variation in thunderstorm location can be observed by comparing the "April, Dawn" map (Fig. 4a) with "April, Dusk" (Fig. 4b). Note that storms are fairly evenly distributed across the land and ocean masses at dawn, but concentrated over land masses at dusk. Storms during northern springtime (i.e., April) are concentrated over the Northern Hemisphere at dawn, and shift to equatorial regions at dusk. Global storm distribution during southern spring (northern fall), however, occurs primarily in the Southern Hemisphere at both dawn and dusk, as shown in Fig. 5. Southern spring distributions also reveal considerably less storm activity at dawn compared to dusk, whereas the total activity shown on the maps of northern springtime is approximately the same for both dawn and dusk. The January-March maps (Fig. 6) show a different diurnal distribution pattern than either Fig. 4 or Fig. 5. These three figures illustrate the wide variation in diurnal storm distribution patterns as well as

a. Dawn, November-December.

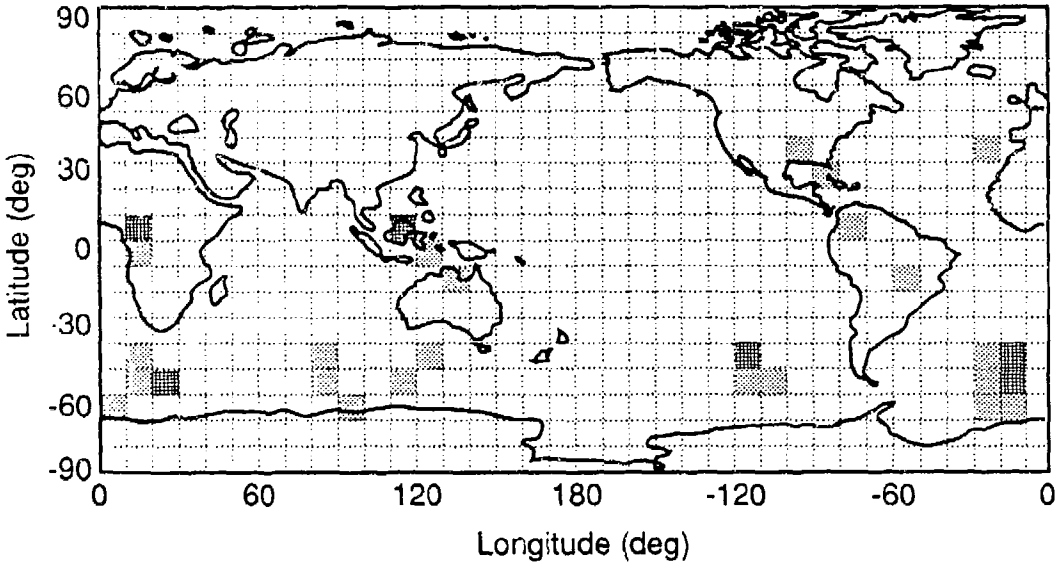

b. Dusk, November-December.

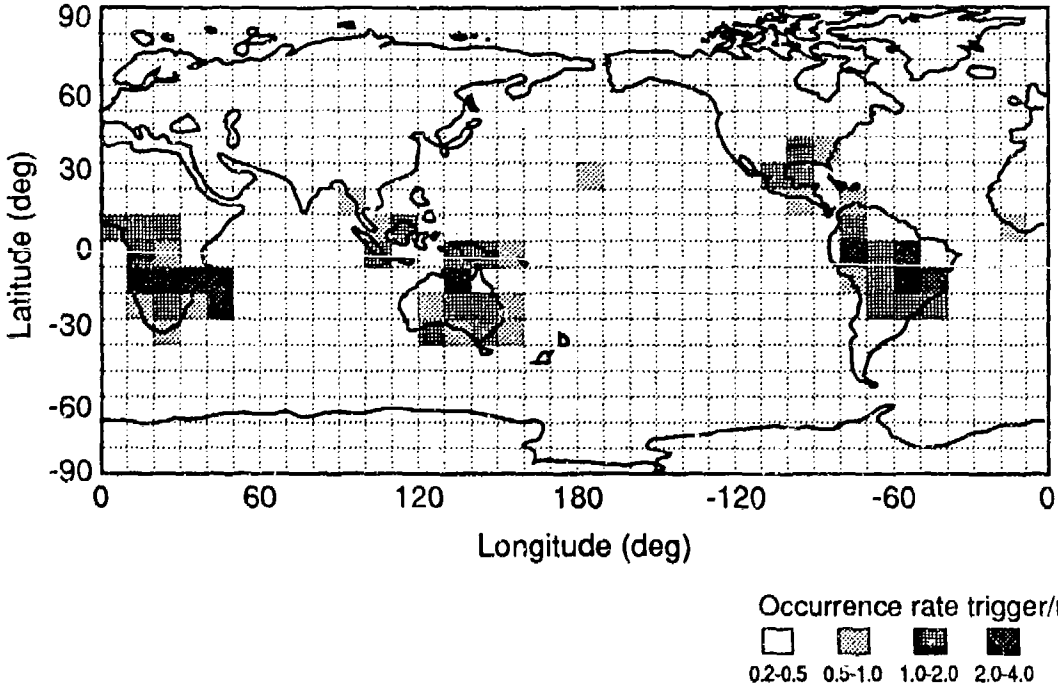

Figure 5. DMSP measured lightning flash occurrence rate maps for November through December at dawn and dusk.

a. Dawn, January-March.

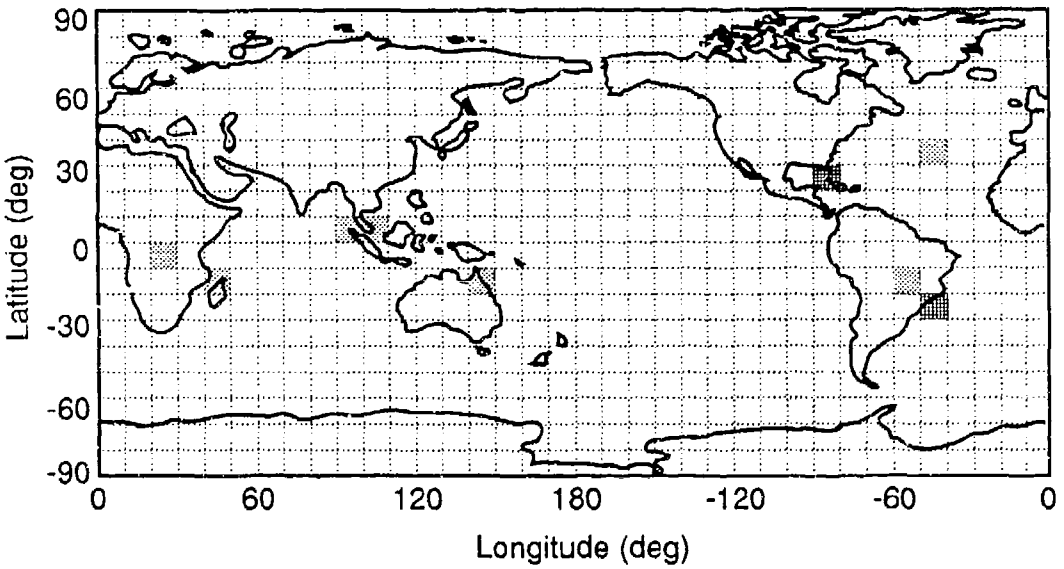

b. Dusk, January-March.

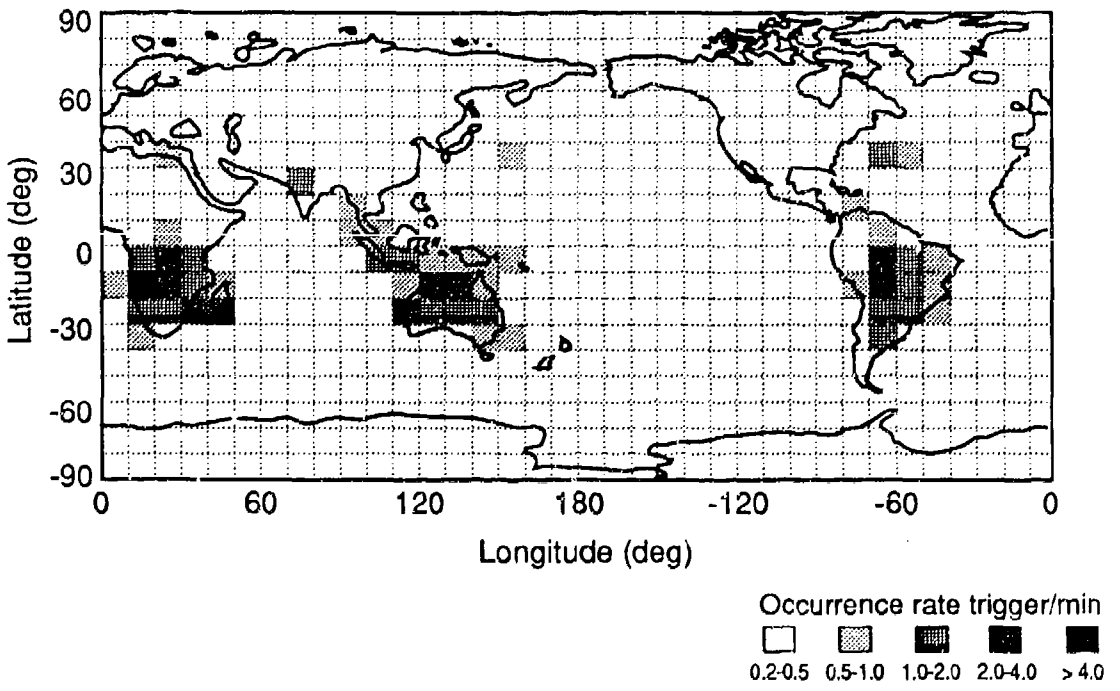

Figure 6. DMSP measured lightning flash occurrence rate maps for January through March at dawn and dusk.

seasonal variations. They emphasize the weakness of the old model, which attempted to infer diurnal distribution patterns from data measured at a limited number of locations.

Although still insufficient to allow complete replacement of the old TD source maps, the DMSP data, in conjunction with that from OSO-2 and OSO-5 will be used to broaden the data base provided by the following study.

Ionosphere Sounding Satellite. Identification of lightning strokes using radio receivers began in the early seventies. Wave-form signatures were identified that allow detection of lightning strokes at any time of day. This technique permits complete replacement of the TD concept with actual lightning flash density data. The Ionosphere Sounding Satellite (ISS-b) used four receivers at different frequencies to record the occurrence of global lightning from June 1978 to May 1980. Radio Research Laboratories, Tokyo, Japan, published that information, which, supplemented by the data described above, we will use to develop the new GLO maps. The new maps will replace the WGL TD maps and eliminate the need for the algorithms that (1) convert TDs to lightning occurrence and (2) account for the diurnal variation in lightning occurrence.

Lightning emissions are strongest at VLF, and the intensity decreases at greater frequencies. However, the use of a satellite platform for lightning observations requires detection frequencies higher than the critical frequency (f_c) of the ionosphere because waves having frequencies below f_c are reflected back toward the earth. Frequencies just above f_c are most desirable because the ionosphere cuts off noise from oblique angles and thus limits the field of view (FOV) to the area directly below the satellite. Limiting the FOV improves source location, although more orbits are required to obtain complete global coverage than are needed with a wide-angle receiver.

The ionosphere varies constantly, so f_c must be evaluated periodically while the data are being recorded. Only receivers operating above f_c can record a lightning event. Several frequencies around the nominal value of f_c were chosen for the onboard receivers so that one detector was usually operating at a frequency just above f_c. Those

frequencies used were 2.5, 5, 10, and 25 MHz. To reduce interference from ground-based transmitters, frequencies offset above and below 10 and 25 MHz were alternately sampled.

Kotaki et al. [1981] published samples of the data from ISS-b. The lightning counts were accumulated in geographic bins of 10 deg latitude by 10 deg longitude in six time blocks of 4-h each. Those parameters were selected to correspond to the standard defined by CCIR 322 [1963]. Obtaining data for all time periods in the equatorial regions required two months because of the satellite orbit and duty cycles for the onboard equipment. Four months were required for high-latitude regions. Seasonal lightning occurrence maps for each 4-h time block were derived.

The raw count data for each bin were normalized to a constant observation time for all sectors. Values for adjacent bins were averaged to make the occurrence rate smooth locally. The data were then converted to lightning occurrence rate per unit time and area as shown in Table 1.

Lightning occurrence rate isopleths for each of the six 4-h time blocks during all four seasons were constructed. Contour maps for the time block 2200 to 0200 for each season are shown in Figs. 7a-d. As in the WGL TD maps, seasonal variations in lightning location are revealed in these maps. The ISS-b information is inherently more accurate, however, because the number of lightning flashes was measured directly, whereas WGL used an imprecise algorithm to convert TDs to total number of lightning flashes. An equally significant improvement is the replacement of the WGL table of diurnal distribution factors by actual flash data.

The ISS-b data represent by far the most accurate study of global lightning occurrence published to date. Radio-frequency sensors are not obscured by light contamination or cloud cover, so the ISS-b detected a much higher percentage of total lightning activity than the DMSP. We must, however, correlate the data to ground-based measurements before it can be used in the GLO maps.

The results of the OSO and DMSP satellite studies will broaden the data base of the GLO maps provided by ISS-b. The new maps will be

Table 1. Measured rate of lightning discharges for September, October, and November for 2200 to 0200.

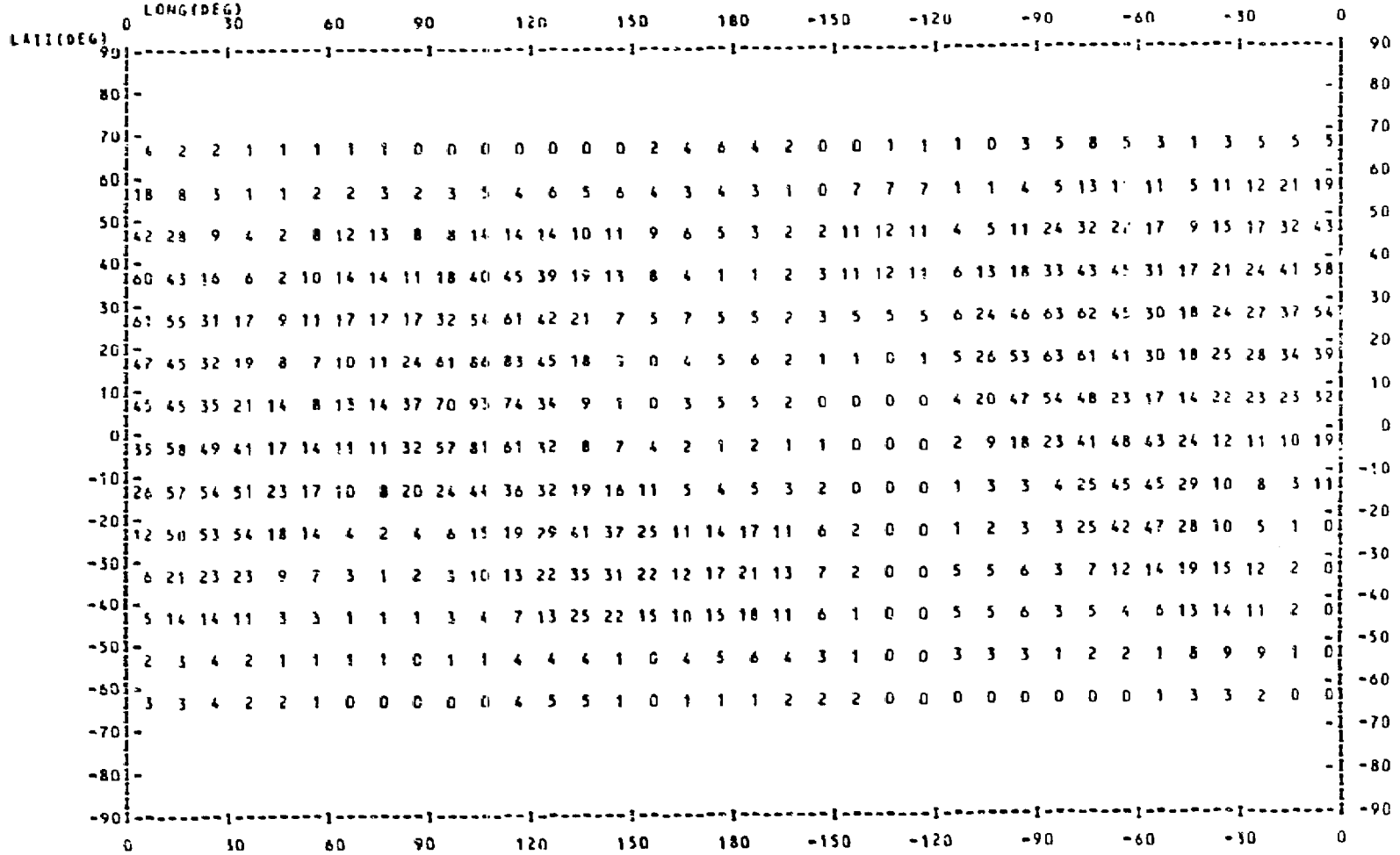

NOTE: Frequency of lightning discharges occurring within 100 km^2/s is obtained by multiplying the numerical value by 10^{-6}.

a. September-October-November.

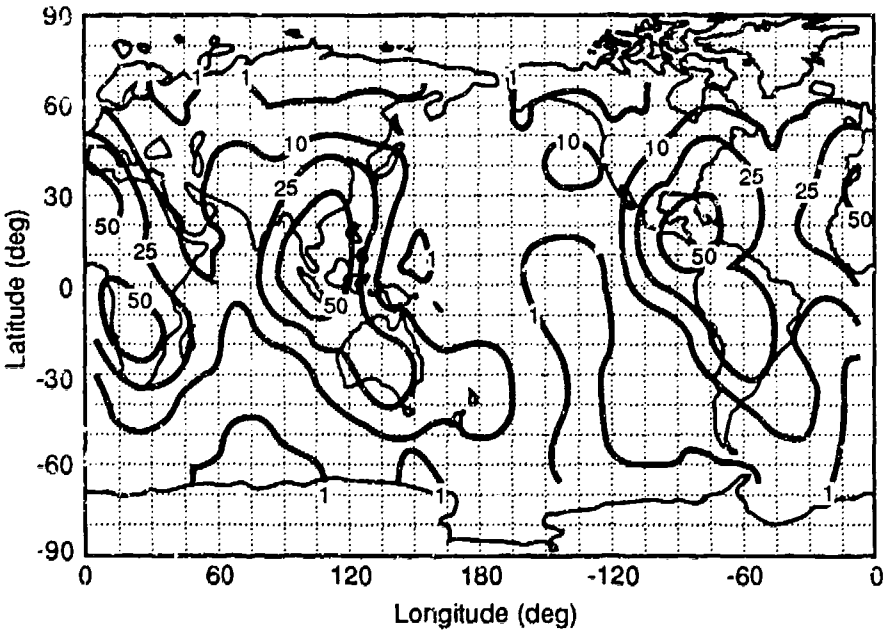

b. December-January-February.

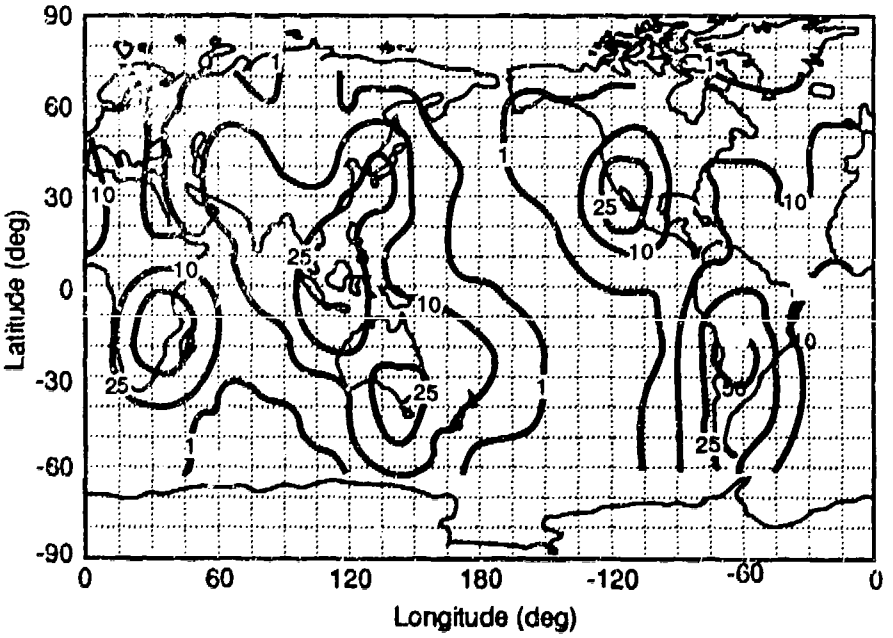

Note: Frequency of lightning discharges occurring within 100 km^2/s is obtained by multiplying contour value by 10^{-6}.

Figure 7. Global distribution of occurrence rate of lightning discharges (2200 to 0200).

c. March-April-May.

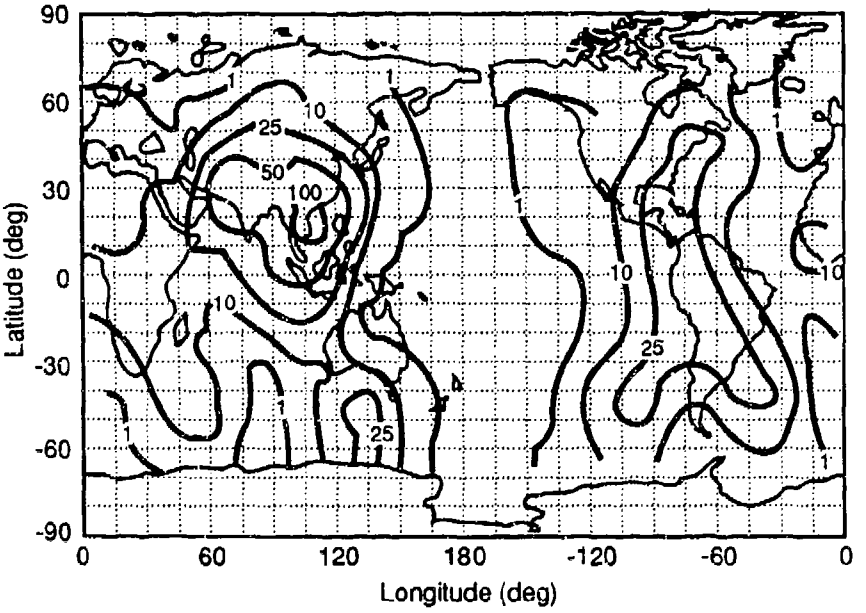

d. June-July-August.

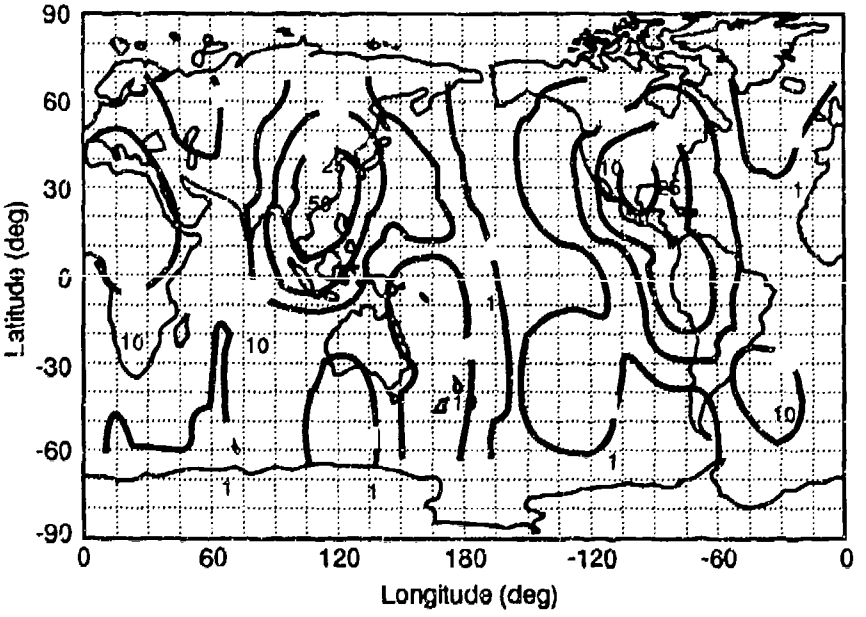

Note: Frequency of lightning discharges occurring within 100 km^2/s is obtained by multiplying contour value by 10^{-6}.

Figure 7. Global distribution of occurrence rate of lightning discharges (200 to 0200) (Concluded).

compared to CCIR 322 and to the WGL maps to incorporate long-term variations in the occurrence rate of thunderstorms. Lightning counter data originally gathered by the WGL also could be used to supplement the GLO map data base. (That information, which WGL converted into TD form for their model, may be available.) Further studies should be incorporated to expand the time duration of the new data base so that variations in lightning quantity and distribution from year to year can be included. Such variations can be significant, as demonstrated by the annual data from ISS-b taken during the northern fall season. Lightning counts for 1978 were approximately double the values recorded for 1979.

Ongoing Measurement Programs. Several organizations have begun installing large networks of lightning counters across the United States to record the time and location of earth flashes. The most extensive of these networks is operated by the State University of New York at Albany. It covers most of the Continental United States, and new stations continue to be added. Although no data from this network has been published, portions of the system have been in operation for more than a year, and some results may be obtainable. We will structure the computer program which generates the GLO contour maps to incorporate new lightning data as it becomes available. This feature will allow periodic revision of the new source maps by enlarging the data base. Ultimately, long-term variations in the storm occurrence rate can be analyzed and incorporated.

SOURCE MODIFIERS.

Noise source maps describe the total number of lightning discharges in a geographic sector over some specified time period. As noted previously in this section, different types of lightning flashes emit different frequency spectra. Source modifiers must be used to determine the proportion of the total number of discharges which are either I-C or C-G. Although of lesser significance, sub-types (such as intercloud and cloud-to-air I-C discharges, or C-G flashes with positively charged leaders) could also be important. If so, separate model flashes will be developed and additional "submodifiers" will be

used tc discriminate between the percentage of I-C or C-G flashes of each subtype.

Several factors have been identified which affect the percentage of I-C and C-G lightning flashes. The first, and best documented, is latitude. Other factors include storm severity, whether the storm occurs over land or ocean, and terrain elevation.

Below, we discuss each factor and describe the ways in which WGL accounted for them, then we detail the approach to source modifiers developed for the new model. Finally, we review a modern algorithm which describes the variation in the proportion of I-C to C-G lightning with latitude.

WGL Source Modifiers.

The WGL used several types of modifiers, necessitated in part by the lack of appropriate data available when that model was developed.

Latitude. The variation in the ratio of I-C to C-G lightning is thought to be related to the height of the 0 deg temperature isotherm. Studies of cloud electrification indicate that maximum charge separation occurs near this level. The altitude of charge separation affects the likelihood that a discharge will contact the ground. Clouds with higher altitude charge separations produce fewer C-G flashes. The old model incorporates the following equation, which Pierce [1968] based upon the scarce data available at that time:

$$\left(\frac{N_c}{N_g}\right)_p = \frac{10}{1 + \frac{\lambda}{30}} - 1 \quad , \tag{2}$$

where N_c and N_g are the densities, in flashes per unit area and time for I-C and C-G flashes respectively, and λ is latitude in degrees.

Storm Severity. As with latitude, the basis for an inverse relationship between storm severity (represented by WGL in the number of TDs per month) and the percentage of C-G flashes was the decrease in the probability of C-G strokes as the altitude of the charge separation layer increases. The strong updrafts associated with

severe storms draw low-altitude, warm air higher in the cloud, increasing the altitude of the charge separation layer. The WGL combined the effects of latitude and storm severity on the I-C/C-G ratio as follows:

$$\frac{N_g}{N_c + N_g} = 0.05 + \frac{0.05 + \sin \lambda}{\left(N_{TD} + 3\right)^{1/2}} , \qquad (3)$$

while acknowledging that there was little empirical support for this modifier equation. Furthermore, after Eq. (3) was used to calculate the distribution and percentages of I-C and C-G lightning flashes from TD maps, an ad hoc correction factor was applied to increase the number of return strokes per C-G flash. That increase was needed to make the predictions of the WGL model agree with measurements of energy radiated by severe storms.

Occurrence over Land/Ocean Masses. The WGL reported that strikes to ground are virtually nonexistent over the oceans. They accounted for this observation by simply decreasing the WGL model noise predictions by 4 dB over the ocean and 2 dB for coastal regions.

Terrain Elevation. Although data indicate that C-G lightning is more prevalent in mountainous regions than other areas, the effects of terrain elevation were not included in the WGL noise model. We will provide a modifier to account for this effect.

Source Modifiers for the New Model.

The WGL model included only vertically polarized (TM) noise. Because the emissions from C-G return strokes dominate TM noise, ad hoc adjustments, such as those just described, could be used by WGL to produce agreement with experimental data. However, we must also include TE noise, the major contributor to which appears to be I-C lightning because of the long horizontal extent of its channels.*

The total number of lightning strokes ($N_c + N_g$) is obtained from the GLO maps. Therefore, an overestimate of N_c will produce a cor-

*A two-dimensional reconstruction of a typical I-C flash, shown in Fig. 8, demonstrates that horizontal structure.

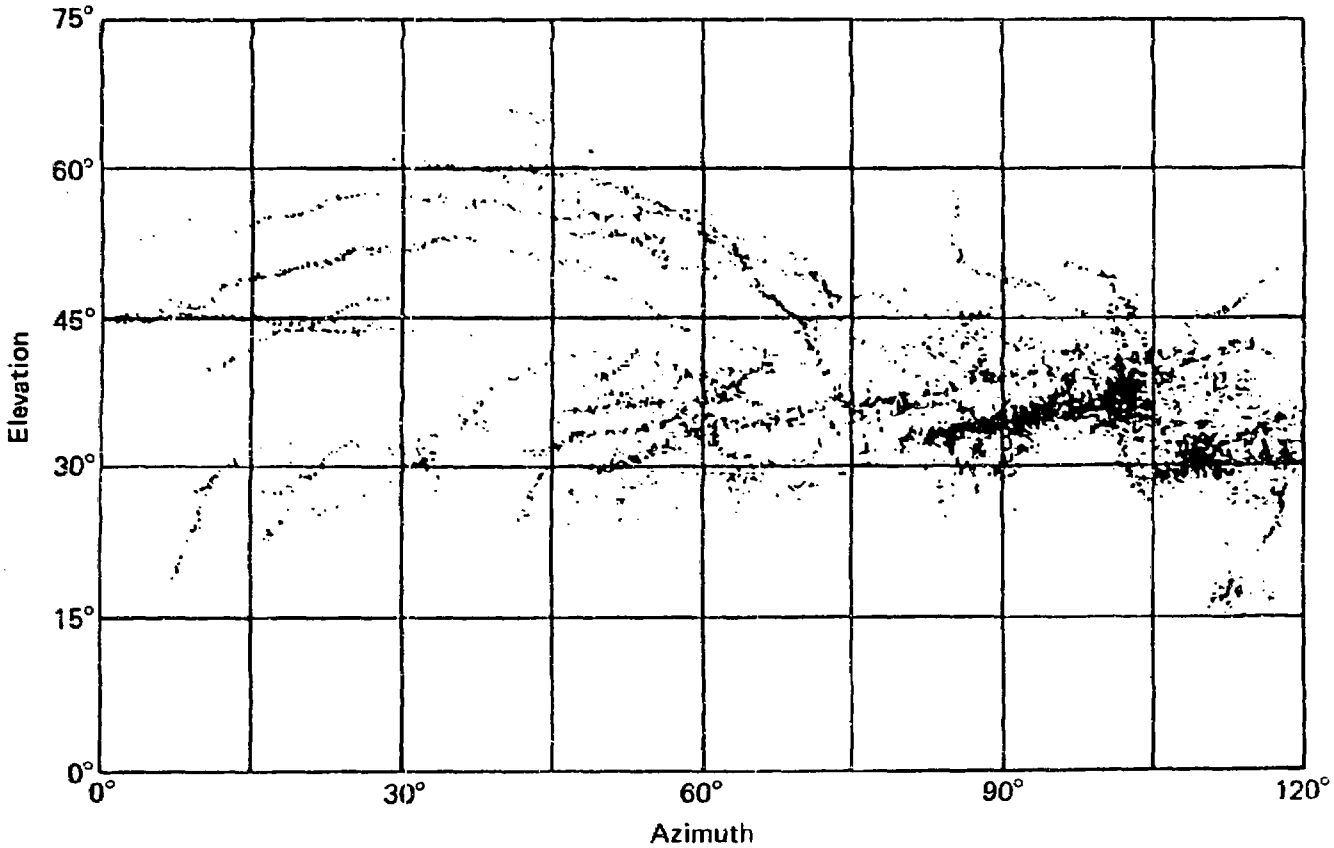

Source: Richard et al. [1987].

Figure 8. Two-dimensional reconstruction of intracloud flash using interferometric lightning location system.

responding underestimate of N_g, and vice versa. Because of the interdependence of N_c and N_g, adjustments such as those used by WGL cannot be used. The new model must accurately portray the percentages of each lightning type. Since N_c dominates TE and N_g dominates TM, N_c/N_g directly affects the ratio of TE to TM noise predicted by the model. The predicted TE/TM ratio will be compared to recent noise measurements conducted aboard balloon platforms [Turtle et al., in press].

The new model will use a composite source definition equation, which is the product of individual source modifiers:

$$\frac{N_c}{N_g} = M_L \cdot M_S \cdot M_E \cdot M_G \ , \tag{4}$$

where M_L is the latitude factor, M_S is the storm severity factor, M_E is the terrain elevation factor, and M_G is the factor which accounts for the land/ocean mass ratio. We conducted a survey of the published literature to develop correlations between N_c/N_g and each of the above factors. Below we discuss the equation for the new model's latitude factor.

Latitude. Prentice and Mackerras [1977] derived a relationship between the percentages of I-C lightning discharges and earth flashes from 29 studies that included over 60,000 flashes. The data points are shown in Fig. 9. The discrimination techniques used by each experimenter included one or more of the following: visual observation, electric field mill, and lightning flash counter. The large scatter in the data is due partly to the biases of different measurement techniques, but may also indicate genuine differences in the I-C to C-G ratio for different localities at the same latitude (such as land/ocean mass differences). Nevertheless, they assumed that such errors are random and that no systematic bias is exhibited by the data.

The data points indicate that $d\zeta/d\lambda$ is small* for λ = 50 to 60 deg. Moreover, Prentice and Mackerras point out that there is no

*Here we use $\zeta = N_c/N_g$.

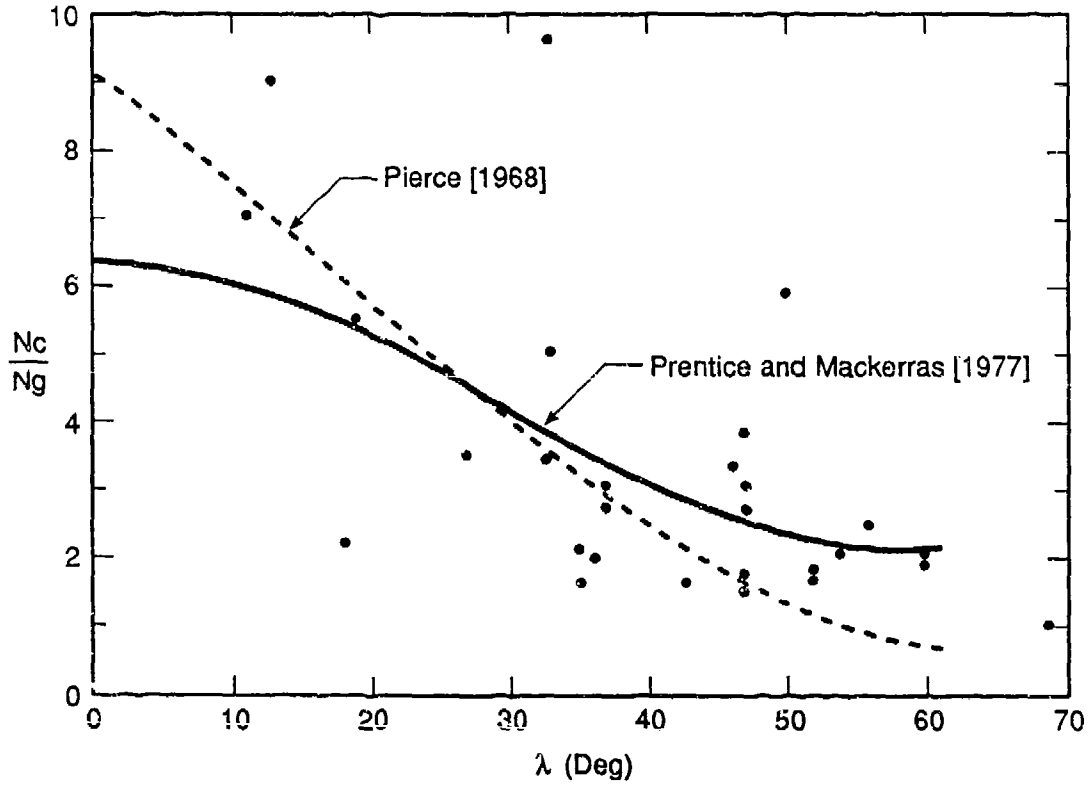

Note: Source of data points—Prentice and Mackerras [1977].

Figure 9. Ratio of densities in flashes per unit area and time of I-C to C-G lightning versus latitude.

evidence for a rapid increase in N_c/N_g as λ approaches zero; and it is unlikely that there are rapid changes in the structure and dynamics of thunderclouds in the equatorial regions. That assertion is supported by Harris and Salman [1972] who confirm that tropical thunderstorm discharges have characteristics similar to those measured in more temperate regions.

In view of the above considerations, Prentice and Mackerras suggest that the relationship between N_c/N_g and λ must satisfy the following boundary conditions: $d\zeta/d\lambda = 0$ at $\lambda = 0$ deg and $\lambda =$ 60 deg. They selected the function $\zeta(\lambda) = A + B \cos 3\lambda$ and, by least-squares fitting, found A = 4.1609 and B = 2.1605. Although better two-parameter fits were found, they did not satisfy the boundary conditions. Therefore Prentice and Mackerras proposed the empirical relationship

$$\zeta(\lambda) = 4.16 + 2.16 \cos 3\lambda \quad 0 < \lambda < 60 \text{ deg} \quad . \tag{5}$$

Equation (5) is shown as the solid line in Fig. 9. The dashed line is from Eq. (2), used in the WGL model.

The difference between the old and new relationships is greatest at low and high latitudes. We will use Eq. (5) for $0 < \lambda < 60$. The WGL omitted sources for $\lambda > 60$. We make the qualitative assumption that the structure of thunderstorms at $\lambda > 60$ does not vary significantly from those at $\lambda = 60$. For $\lambda > 60$ we will use $\zeta(60)$.

Storm Severity, Land/Ocean Mass, Terrain Elevation. Comprehensive studies, such as those described above, have not been conducted to quantify the effects of storm severity, land versus ocean mass, and terrain elevation on N_c/N_g. Lightning experts, however, generally acknowledge a relationship between each of these factors and the proportion of cloud-to-earth flashes. Therefore, we will develop separate algorithms that, although not scientifically rigorous, reflect the influence of each factor based on the minimal data now available and modern theoretical understanding of these phenomena. We include a separate modifier for each factor to allow easy incorporation of results from future studies that better quantify these effects.

SECTION 3
PROPAGATION MODEL

This section begins by giving an overview of PSR's noise propagation submodel and comparing it to the old WGL model. It then gives examples that test the accuracy of the model against full-wave calculations. Virtually all mathematical derivations are relegated to the appendix.

OVERVIEW: NEW MODEL VERSUS WGL MODEL.

Our method, introduced in a previous report [Warber and Field, 1987], efficiently calculates mode coupling caused by changes in ground conductivity under ambient day propagation conditions. We refer to that method, and to the extension developed in the present report, as the approximate model; and to the technique used by WGL as the WGL model. Because atmospheric noise can seldom be specified to within a few decibels, even with extensive data, we--somewhat arbitrarily--set a 3-dB tolerance on the accuracy of the propagation model.

We can generalize our equation for the transverse component of the electromagnetic field as:

$$F_n = \frac{\kappa \sqrt{P}}{\sqrt{a_e \sin (x/a_e)}} \Gamma_t \Gamma_r(x) \; [1 + Q_n(x)] \sqrt{\frac{S_n(0)}{S_n(x)}} \; f_t(z) f_r(x,z)$$

$$\exp \left[-\int_0^x \Omega_n(\chi) \, d\chi \right] , \qquad (6)$$

where F_n is a transverse field component (either E_y or H_y) of the nth earth-ionosphere waveguide mode, P is the radiated power, and $(a_e \sin (x/a_e))^{1/2}$ is the geometric spreading term, where a_e is the radius of the earth and x the distance from the transmitter. The form of Eq. (6) was chosen to allow us to compare our formulation with that

of the WGL. Terms which normally appear in the field equation but which are not important for this comparison have been collected into κ. We may then regard κ as the factor which converts the units of the rest of the right-hand side of Eq. (6) into the units of the field on the right. The exact form of κ depends on the kind of field on the right. The excitation values for the transmitter and receiver, Γ_t and $\Gamma_r(x)$, respectively, also depend on the type of field. Note that Γ_r is a function of distance x. The mode coupling factor is Q_n, which expresses the scattering of energy into or out of the *n*th mode. The terms $f_t(z)$ and $f_r(x,z)$ are the height gain functions for the transmitter and receiver, respectively; they are functions of altitude z and the receiver term is also a function of distance. S_n can be thought of as the sine of the complex angle of incidence of the mode on the ionosphere. Note that this is a function of distance. The attenuation term $\exp[-\int \Omega_n (\chi)\, d\chi]$ contains an integral to express the fact that the attenuation rate is a function of distance. The only difference between Eq. (6) and Eq. (57) in the appendix is that in the latter equation, the terms that specify the transmitter and the spreading term are collected into a single constant called Γ_n. The expanded formulation facilitates discussion of how the WGL model and the approximate model treat each term.

WGL Model.

To calculate VLF noise, WGL determined the number of vertical lightning strokes within a 15 by 15 deg region and combined those strokes into a single equivalent noise transmitter at the center of the region. The 240 equivalent transmitters found in this way form the data base (the polar regions are not included). For each transmitter, the propagation model is used to calculate the signal at the center of the other 239 regions. The RMS sum of the modal fields from all transmitters is then the noise in the center of each region. Using the RMS sum is equivalent to assuming that earth-ionosphere waveguide modes do not interfere. That assumption is valid because atmospheric noise is treated as a statistical quantity and is therefore an average of the contributions from numerous sources at

different locations. That averaging process will smear out nulls caused by mode interference. The noise at intermediate locations is determined by interpolation.

In order to perform this large number of calculations quickly on the computers available in 1970, the WGL model retained only three modes, whose attenuation and excitation values were precalculated for two ambient ionospheres (day and night) and several ground conductivities. The model takes the height gain factors $f_t(z)$ and $f_r(x,z)$ to be unity, since it deals solely with TM modes, whose height gains are approximately unity up to aircraft altitudes. The WGL model also assumes that the mode coupling term $Q_n(x)$ is zero. Westinghouse Georesearch partially justifies that assumption by pointing out that Q_n is small for frequencies below 16 kHz (they considered only frequencies between 10 and 30 kHz). They also argued that mode coupling merely rearranges the energy between modes, at least during the sunrise and sunset periods, and thus tends to cancel out in the summation. That argument is incorrect, however, if energy is coupled to modes other than the lowest three, which were the only ones retained.

The WGL model includes ad hoc corrections to account for the dependence of attenuation rate on direction of propagation and solar zenith angle. Those formulas contain constants assumed to be independent of the mode number, although even WGL points out that those constants, in fact, are mode dependent.

New Propagation Submodel.

The noise model that we are developing will also use the concept of equivalent noise transmitters, although, as discussed in Sec. 2, our data base will include the effects of both vertical and horizontal transmitters. The new propagation submodel must therefore include both TE and TM modes and allow for conversion between them (i.e., at night). The new model also must predict noise under disturbed ionospheric conditions as well as ambient conditions. The need to extend the frequency range of the predictions up to 60 kHz will require more

careful treatment of the mode coupling and mode conversion*, because those phenomena are stronger at LF than at VLF.

In full-wave computer codes, the ionosphere is modeled by specifying the number-density profiles of free electrons and any ion species present. These full-wave methods, although accurate, would be much too slow for the many-source model of interest here; a faster method is needed. Our approximate propagation model combines precalculated full-wave results with a model waveguide that treats portions of the ionosphere as a sharply bounded conducting space. That approximation, which is the major one, allows formulation of analytic equations for mode coupling under nonstratified conditions. The height and conductivity of the sharply-bounded ionosphere are chosen to give propagation parameters that agree with the full-wave results.

Warber and Field [1987] assumed the conductivity and height of the ionosphere to be constant, but allowed the ground conductivity to change within a region of length Δx. In the appendix of the present report we extend that method to situations in which the height of the ionosphere undergoes lateral changes, but the conductivities are constant. Such ionospheric height changes occur, for example, at boundaries between ambient and nuclear-disturbed regions. In addition, the appendix derives a method to easily calculate the change in attenuation rate as the propagation direction changes with respect to the earth's magnetic field at night.

The mode coupling function of Eq. (6) is the double summation of a series of scattering terms:

$$Q_n(x) = \sum_k \left[Q_{nn}^{(k+1)} + \sum_{\substack{m \\ m \neq n}} Q_{nm}^{(k)} \right] . \qquad (7)$$

Here $Q_{nm}^{(k)}$ represents the kth order scattering of energy from the nth to the mth mode, and the $Q_{nn}^{(k+1)}$ represents the energy scattered back

*We define mode coupling as the transfer of energy between modes due to lateral transitions in propagation conditions, whereas mode conversion results from the earth's magnetic field changing part of a TM field into a TE field and vice versa.

into the mode from all the other modes. Warber and Field [1987] discuss the scattering matrix in detail. The computer algorithm that determines $Q_{nm}^{(k)}$ keeps track of the size of each scattering order and truncates the sum when the scattering becomes small. In addition, the number of retained modes is monitored and increased, if necessary, during a coupling calculation. Examples of mode coupling at transitions between nuclear-disturbed and ambient ionospheres are given later in this section.

It is well-known that modeling of propagation under ambient night conditions is difficult, especially for west-to-east propagation. Even full-wave computer codes are hard-pressed to give accurate results [Pappert and Hitney, 1988]. It is therefore not surprising that we were unable to develop a satisfactory fast-running approximate method for undisturbed nighttime propagation. However, we have developed a fast method to calculate the change in attenuation rate as the propagation direction changes. That method uses full-wave results at a particular propagation direction (e.g., east to west) to determine an anisotropic conducting layer to represent the ionosphere. Then we can use the fast approximate model to find the propagation parameters for other directions, thus avoiding full-fledged calculations for each of many propagation directions. Again, details are given in the appendix and later in this section.

To summarize, our propagation submodel was developed to take advantage of the increase in computing power that has occurred in the 18 years since the publication of the WGL model. It is still necessary to perform the calculations efficiently, however, because of the enormous number of modes and paths. Tests against the full-wave code show our method decreases computer running time up to fivefold, depending on the particular situation.

PROPAGATION UNDER NUCLEAR-DISTURBED CONDITIONS.

We will model nuclear-disturbed ionospheres using standard spread-debris environments based on radiation from fission debris shining down on the VLF reflecting regions. The debris is assumed to be spread over a wide area at altitudes around 150 km. The resulting disturbed ionospheres are characterized by the parameter W, which is a

measure of the ionizing intensity of the debris, and is defined as

$$W = \frac{Y_F}{A(1 + t)^{1.2}} , \tag{8}$$

where Y_F = total deposited fission yield in megatons,

A = area over which debris is uniformly spread in square kilometers,

t = time after the burst in seconds.

Strictly speaking, the above definition applies only to situations in which all bursts occur at $t = 0$. For a large number of bursts at different times, we could express W as a sum of $Y_F/(1 + t)^{1.2}$ terms over a constant area, and determine an equivalent value for any time. The noise model must apply to a range of environments rather than a specific scenario; the parameter W is a simple yet realistic way to characterize the ionospheres.

A value for W of $\sim 10^{-8}$ represents a severe environment; values between 10^{-10} and 10^{-11} characterize moderate environments; and smaller values, weakly disturbed environments.

Figure 10 shows the ion and electron density profiles calculated by Field and Dore [1975] for a range of W values. Those profiles have been used in our full-wave code to determine the propagation parameters over a range of ground conductivities and frequencies (see

Table 2. Effective ionospheric heights for approximate model.

W (MT/km^2-s$^{1.2}$)	h (km)
2×10^{-8}	31
2×10^{-9}	35
2×10^{-10}	42
2×10^{-11}	49
2×10^{-12}	50
2×10^{-13}	56
2×10^{-14}	58
2×10^{-15}	60

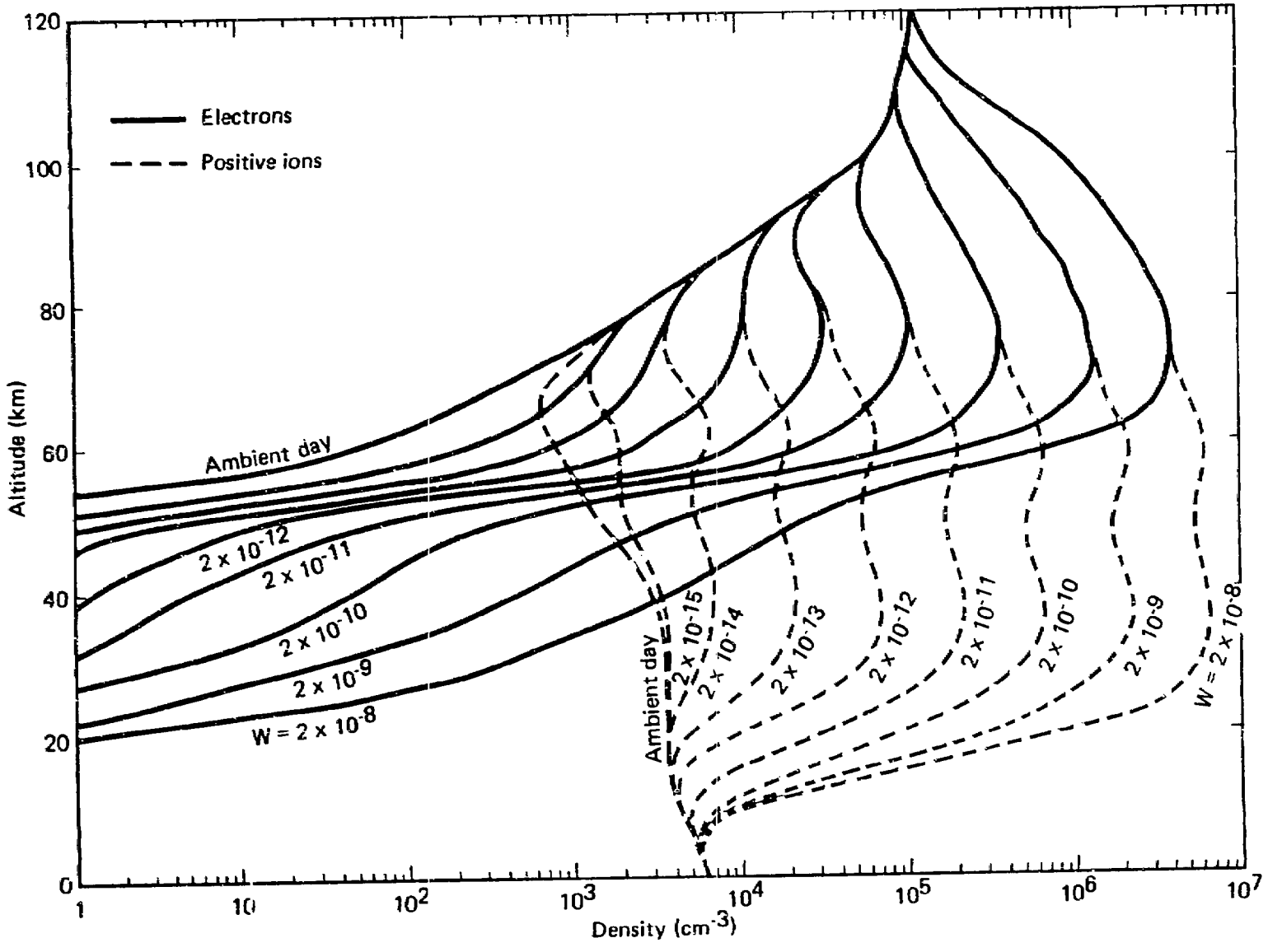

Figure 10. Electron and ion density profile for ambient and spread debris environments.

Vol. II). By using these propagation parameter data we can select a set of effective heights (h) and ionosphere conductivities (σ_i) that cause our approximate model to give results that agree with full-wave results. For the examples that follow, we found that at 30kHz we could take $\sigma_i \sim 3 \times 10^{-7}$ S/m for each W value and then find a effective height that fit the full-wave data well. These are given in Table 2. Note that the effective height is just a parameter in our model and does not correspond to a physical reflection height. Moreover such use of mathematically convenient effective heights is common. For example, when exponential ionospheric models (e.g. β = 0.3, h' = 72 km) are used in the literature, the effective height h' merely establishes a reference level, and bears no relation to the physical reflection heights. Such reference levels are not unique and can vary from model to model provided that certain other mathematical parameters are adjusted to accommodate changes in h'. For our model other values of h would work, provided we changed σ_i accordingly.

In order to model the transition from ambient to disturbed conditions, we must specify the distance over which this transition takes place. This transition distance is somewhat scenario dependent. For example, a high-altitude detonation throws debris high into the ionosphere, so at early times the debris has a large line of sight, and the ionosphere is affected over distances of several megameters. At later times, as the debris lowers and spreads out, the total affected area is still large, but the width of transition zone shrinks, because radiation from the edge of the debris shines over shorter distances. Roughly speaking, the ionosphere is affected laterally out to distances on the order of 3 times the debris height, often assumed to be on the order of 150 km for spread-fission debris. This height would therefore correspond to a transition zone width on the order of half a megameter. More severe environments will affect the ionosphere out to greater distances than weaker ones.

We now compare the full-wave and approximate calculations. For the full-wave calculations, we assumed a transition width of 600 km, and divided the transition from the $W = 2 \times 10^{-8}$ disturbed ionosphere to the ambient ionosphere (which has a W of approximately 2×10^{-15}) into six zones, each 100-km wide. Later in this section we

demonstrate the effects of zone width on mode coupling. For the approximate calculation we assume the height of the ionosphere varies smoothly from the ambient, h_0, to the disturbed ionosphere, h_D; i.e., we assume that the derivative of the function $h(x)$ is continuous. We define the coordinate system such that the transition region starts at $x = 0$ and ends at $x = \Delta x$. In the examples in this section, we used the following functional form for $h(x)$:

$$h(x) = \begin{cases} h_0 + \Delta h & \text{for } x > \Delta x \ , \\ h_0 + \Delta h \left[3\left(\frac{x}{\Delta x}\right)^2 - 2\left(\frac{x}{\Delta x}\right)^3\right] & \text{for } 0 \le x \le \Delta x \ , \\ h_0 & \text{for } x < 0 \ . \end{cases} \tag{9}$$

This form was chosen so that $h(x)$ and dh/dx are continuous for all values of x. Figure 11 illustrates this dependence.

Figure 12 compares the full-wave calculation with the approximate one for propagation from a disturbed to an ambient environment. The assumed ground conductivity is 10^{-2} S/m. We show the field strength normalized to unity at the start of the transition region (x = 0 km) for the first two TM modes. For the approximate calculation, we assume that only the first mode exists at the beginning of the transition. That assumption is consistent with the full-wave calculation, which showed that the second TM mode was on the order of 60 dB smaller than the first at the start of the transition (1 Mm from the transmitter). The solid line in Fig. 12 shows the full-wave calculation. The jumps are caused by mode coupling at the start of each region. The dashed line is the approximate calculation. At the end of the transition (x = 600 km), the approximate results are only about 1 dB higher than the full-wave results, well within the tolerable error. Similar results are obtained for TE modes.

Figure 13 shows results for a signal propagating from ambient conditions to disturbed regions. Contrary to the prior example, the first and second modes dominate at the start of the transition, with the second, due to its greater excitation, being 6 dB greater than the first. The second mode decreases in magnitude and becomes very small

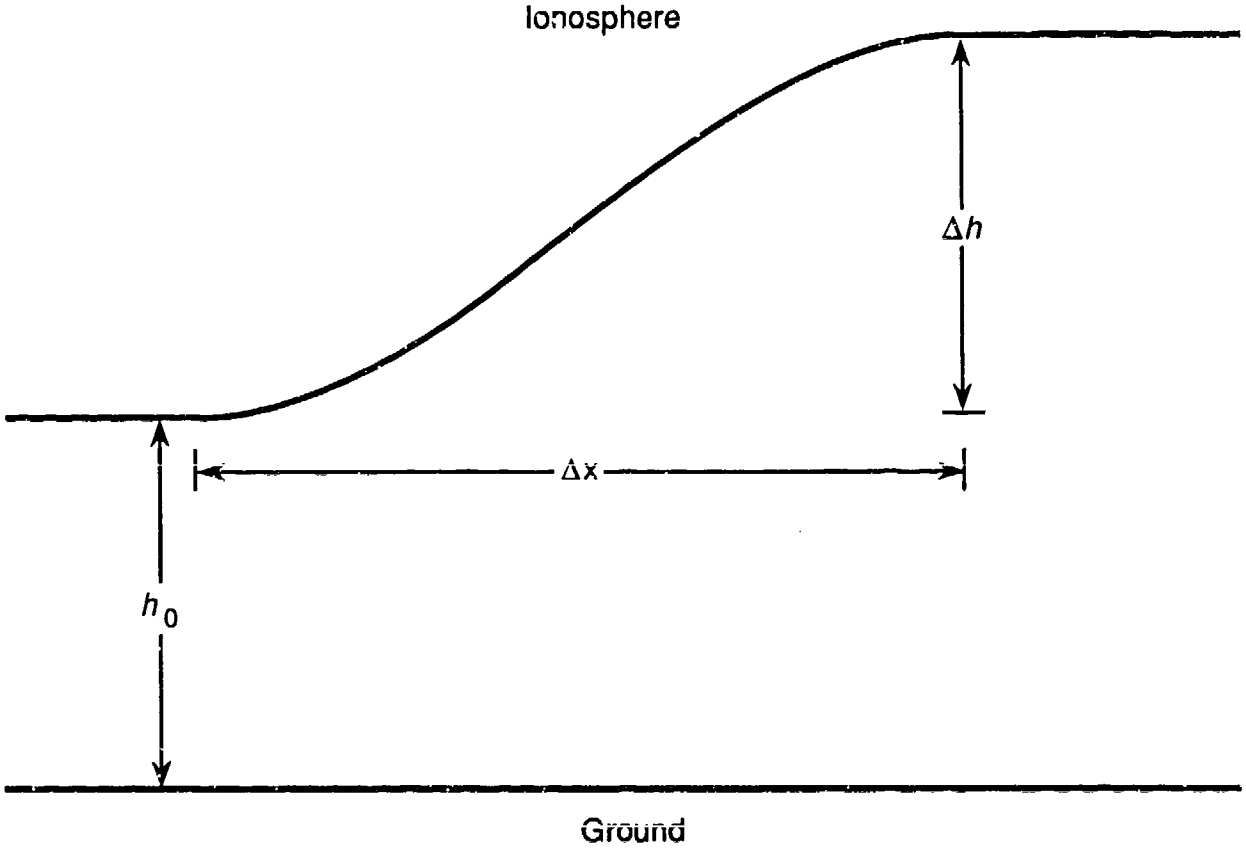

Figure 11. Model of change in ionosphere height from disturbed to ambient day conditions.

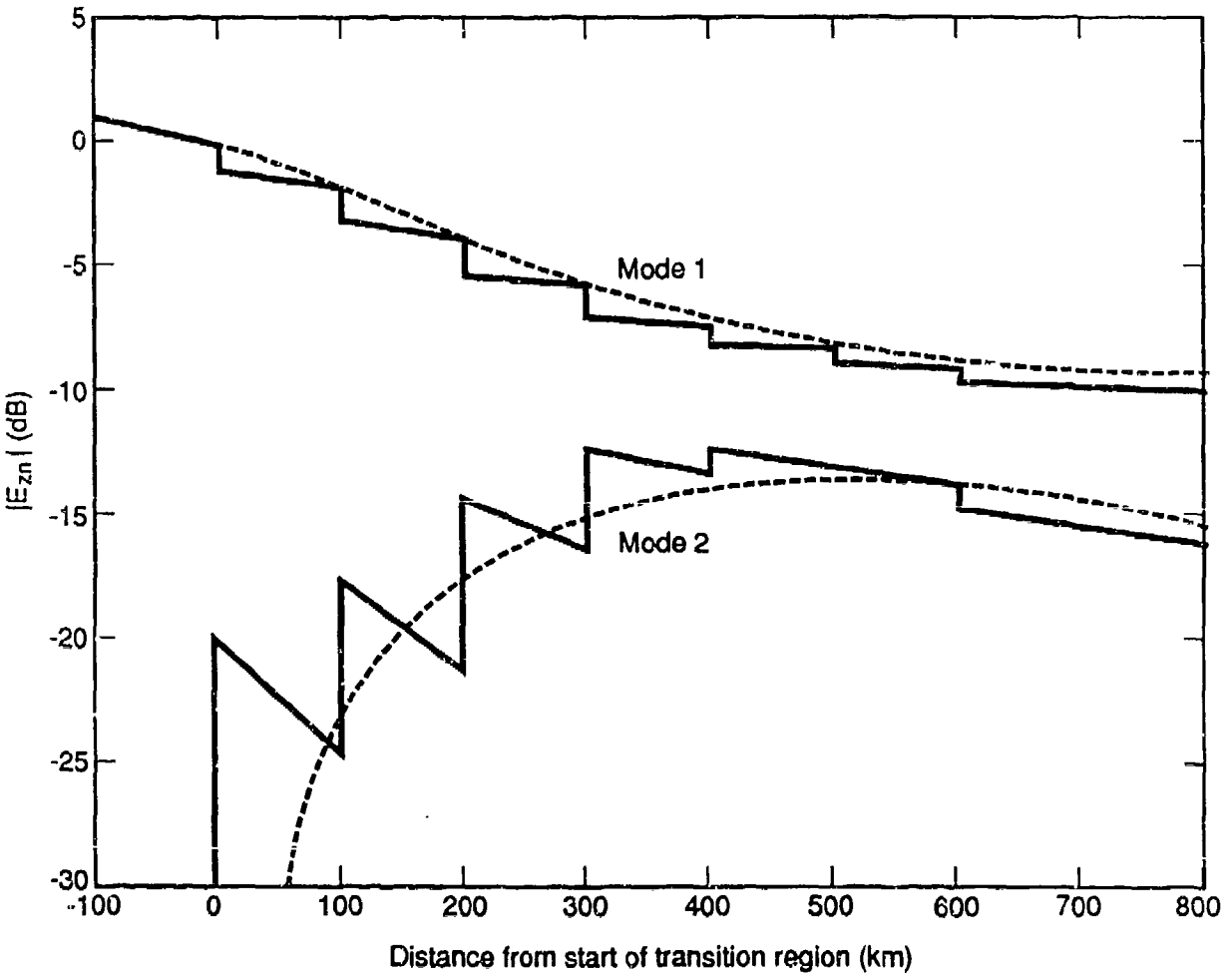

Figure 12. Comparison of full-wave to approximate calculation for TM propagation from disturbed to ambient environment.

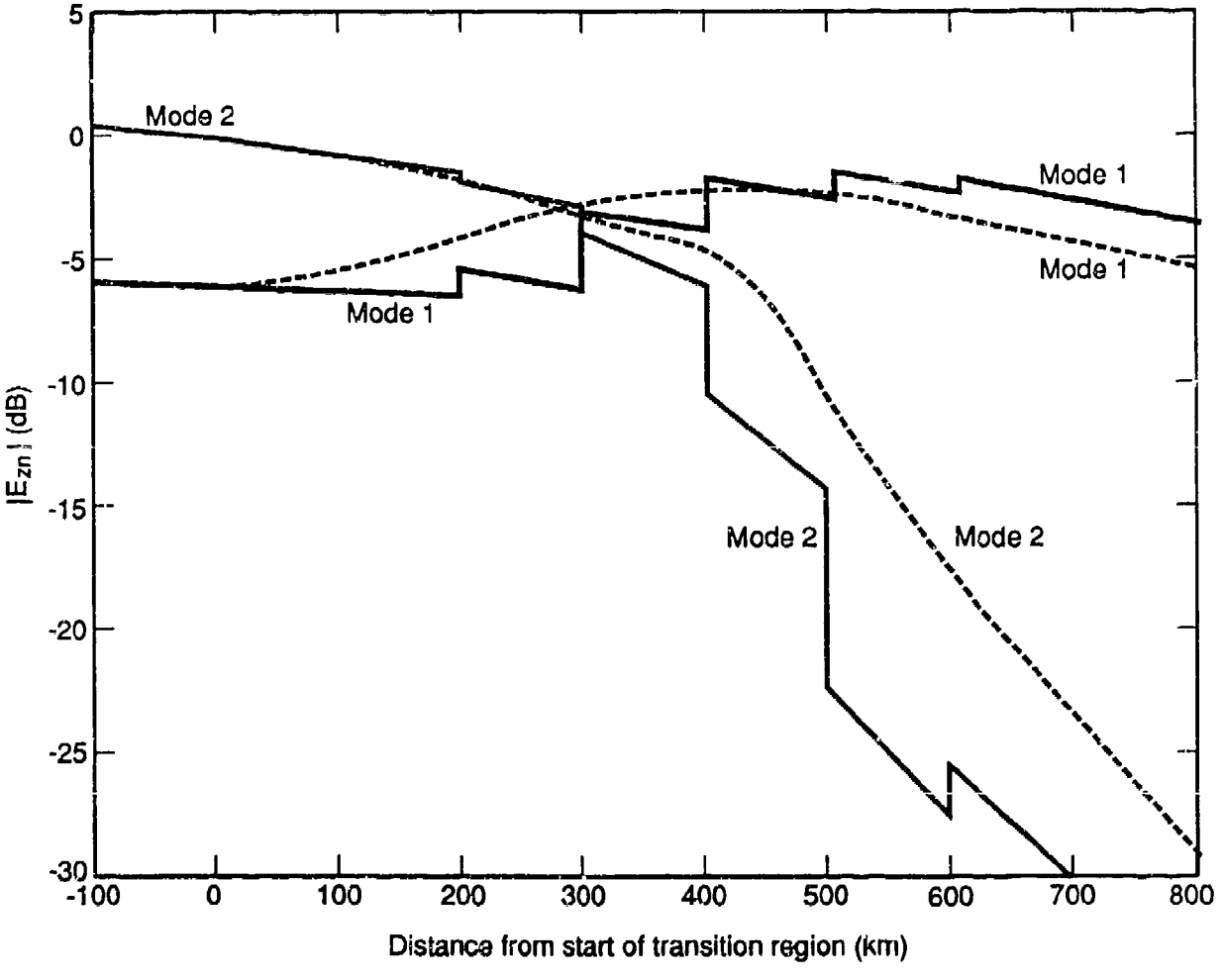

Figure 13. Comparison of full-wave to approximate calculation for propagation from ambient to disturbed environment.

by the end of the transition, whereas the strength of the first mode increases somewhat. This increase in strength is due largely to the increase in excitation values caused by the narrower waveguide. At the end of the transition the approximate model results are 1.5 dB lower than the full-wave results for the first mode; again, this is within the 3-dB tolerance. The agreement is not as close for the second mode, but this mode is so heavily attenuated that the errors are of no importance to the total field.

To determine the effect of the transition-zone width on the approximate calculation, we consider propagation from the disturbed to the ambient regions for widths from 0.1 to 1 Mm. The results are as expected: The shorter transition regions, which have a larger derivative of $h(x)$, require higher scattering orders and so take longer to run. In Fig. 12, for example, we need only scattering order 3, while a 1-Mm transition region needs only order 2, and a 0.1 Mm region needs order 7. The full-wave calculations shown in Figs. 12 and 13 use four modes in regions where W is large and six where W is small.

In the full-wave calculation there is a trade-off in difficulty between the mode-finding calculation and the mode-coupling calculation. If the change in conditions at a boundary occurs abruptly--or is severe--then many modes must be found in order to determine the signal structure correctly; there is a noticeable error in the signal if too few modes are used. If more steps are used to make the change at the step boundaries less abrupt, then more mode-coupling calculations are needed.

The fact that only order 2 is needed when $\Delta x \sim 1$ Mm means that very little mode coupling occurs in this case. The change in the field strength of the dominant mode is due almost entirely to the decrease in the excitation values caused by the increasing height of the ionosphere. Because of that height increase, the energy in the field has to spread out over a greater volume and, in effect, becomes diluted.

PROPAGATION FOR AMBIENT NIGHT.

Ambient-night propagation differs from ambient day or nuclear-disturbed propagation in three major ways:

1. The attenuation rate of the modes is much lower.
2. An individual mode contains both TM and TE fields, i.e., the modes are now "quasi" TM or TE.
3. The propagation parameters are dependent on the angle ϕ that the direction of propagation makes with the earth's magnetic field.

In our model, the first point is less important than the others, because it is valid to assume that the modes do not interfere. In a full-wave calculation with interference, a large number of modes (as many as 20) are needed to account for the signal interference structure. We need only consider six to eight modes.

The approximate model treats the nighttime ionosphere as an anisotropic conducting layer. The modal equation in this case is:

$$({}_{\parallel}R_{\parallel}^{gnd}\ {}_{\parallel}R_{\parallel}^{ion}\ e^{-2ikCh} - 1)\ ({}_{\perp}R_{\perp}^{ion}\ {}_{\perp}R_{\perp}^{gnd}\ e^{-2ikCh} - 1)$$

$$- {}_{\perp}R_{\perp}^{gnd}\ {}_{\parallel}K_{\parallel}^{gnd}\ {}_{\perp}R_{\parallel}^{ion}\ {}_{\parallel}R_{\perp}^{ion}\ e^{-4ikCh} = 0\ . \qquad (10)$$

Equation (10) is fully derived in the appendix.

Here R^{ion} represents the ionosphere reflection coefficients and R^{gnd} the ground reflection coefficients. We use Budden's [1961] classic definitions in which ${}_{\parallel}R_{\parallel}$ expresses the reflection of TM fields into TM fields and ${}_{\perp}R_{\perp}$ represents the reflection of TE fields into TE fields. The ${}_{\perp}R_{\parallel}$ and ${}_{\parallel}R_{\perp}$, which are nonzero only for the ionosphere, represent the reflection of TM fields into TE fields and vice versa. The exp(-2ikCh) terms in Eq. (10) occur because we define the ionospheric reflection coefficient as the ratio of the reflected-to-incident waves defined at the ionospheric boundary ($z = h$), whereas the ground reflection coefficients are defined at $z = 0$. Here k is the wavenumber (2π/wavelength) and C is the cosine of the angle of incidence.

The height gains in the waveguide can be expressed in terms of the reflection coefficients. In Appendix A, we show how this is done.

The dependence on direction of propagation can be dramatic. Figure 14 shows the attenuation rate for several modes and a typical ambient-night ionosphere. We chose the 1st, 4th, 5th, and 7th least attenuated modes* from a data set created at 30 kHz for west-to-east propagation. The assumed ionosphere was exponential, with $\beta = 0.5$ km^{-1} and h′ = 80 km; that model is often used with good results.** The geomagnetic field dip angle is 60 deg.

Figure 14 shows the results obtained using the full-wave code and varying the propagation azimuth angle over 360 deg. The lower order modes are slightly less attenuated for west-to-east propagation (ϕ = 90 deg) than for east-to-west (ϕ = 270 deg), the well-known "east-west" effect. There is no difference between south-to-north (ϕ = 0 deg) and north-to-south (ϕ = 180 deg) propagation, but there is a significant difference between ϕ = 0 deg and $\phi = \pm$ 90 deg propagation. Three of the modes show attenuation minima at ϕ = 0 deg or 180 deg; one shows attenuation maxima at those angles. The three showing minima are quasi-TM at ϕ = 270 deg, the one showing maxima is quasi-TE. (Usually, a mode that is quasi-TE at $\phi = \pm$ 90 deg becomes quasi-TM at ϕ = 0 deg or 180 deg, and vice versa).

The angle ϕ changes along all paths except those lying along the magnetic equator, or directly north-south. Because the attenuation rate depends only weakly on ϕ (except near ϕ = 0 deg, 180 deg, or near the magnetic poles) we need not be too concerned about attenuation changing along a path due to changing ϕ.

In Appendix A we show that in order to specify the sharply-bounded anisotropic ionosphere, we need a parameter $\mathcal{Y}$ in addition to σ_i and h, which were adequate to define the isotropic ionosphere. That additional parameter $\mathcal{Y}$, is given by

---

*Note that the choice of modes was arbitrary and made simply to allow easy plotting on a single figure.

**The parameters h′ and β are the classic ones originally defined by Wait and Spies [1964]; also see Wait [1970].

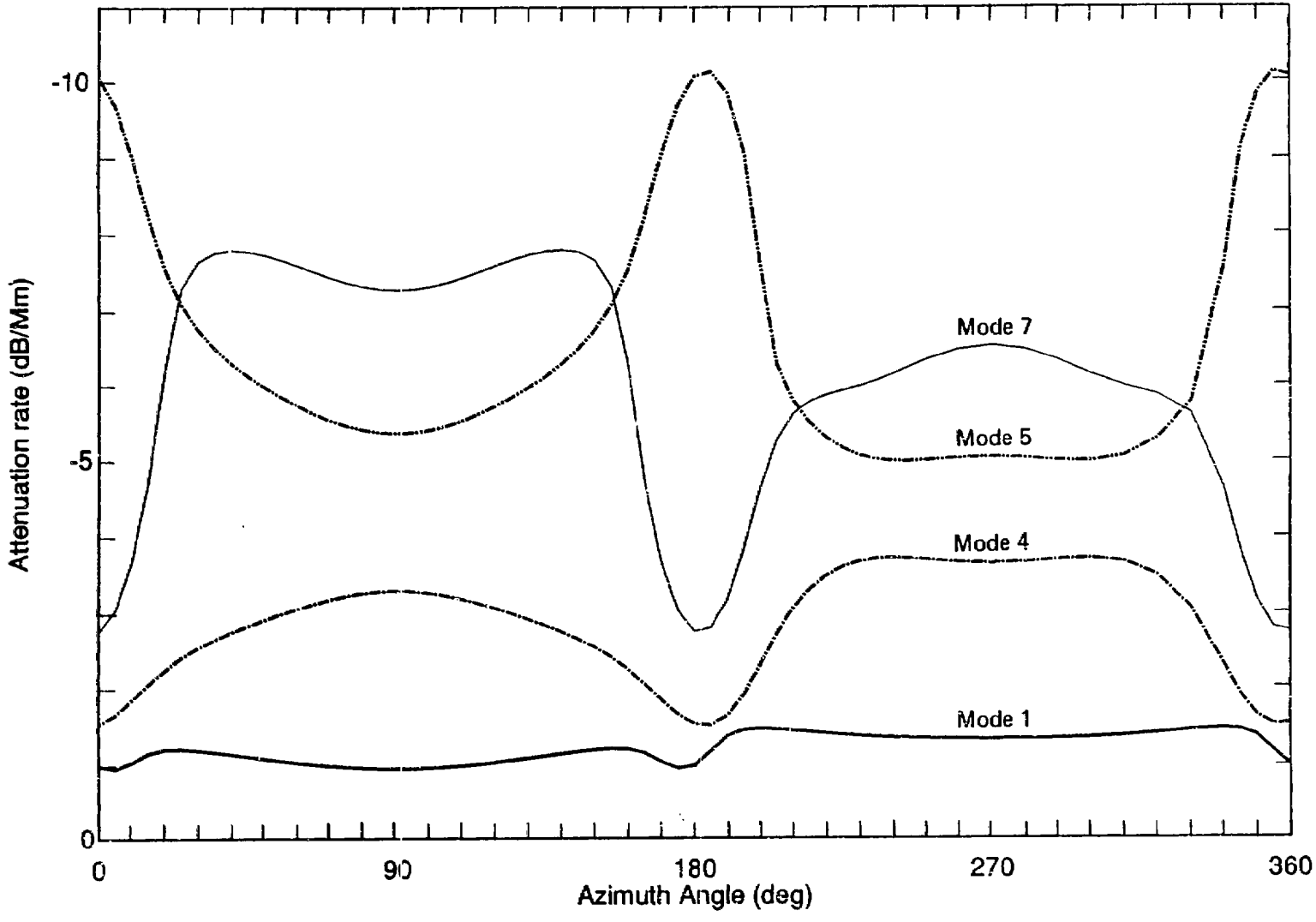

Figure 14. Attenuation rate as function of azimuth angle for four selected modes at night.

$$y = \frac{Y}{U} \approx \frac{\omega_g}{\nu} \quad , \tag{11}$$

where Y and U are the standard magnetic-ionic parameters defined in the appendix, where ω_g is the gyro frequency, and ν is the electron-neutral ion collision frequency.

In our approximate model we use the modal equation (Eq. 10), to determine how the attenuation changes with azimuth. As an example, using the full-wave results for mode 7 in Fig. 14, we find that $h \approx 122$ km,* $\sigma_i \approx 6 \times 10^{-7}$S/m, and $y = 30$, give the best agreement. We can then solve the modal equation as a function of ϕ and compare with full-wave results. Figure 15 shows that comparison. Although the approximate calculation does not reproduce all details of the full-wave results, the agreement is within 1 dB. Figure 15 is important because it gives an alternative to performing a separate full-wave calculation for each propagation direction from every noise source. Instead, we need perform the full-wave nighttime calculation only once for some cardinal direction and then use results like those of Fig. 15 to adjust to other directions.

*This value is much larger than the altitude at which VLF reflections occur in the real ionosphere.

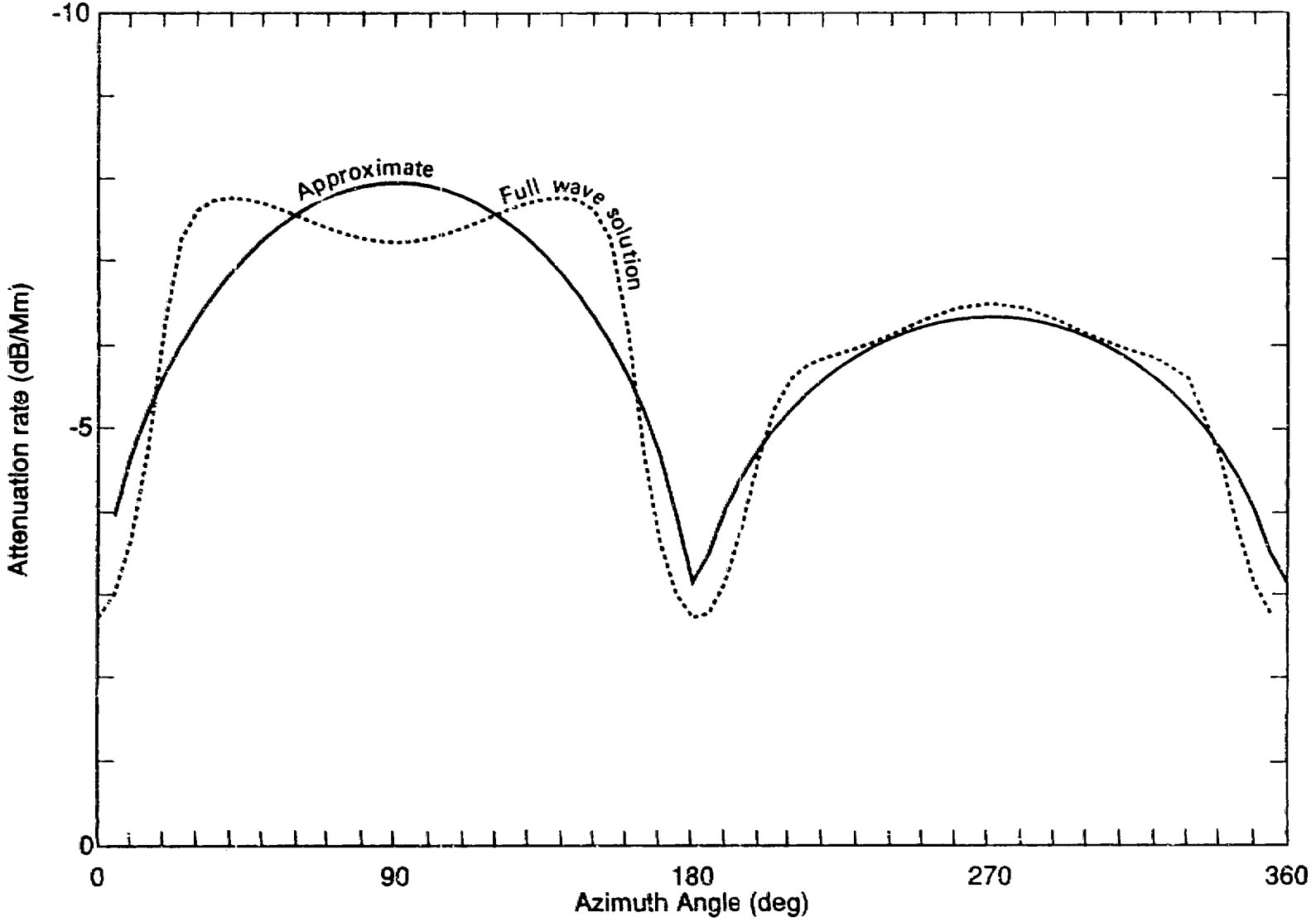

Figure 15. Comparison of full-wave to approximate calculation for selected mode at night.

SECTION 4

LIST OF REFERENCES

Budden, K. G., *Radio Waves in the Ionosphere*, Cambridge University Press, London, 1961.

CCIR (International Radio Consultative Committee), *World Distribution and Characteristics of Atmospheric Radio Noise*, International Telecommunications Union, Geneva, Switzerland, Report 322, 1963.

Fitzgerald, D. R., "Thunderstorm activity," *Handb. Geophys. Space Environ.*, 1985.

Harris, D. J., and Y. E. Salman, "The measurement of lightning characteristics in northern Nigeria," *J. Atmos. Terr. Phys.*, Vol. 34, 1972, pp. 775-786.

Kotaki, M., et al., "Global distribution of thunderstorm activity observed with ISS-b," *J. Radio Res. Lab.*, Vol. 28, No. 125/126, March/July 1981.

Pappert, R. A., and L. R. Hitney, "Empirical modeling of nighttime easterly and westerly VLF propagation in the earth-ionosphere waveguide," *Radio Sci.*, Vol. 23, No. 4, July-August 1988, pp. 599-611.

Pierce, E. T., "The Counting of Lightning Flashes," *SRI Special Report 49*, June 1968.

Prentice, S. A., and D. Mackerras, "The ratio of cloud to cloud-ground lightning flashes in thunderstorms," *J. Appl. Meteorol.*, Vol. 16, May 1977, pp. 545-550.

Ratcliffe, J. A., *The Magneto-Ionic Theory*, Cambridge University Press, London, 1959.

Richard P., et al., *SAFIR: Lightning Monitoring and Warning System*, paper presented at 22d General Assembly of the International Union of Radio Science, Tel Aviv, Israel, 24 August-2 September 1987, subsequently published by the Office National d'Etudes et de Recherches Aerospatiales, Chatillon-sous Bagneux, France, as T. P. No. 1988-4.

Turman, B. N., and B. C. Edgar, "Global lightning distributions at dawn and dusk," *J. Geophys. Res.*, Vol. 87, No. C2, February 1982, pp. 1191-1206.

Turtle, J., et al., "Low-frequency TE atmospheric noise: measurement and theory," *Radio Sci.*, in press.

Uman, M. A., and E. P. Krider, "A review of natural lightning: experimental data and modeling," *IEEE Trans. Electromagn. Compat.*, Vol. EMC-24, No. 2, May 1982.

Vorpahl, J. A., J. G. Sparrow, and E. P. Ney, "Satellite Observations of Lightning," *Science*, Vol. 169, June 1970.

Wait, J. R., *Electromagnetic Waves in Stratified Media*, Pergamon Press, New York City, 1970.

Wait, J. R., and K. P. Spies, *Characteristics of the Earth-Ionosphere Waveguide for VLF Radio Waves*, U.S. Department of Commerce, National Bureau of Standards, Washington, DC, Technical Note 300, 1964.

Warber, C. R., and E. C. Field, Jr., *Mode Coupling in VLF/LF Atmospheric Noise Models*, PSR Report 1725, subsequently published by the Defense Nuclear Agency, Washington, DC, as DNA-TR-87-169, 31 August 1987.

Westinghouse Georesearch Laboratory, *Development of a VLF Atmospheric Noise Model*, Boulder, Colorado, 30 June 1970, subsequently published by the Naval Research Laboratory, Washington, DC, July 1972.

APPENDIX A
DERIVATION OF EQUATIONS

INTRODUCTION.

This appendix shows the derivation of our method for rapidly calculating the coupling of modes across a region of changing propagation conditions. The method generalizes work of Warber and Field [1987], who developed a model to compute daytime mode coupling that occurs at changes in ground conductivity. Here we extend that method to lateral changes in the ionosphere, particularly in the ionosphere height. Moreover, we account for the nighttime propagation anisotropy caused by the geomagnetic field. Some of the results of Warber and Field [1987] are repeated here to make this appendix self-contained, but the reader should be familiar with that earlier report.

This time we begin by deriving the approximate equations for the general case of a lateral change in any propagation condition. Then we restate the results for the daytime change in ground conductivity which was the subject of Warber and Field [1987]. Next, we extend the analysis to lateral changes in the ionosphere height which can occur, for example, at the transition between ambient conditions and disturbed ionospheric conditions. Finally, we consider nighttime propagation.

Nighttime and daytime propagation differ in several important respects. First, of course, are the much lower attenuation rates which require the calculation of a large number of modes in order to define the signal structure. This is of less importance in the noise model than for man-made signals because, as discussed in the main text, modes from lightning strokes do not interfere. Of greater importance is the fact that at night--unlike the daytime case--we cannot assume that the modes are pure TE or TM. We must account for a single mode excitation of both the horizontal magnetic and horizontal electric fields. Finally, our approximate method must reproduce the marked dependence that the propagation parameters have on the angle between the propagation direction and the earth's magnetic field.

In the earlier work we assumed that the fields in the ground could be ignored. This was equivalent to assuming that the Booker quartic q_g in the ground was independent of the propagation parameter C_n. The largest error this assumption made in the value of q_g was about 2 percent at the very low conductivity of sea ice, $\sigma_g \sim 10^{-5}$ S/m. Although errors of such small degree are not critical to the analysis, we do not make the same assumption here. This leads to slightly more complicated forms for the critical functions Λ_n and K_{nm}, however, as defined later in the appendix. When those differences occur they will be noted.

We assume that the normal to the wavefront lies in the xz-plane and makes an angle θ with the vertical. We call the angle the projection of the earth's magnetic field on the ground (xy) plane makes with the x-axis the azimuth of propagation (ϕ). The angle the geomagnetic field makes with the horizontal is called the geomagnetic dip and is denoted by δ. The dip is positive in the Northern Hemisphere and negative in the Southern. Figure 16 shows these angles, along with the coordinate system. The angular dependence is expressed in terms of the direction cosines:

$$l = \cos \delta \cos \phi \ , \tag{12}$$

$$m = \cos \delta \sin \phi \ , \tag{13}$$

$$n = - \sin \delta \ . \tag{14}$$

By using Budden's [1961] renormalization of the magnetic field, the field H in this appendix is, in fact, the magnetic field multiplied by the impedance of free space. The wave impedances are therefore dimensionless and should be multiplied by 377 Ω to put them into meter-kilogram-second units. The above normalization also removes the distinction between the magnetic and electric fields. We often combine the standard TE (E_y, H_x, H_z) or TM field components (H_y, E_x, E_z) into a generalized field called $\vec{F}$. That notation allows us to derive one set of equations that is applicable to both TE and TM modes.

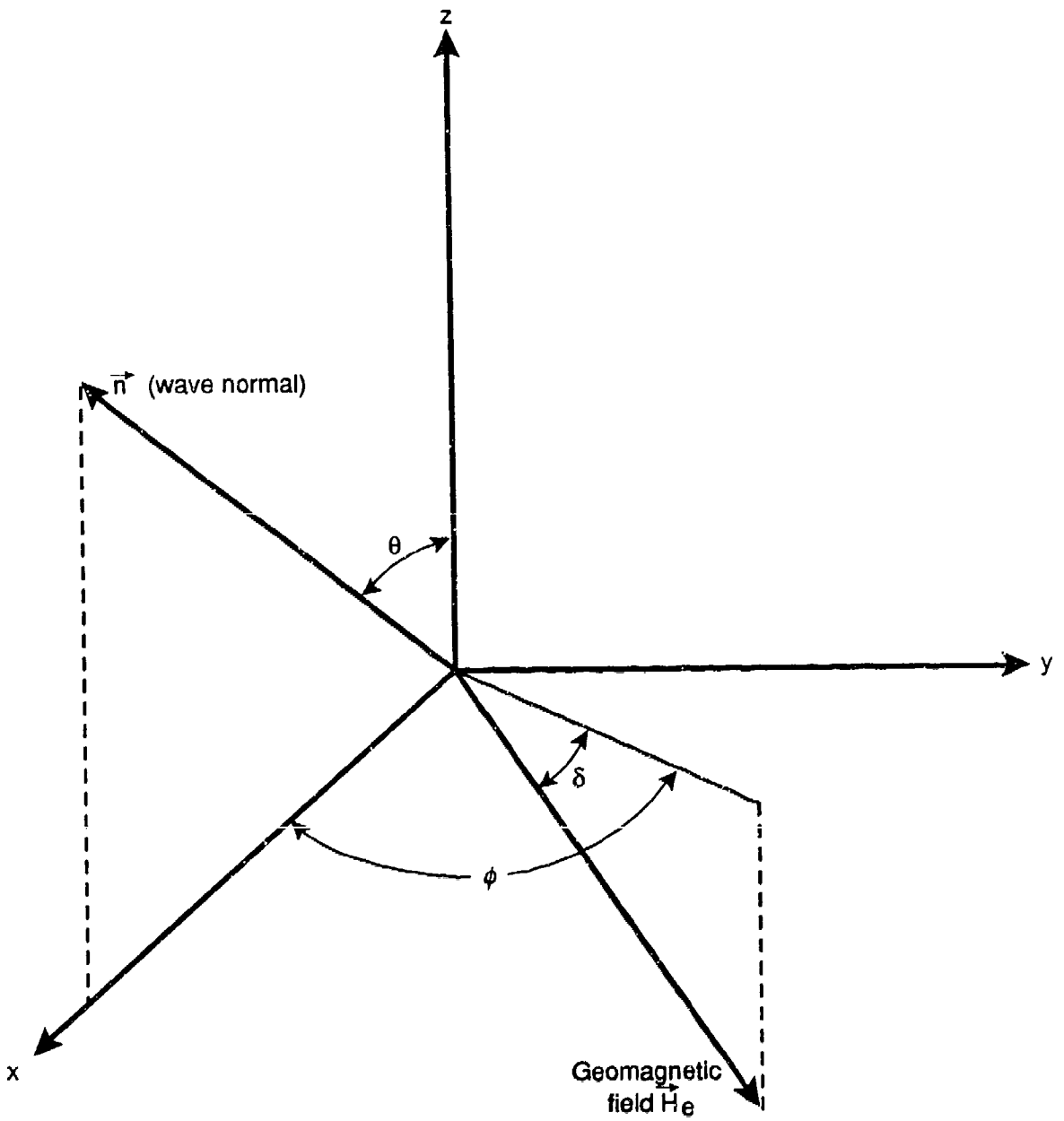

Figure 16. Coordinate system and angles of propagation.

MODEL.

We treat the earth as an isotropic conducting half-space below $z = 0$, characterized by the index of refraction:

$$n_g^2 = \epsilon_r - i \frac{\sigma_g}{\omega \epsilon_0} \quad . \tag{15}$$

The ionosphere is taken to be a possibly anisotropic half-space above $z = h$. The ionosphere is characterized by index of refraction:

$$n_i^2 = 1 - i \frac{\sigma_i}{\omega \epsilon_0} \quad , \tag{16}$$

in the isotropic case. It is characterized by the susceptibility matrix $\hat{M}$ in the anisotropic case, where

$$\hat{M} = - \frac{X}{U(U^2 - Y^2)} \begin{bmatrix} U^2 - l^2Y^2 & -inYU - lmY^2 & imYU - lnY^2 \\ inYU - lmY^2 & U^2 - m^2Y^2 & -ilYU - mnY^2 \\ -imYU - lnY^2 & ilYU - mnY^2 & U^2 - n^2Y^2 \end{bmatrix} \tag{17}$$

and X, Y, and U are the normal magneto-ionic parameters [see for example Ratcliffe (1959)]. They, and some other symbols used in the anisotropic case, are defined in Table 3. Note that in the isotropic case, where $Y/U \ll 1$, $\hat{M} \rightarrow (n_i - 1)\, \hat{I}$, where $\hat{I}$ is the identity matrix.

We assume that $\sigma_g \geq 10^{-5}$ S/m, but make no assumption about the ionosphere for the moment. We also assume that the region where the propagation conditions are laterally nonuniform is confined to the boundary region: $0 \leq x \leq \Delta x$. For smaller or larger values of x the conditions are constant. For our purposes, any changes in propagation conditions are considered to be continuous.

Table 3. Symbols: anisotropic ionospheric parameters.

Symbol	Definition
ω	$2\pi \times$ frequency (s^{-1})
H_e	earth's magnetic field (A/m)
l, m, n	direction cosines of earth's magnetic field (dimensionless)
e	charge of electron (1.6×10^{-19} coul)
m	mass of electron (9.1×10^{-31} kg)
ϵ_0	electric permittivity of free space (8.85×10^{-12} F/m)
μ_0	magnetic permeability of free space ($4\pi \times 10^{-7}$ H/m)
Z_0	characteristic impedance of free space = $(\mu_0/\epsilon_0)^{1/2}$ (377Ω)
N	electron density (m^{-3})
ν	collision frequency of electrons (s^{-1})
X	$Ne^2/\epsilon_0 m\omega^2 = \sigma_i \frac{\nu}{\epsilon_0 \omega^2}$, magneto-ionic parameter (dimensionless)
Y	$\mu_0 eH_e/m\omega$, magneto-ionic parameter (dimensionless)
U	$1 - i\frac{\nu}{\omega}$, magneto-ionic parameter (dimensionless)
C	propagation parameter, cosine of complex angle of incidence (dimensionless)
S	$\sqrt{1 - C^2}$, ImS < 0, sine of angle of incidence (dimensionless)
$\hat{M}$	susceptibility tensor for ionosphere (dimensionless)
ϕ	azimuth of propagation (measured east of north) (rad)
δ	geomagnetic field dip angle (positive in Northern Hemisphere) (rad)

NOTE: All units are in the International System of Units (SI).

We assume that the boundary is far enough from the transmitter that the total field is made up of a sum of fields of individual waveguide modes. For example, the electric field is

$$E_y = \sum_n E_{yn} \ . \tag{18}$$

MAXWELL'S EQUATIONS.

Using Budden's renormalization, we can write Maxwell's equations for the anisotropic case as

$$\vec{\nabla} \times \vec{E} = -ik\vec{H} \ , \tag{19}$$

$$\vec{\nabla} \times \vec{H} = ik\left(\hat{I} + \hat{M}\right) \vec{E} \ . \tag{20}$$

Here k is the wave number and is 2π/wavelength. For an isotropic ionosphere in the TE case these reduce to

$$H_x = \frac{1}{ik} \frac{\partial E_y}{\partial z} \ , \tag{21}$$

$$H_z = - \frac{1}{ik} \frac{\partial E_y}{\partial x} \ , \tag{22}$$

and

$$\left[ikn^2 - \frac{1}{ik} \frac{\partial^2}{\partial z^2}\right] E_y + \frac{\partial}{\partial x} H_z = 0 \ . \tag{23}$$

For the TM case, Maxwell's equations become:

$$ikn^2 E_x = - \frac{\partial H_y}{\partial z} \ , \tag{24}$$

$$ikn^2 E_z = \frac{\partial H_y}{\partial x} \quad , \tag{25}$$

and

$$-ikH_y + \frac{1}{ikn^2}\frac{\partial^2 H_y}{\partial z^2} + \frac{\partial E_z}{\partial x} = 0 \ . \tag{26}$$

LATERAL CHANGES IN PROPAGATION CONDITIONS: ISOTROPIC CASE.

In this section we generalize the work of Warber and Field [1987] so that it applies to lateral changes in ionospheric height as well as changes in ground conductivity. We use F_y, the y component of the field, in the region where conditions are not changing, i.e., $x < 0$. (Note that $F_y = E_y$ in the TE case and $F_y = H_y$ in the TM.) The form of F_y is well known; i.e.,

$$F_y = \sum_n f_n(z)\left[\Gamma_n e^{-ikSx} + R_n e^{ikSx}\right] \ . \tag{27}$$

Here $f_n(z)$ is the height gain function, $\Gamma_n e^{-ikSx}$ represents the forward-moving wave, and $R_n e^{ikSx}$ represents the backward-moving wave, i.e., that part of the wave reflected from the boundary. We normalize the height gain to one on the ground, so that the excitation (Γ_n) and reflection (R_n) factors represent the forward and backward field on the ground at $x = 0$.

In the region where conditions are spatially changing, we need a form that reduces to Eq. (27). Thus, for $x \geq 0$,

$$F_y = \sum_{n=1}^{\infty} f_n(z, x)\left[A_n(x) + B_n(x)\right] \ . \tag{28}$$

Here $A_n(x)$ represents the forward-moving wave; $B_n(x)$ represents the backward-moving wave; and $f_n(z, x)$ is the height gain, which is dependent on x. Here A_n and B_n are arbitrary functions of x. We place

restrictions on the height-gain term f_n and determine what form $A_n(x)$ and $B_n(x)$ must have to satisfy Maxwell's equations.

The restriction on f_n is that locally it must satisfy the wave equation

$$\left[\frac{\partial^2}{\partial z^2} + k^2 q^2(x, z)\right] f_n(z, x) = 0 \quad , \tag{29}$$

where $q^2 = n^2(x, z) - 1 + C_n^2$.

We discuss the height-gain term f_n in more detail below where we show that there exists a g_n that is orthogonal to f_n in the sense that

$$\int_{-\infty}^{\infty} g_n(z, x) f_m(z, x)\, dz = \Lambda_n(x)\delta_{nm} \quad . \tag{30}$$

The boundary conditions satisfied by f_n determine the modal equation that gives the value of C_n. Thus, the information about the propagation condition is contained in f_n, so we can restrict ourselves to the region within the waveguide ($0 \le z \le h$).

Equations (22) and (25) can be written:

$$F_z = -\frac{1}{ik}\frac{\partial}{\partial x} F_y \quad . \tag{31}$$

(So $F_z = H_z$ in the TE case and $F_z = -E_z$ in the TM case.) The form of F_z that is consistent with Eq. (28) and that reduces to the correct form for $x \le 0$ is

$$F_z = \sum_{n=1}^{\infty} f_n S_n \left(A_n - B_n\right) \quad . \tag{32}$$

We combine Eqs. (23) and (26) (in the waveguide) to give:

$$\left[ik - \frac{1}{ik}\frac{\partial^2}{\partial z^2}\right] F_y = -\frac{\partial}{\partial x} F_z \ . \tag{33}$$

The functions $A_n(x)$ and $B_n(x)$ must satisfy Eqs. (31) and (33). To find out what this requires of $A_n(x)$ and $B_n(x)$, we use Eqs. (28) and (32), multiply by the orthogonal function g_n and integrate over z from $-\infty$ to $+\infty$. Using Eq. (29) gives, after some algebra (here, a prime symbol denotes the differentiation with respect to x),

$$A_n' + B_n' + ikS_n\left(A_n - B_n\right) + \sum_{m=1}^{\infty} K_{mn}\left(A_m + B_m\right) = 0 \ , \tag{34}$$

$$A_n' - B_n' + ikS_n\left(A_n + B_n\right) + \frac{S_n'}{S_n}\left(A_n - B_n\right) + \sum_{m=1}^{\infty} K_{mn}\left(A_m - B_m\right)\frac{S_m}{S_n} = 0 \ . \tag{35}$$

Here,

$$K_{mn} = \frac{1}{\Lambda_n}\int_{-\infty}^{\infty} f_m'(z)\, g_n(z)\, dz \ . \tag{36}$$

Adding Eqs. (34) and (35) yields:

$$A_n' + ikS_nA_n + \frac{S_n'}{2S_n}\left(A_n - B_n\right) + \frac{1}{2}\sum_{m=1}^{\infty}\left[A_m\left(1 + \frac{S_m}{S_n}\right)\right.$$

$$\left. + B_m\left(1 - \frac{S_m}{S_n}\right)\right] K_{mn} = 0 \ . \tag{37}$$

Subtracting those equations from each other gives

$$B_n' - ikS_nB_n - \frac{S_n'}{2S_n}\left(A_n - B_n\right) + \frac{1}{2}\sum_{m=1}^{\infty}\left[A_m\left(1 - \frac{S_m}{S_n}\right)\right.$$

$$\left. + B_m\left(1 + \frac{S_m}{S_n}\right)\right] K_{mn} = 0 \ . \tag{38}$$

Now we define A and B in terms of a and b, which are functions that vary more slowly with respect to x, and we let

$$A_n = \frac{a_n(x)}{\sqrt{S_n(x)}} \exp\left[-ik \int_0^x S_n(\chi)\, d\chi\right] , \tag{39}$$

and

$$B_n = \frac{b_n(x)}{\sqrt{S_n(x)}} \exp\left[ik \int_0^x S_n(\chi)\, d\chi\right] . \tag{40}$$

Thus Eqs. (37) and (38) become

$$a_n' - \frac{1}{2}\frac{S_n'}{S_n} b_n \exp\left[2ik \int_0^x S_n(\chi)\, d\chi\right]$$

$$+ \frac{1}{2}\sum_{m=1}^{\infty}\left[\left(\frac{S_n + S_m}{\sqrt{S_n\, S_m}}\right) a_m \exp\left\{-ik \int_0^x \left[S_m(\chi) - S_n(\chi)\right] d\chi\right\}\right.$$

$$\left. + \left(\frac{S_n - S_m}{\sqrt{S_n\, S_m}}\right) b_m \exp\left\{ik \int_0^x \left[S_m(\chi) + S_n(\chi)\right] d\chi\right\}\right] K_{mn} = 0 \ , \tag{41}$$

$$b_n' - \frac{1}{2}\frac{S_n'}{S_n} a_n \exp\left[-2ik \int_0^x S_n(\chi)\, d\chi\right]$$

$$+ \frac{1}{2}\sum_{m=1}^{\infty}\left[\left(\frac{S_n - S_m}{\sqrt{S_n S_m}}\right) a_m \exp\left\{-ik \int_0^x \left[S_m(\chi) + S_n(\chi)\right] d\chi\right\}\right.$$

$$\left. + \left(\frac{S_n + S_m}{\sqrt{S_n S_m}}\right) b_m \exp\left\{ik \int_0^x \left[S_m(\chi) - S_n(\chi)\right] d\chi\right\}\right] K_{mn} = 0 \ , \qquad (42)$$

Equations (39) and (40) would be the WKB approximation if $a_n(x)$ and $b_n(x)$ were constants. Thus, Eqs. (41) and (42) become the second-order WKB approximation. Up to this point, we have made no approximations. In Warber and Field [1987], direct calculation showed that the reflection term is very small for changes in ground conductivity. Here we argue that the same is true for any other changes we make. This is, at any rate, the standard assumption made. We therefore neglect reflections, which means we can set $b_m = 0$ in Eq. (41).

Removing the nth term from the summation in Eq. (41) yields:

$$a_n' + a_n K_{nn} + \frac{1}{2}\sum_{\substack{m=1 \\ m\neq n}}^{\infty}\left(\frac{S_n + S_m}{\sqrt{S_m S_n}}\right) a_m \exp\left\{-ik \int_0^x \left[S_m(\chi) - S_n(\chi)\right] d\chi\right\} K_{mn} = 0 \ . \qquad (43)$$

That reduces to a very simple form if we let

$$a_n(x) = \alpha_n(x) \exp\left[-\int_0^x K_{nn}\, d\chi\right] \ . \qquad (44)$$

Then Eq. (43) is

$$\alpha_n'(x) = \sum_{\substack{m=1 \\ m\neq n}}^{\infty} \gamma_{nm}(x)\ \alpha_m(x) \ , \tag{45}$$

where for, $m \neq n$,

$$\gamma_{mn} = -\frac{1}{2}\left[\frac{S_n + S_m}{\sqrt{S_m\ S_n}}\right] \exp\left[\int_0^x (K_{nn} - K_{mm})\ d\chi\right]$$

$$\times \exp\left[-ik \int_0^x (S_m - S_n)\ d\chi\right] K_{mn} \ . \tag{46}$$

We can integrate Eq. (45) directly, then:

$$\alpha_n(x) = \alpha_n(0) + \sum_{\substack{m=1 \\ m\neq n}}^{\infty} \int_0^x \gamma_{nm}(\chi)\ \alpha_m(\chi)\ d\chi \ . \tag{47}$$

We can solve Eq. (47) as we would a perturbation or scattering series. That is, we can use Eq. (47) to find $\alpha_m(\chi)$ and substitute this into the integral, getting:

$$\alpha_n(x) = \alpha_n(0) + \sum_{\substack{m=1 \\ m\neq n}}^{\infty} \alpha_m(0) \int_0^x \gamma_{nm}(\chi)\ d\chi$$

$$+ \sum_{\substack{m=1 \\ m\neq n}}^{\infty} \sum_{\substack{\ell=1 \\ \ell\neq m}}^{\infty} \int_0^x d\chi\ \gamma_{nm}(\chi) \int_0^\chi \gamma_{m\ell}(\tau)\ \alpha_\ell(\tau)\ d\tau \ . \tag{48}$$

We can repeat this process an arbitrary number of times. If we define $\gamma_{nn}(x) \equiv 0$, and assume summation over repeated symbols, the notation is simpler:

$$\alpha_n(x) = \alpha_n(0) + G_{nm}^{(1)}\ \alpha^m(0) + G_{nm}^{(2)}\ \alpha^m(0) + G_{nm}^{(3)}\ \alpha^m(0) + \cdots \qquad (49)$$

where

$$G_{nm}^{(1)}(x) = \int_0^x \gamma_{nm}(\chi)\ d\chi\ , \qquad (50)$$

$$G_{nm}^{(2)}(x) = \sum_{\ell} \int_0^x d\chi\ \gamma_{n\ell}(\chi)\ G_{\ell m}^{(1)}\ (\chi)\ , \qquad (51)$$

and, in general:

$$G_{nm}^{(i)}(x) = \sum_{\ell} \int_0^x d\chi\ \gamma_{n\ell}(\chi)\ G_{\ell m}^{(i-1)}\ (\chi)\ . \qquad (52)$$

For $x = 0$, and ignoring reflections, we have, from Eq. (27):

$$F_y = \sum_{n=1}^{\infty} \Gamma_n f_n(z)\ . \qquad (53)$$

At $x = 0$, we have, from Eq. (28):

$$F_y = \sum_{n=1}^{\infty} f_n(z,\ 0) A_n(0)\ . \qquad (54)$$

Equations (53) and (54) must be equal. So, since from Eq. (39) and Eq. (44),

$$A_n(0) = a_n(0)/\sqrt{S_n(0)} = \alpha_n(0)/\sqrt{S_n(0)} \ , \tag{55}$$

we see that

$$\alpha_n(0) = \Gamma_n \sqrt{S_n(0)} \ . \tag{56}$$

That is the initial condition on α.

Putting this all together gives, for $0 \le x \le \ell$,

$$F_y(x, z) = \sum_{n=1}^{\infty} \Gamma_n \left[1 + Q_n(x)\right] \sqrt{\frac{S_n(0)}{S_n(x)}} \exp\left(+ \int_0^x K_{nn}\, d\chi\right)$$

$$\cdot f_n(x, z) \exp\left[-ik \int_0^x S_n(\chi)\, d\chi\right] \tag{57}$$

In Eq. (57), we define the mode-coupling factor Q_n as:

$$Q_n = \sum_i Q_n^{(i)} \ , \tag{58}$$

and

$$Q_n^{(i)}(x) = \sum_{\substack{m=1 \\ m \neq n}}^{\infty} G_{nm}^{(i)}(x) \sqrt{\frac{S_m(0)}{S_n(0)}} \ \frac{\Gamma_m}{\Gamma_n} + G_{nn}^{(i+1)} \ . \tag{59}$$

Here $Q_n^{(i)}$ represents the ith order scattering. In the limit, as Γ_n goes to zero, we have:

$$\Gamma_n[1 + Q_n(x)] = \sum_{m=1}^{\infty} \sum_{i=1} G_{nm}^{(i)}(x) \sqrt{\frac{S_m(0)}{S_n(0)}}\, \Gamma_m \ . \tag{60}$$

TE HEIGHT GAIN AND MODAL EQUATIONS FOR ISOTROPIC CASE.

In the TE case, we write the height-gain function as $e_n(z)$. Recall that it is a solution to Eq. (29). The boundary conditions require that e_n and

$$\frac{1}{ik} \frac{\partial}{\partial z} e_n \ , \tag{61}$$

be continuous across the boundaries at $z = 0$ and $z = h$.

The solutions of Eq. (29) that satisfy these conditions as well as the radiation condition (i.e., that the field must go to zero at infinity), and have $e_n(0) = 1$ are:

$$e_n = \begin{cases} \dfrac{Z_i}{Z_g} \left(\dfrac{CZ_g - 1}{CZ_i + 1} \right) e^{-iCkh}\, e^{-iq_i k(z-h)} & \text{for } z \geq h \ , \quad (62) \\ \cos Ckz + i \dfrac{q_g}{C} \sin Ckz & \text{for } 0 < z < h \ , \quad (63) \\ e^{iq_g kz} & \text{for } z \leq 0 \ , \quad (64) \end{cases}$$

where

$$Z_g \equiv \frac{1}{q_g} \ , \tag{65}$$

and

$$Z_i \equiv \frac{1}{q_i} \ . \tag{66}$$

Recall that the solution to Eq. (29) is a superposition of up- and down-going waves whose amplitudes are constants to be determined by the boundary conditions. Thus, in the three regions there are six

constants. Two of them are determined by the radiation condition and one by the normalization condition. In reality, the boundary conditions at $z = 0$ and $z = h$ determine four more constants, but there are only three to be determined. That fact places a restriction on the value of C, which is expressed by the modal equation:

$$\frac{CZ_g + 1}{CZ_g - 1} = \frac{CZ_i - 1}{CZ_i + 1} e^{-2iCkh} \quad . \tag{67}$$

Note that we can write Eq. (67) as

$$iC\left(Z_i + Z_g\right) \cos Ckh = \left(1 + C^2 Z_i Z_g\right) \sin Ckh \quad . \tag{68}$$

The last form is particularly easy to solve numerically. When σ_g is very large, Z_g is very small, so:

$$iCZ_i \cos Ckh \approx \sin Ckh \quad . \tag{69}$$

To zeroth order in Z_i, $C_n^{(0)} \approx n\pi/kh$, while to first order

$$C_n^{(1)} \approx C_n^{(0)} \left(\frac{1}{1 - iZ_i/kh}\right) \quad . \tag{70}$$

We solve Eq. (68) numerically using the Newton-Raphson method starting with $C = C_n^{(1)}$.

TM HEIGHT GAIN AND MODAL EQUATIONS FOR ISOTROPIC CASE.

In this case, the height-gain function is written as $h_n(z)$ and the boundary conditions require that h_n and

$$-\frac{1}{ikn^2} \frac{\partial}{\partial z} h_n \quad , \tag{71}$$

be continuous across the boundaries. This gives:

$$h_n(z, x) = \begin{cases} \dfrac{C - Z_g}{C + Z_i} e^{-iCkh} e^{-iq_i k(z-h)} & \text{for } z \geq h , \quad (72) \\ \cos Ckz + i \dfrac{Z_g}{C} \sin Ckz & \text{for } 0 < z < h, \quad (73) \\ e^{iq_g kz} & \text{for } z \leq 0 , \quad (74) \end{cases}$$

where $Z_g \equiv q_g/n_g^2$, (75)

$Z_i \equiv q_i/n_i^2$, (76)

and the modal equation is:

$$\frac{C + Z_g}{C - Z_g} = \frac{C - Z_i}{C + Z_i} e^{-2iCkh} . \quad (77)$$

Equation (77) may also be written:

$$iC\left(Z_i + Z_g\right) \cos Ckh = \left(C^2 + Z_i Z_g\right) \sin Ckh . \quad (78)$$

The zeroth order solution for small Z_g is then

$$C_n^{(0)} = \left(n - \frac{1}{2}\right) \frac{\pi}{kh} , \quad (79)$$

and the first order is

$$C_n^{(1)} = C_n^{(0)} \left(1 - \frac{1}{1 + iZ_i kh}\right) . \quad (80)$$

ORTHOGONAL FUNCTION $g_n(z)$.

In Eqs. (34) and (35) we eliminated the height-gain function f_n by multiplying by g_n and integrating over all z. In this section we determine the form of $g_n(x)$ for the TE and TM cases.

In the TE case, since e_n is a solution of Eq. (29), we can write

$$e_m \frac{\partial^2}{\partial z^2} e_n - e_n \frac{\partial^2}{\partial z^2} e_m + k^2\left[C_n^2 - C_m^2\right] e_n e_m = 0 \ . \tag{81}$$

If $n \neq m$, then

$$\int_{-\infty}^{\infty} e_n e_m \, dx = \frac{1}{k^2\left[C_n^2 - C_m^2\right]} \int_{-\infty}^{\infty} \frac{\partial}{\partial z}\left[e_m \frac{\partial}{\partial z} e_n - e_n \frac{\partial}{\partial z} e_m\right] dz$$

$$= \frac{1}{k^2\left[C_n^2 - C_m^2\right]} \left[\left[e_m^{(i)} \frac{\partial}{\partial z} e_n^{(i)} - e_n^{(i)} \frac{\partial}{\partial z} e_m^{(i)}\right]\Big|_{z\to\infty}\right.$$

$$- \left[e_m^{(i)} \frac{\partial}{\partial z} e_n^{(i)} - e_n^{(i)} \frac{\partial}{\partial z} e_m^{(i)}\right]\Big|_{z=h}$$

$$+ \left[e_m^{(0)} \frac{\partial}{\partial z} e_n^{(0)} - e_n^{(0)} \frac{\partial}{\partial z} e_m^{(0)}\right]\Big|_{z=h}$$

$$- \left[e_m^{(0)} \frac{\partial}{\partial z} e_n^{(0)} - e_n^{(0)} \frac{\partial}{\partial z} e_m^{(0)}\right]\Big|_{z=0}$$

$$+ \left[e_m^{(g)} \frac{\partial}{\partial z} e_n^{(g)} - e_n^{(g)} \frac{\partial}{\partial z} e_m^{(g)}\right]\Big|_{z=0}$$

$$\left. - \left[e_m^{(g)} \frac{\partial}{\partial z} e_n^{(g)} - e_n^{(g)} \frac{\partial}{\partial z} e_m^{(g)}\right]\Big|_{z\to -\infty}\right] , \tag{82}$$

where the superscripts i, 0, g indicate the height gain function in the ionosphere, the waveguide, and the ground, respectively.

The radiation conditions ensure that $e_m \to 0$ as $z \to \pm\infty$. The fact that e_m and $\partial e_n/\partial z$ are continuous across the boundary at $z = h$, and $z = 0$ means that there is no contribution to the integral at those boundaries. Thus, for the TE case, $g_n(z) = e_n(z)$.

In the TM case $\partial h_n/\partial z$ is not continuous across the boundaries at $z = 0$, $z = h$, but the following is:

$$\frac{1}{n^2} \frac{\partial}{\partial z} h_n \ .$$

Thus if we write*

$$g_n = \frac{1}{n^2} h_n \ , \tag{83}$$

$$\int_{-\infty}^{\infty} g_n h_m \, dz = \frac{1}{n_g^2} \int_{-\infty}^{0} h_n h_m \, dz + \int_{0}^{h} h_n h_m \, dz + \frac{1}{n_i^2} \int_{h}^{\infty} h_n h_m \, dz \ . \tag{84}$$

Then proceeding as in Eq. (82) gives

$$\int_{-\infty}^{\infty} g_n h_m \, dz = 0 \text{ if } n \neq m \ . \tag{85}$$

*This point was dropped inadvertently from Warber and Field [1987]. However, the results for Λ_n and K_{nm} in the TM case do include the correct term.

RESULTS FOR LATERAL CHANGES OF GROUND CONDUCTIVITY.

This is the case discussed in Warber and Field [1987]; now we present the results, updated to include the term that corresponds to integration from $z = -\infty$ to $z = 0$. Note that many quantities we use are dependent on C and hence are mode dependent. In order to cut down on the number of subscripts, we often suppress the mode number subscript on those quantities that already have a subscript such as q_g, Z_g, etc. We do this only in those cases where the mode number is clear from the content, such as in equations that depend only on one mode. We do use the mode number subscript in those situations, such as equations that depend on two modes, where it would be ambiguous not to do so.

In the TE case:

$$\Lambda_n(x) = \frac{1}{2ik}\left\{\frac{1}{q_g} + \left(ikh + Z_i\right)\left[1 - \left(\frac{q_g}{C}\right)^2\right]\right\} . \tag{86}$$

In the TM case:

$$\Lambda_n(x) = \frac{1}{2ik}\left\{\frac{1}{n_g^2 q_g} + \left[ikh + \left(\frac{C^2}{q_i n_i^2} - Z_i\right)\frac{1}{C^2 - Z_i^2}\right]\left[1 - \left(\frac{Z_g}{C}\right)^2\right]\right\} . \tag{87}$$

In Eqs. (86) and (87) the first term inside the braces is due to the ground integration. And for $n \neq m$, we can write

$$K_{nm} = + \frac{1}{\Lambda_m}\frac{1}{ik\left(C_m^2 - C_n^2\right)}\frac{\partial}{\partial x}\zeta(x) , \tag{88}$$

where $\zeta(x) = q_g$ in the TE case and $\zeta(x) = Z_g$ in the TM.

To calculate $K_{nn}(x)$ we note that in the TE case,

$$K_{nn}(x) = \frac{1}{\Lambda_n}\int_0^\infty e_n'(z)e_n(z)\,dz . \tag{89}$$

However, from Eq. (30) we see that

$$\Lambda_n'(x) = 2 \int_{-\infty}^{\infty} e_n'(z) e_n(z)\, dz \ . \tag{90}$$

So,

$$K_{nn} = \frac{1}{2\Lambda_n} \Lambda_n' \ , \tag{91}$$

and hence,

$$\int_0^x K_{nn}\, d\chi = \frac{1}{2} \ell n \left[\Lambda_n(x)/\Lambda_n(0)\right] \ , \tag{92}$$

and also

$$\exp\left(-\int_0^x K_{nn}\, d\chi\right) = \sqrt{\frac{\Lambda_n(0)}{\Lambda_n(x)}} \ . \tag{93}$$

In the TM case,

$$\Lambda_n'(x) = 2 \int_{-\infty}^{\infty} \frac{1}{n^2} h_n' h_n\, dz - \frac{\left(n_g^2\right)'}{\left(n_g^2\right)^2} \int_{-\infty}^{0} h_n^2\, dz \tag{94}$$

$$= 2\, \Lambda_n(x) K_{nn} - \frac{\left(n_g^2\right)'}{\left(n_g^2\right)^2} \frac{1}{2ikq_g} \ . \tag{95}$$

Now the second term is much smaller than 1, whereas $\Lambda_n \sim h/2$ and $K_{nn} \sim 1$. Thus we can ignore it. And so Eq. (93) is good for the TM case also.

RESULTS FOR LATERAL CHANGES IN IONOSPHERE HEIGHT.

The effect of changing the height of the ionosphere is considered. Here we assume that h is a continuous function of x. From either modal equation [Eqs. (67) or (77)] it is clear that changing h changes C. We can determine how much C changes by taking the derivative of the modal equations with respect to x. This gives, in the TE case,

$$C' = \frac{-iCkh'}{Z_g + Z_i + ikh} \cdot \tag{96}$$

Recall in the TE case that $Z = 1/q$. If we assume that $|Z_g| \ll 1$ and $|Z_i| \ll kh$, which is true if $\sigma_i \gtrsim 10^{-6}$ S/m and frequency is above 10 kHz, then a useful approximate solution for Eq. (96) is

$$C = C_o \frac{h_o}{h} \exp\left[-iZ_i \left(\frac{1}{kh} - \frac{1}{kh_o}\right)\right] , \tag{97}$$

where C_o is calculated from the modal equation with $h = h_o$. In the TM case,

$$C' = \frac{-iCkh'}{ikh - \frac{1}{\Xi_g Z_g} - \frac{1}{\Xi_i Z_i}} \tag{98}$$

where $$Z_g = \frac{q_g}{n_g^2} , \quad Z_i = \frac{q_i}{n_i^2} , \quad \Xi_g = C^2(n_g^2 + 1) - 1; \text{ etc.}$$

The approximate solution of Eq. (98) has its leading term,

$$C = C_o \frac{h_o}{h} , \tag{99}$$

which is the same as Eq. (97). However, the range over which this is valid is not very useful (typically $C \lesssim 0.3$, frequency > 40 kHz, $\sigma_i > 10^{-5}$ S/m) and so we will not use it. Since Eq. (30) does not depend on the kind of change, it is clear that the Λ_n are the same as in the previous case. To calculate K_{nm} for the TE case we write Eq. (36) as

$$K_{mn} = \frac{1}{\Lambda_n} \int_{-\infty}^{\infty} e_n(z) e_m'(z)\, dz \ , \tag{100}$$

where $e_n(z)$ is defined in Eqs. (62) to (64).

To compute this, note that

$$\left[\frac{\partial^2}{\partial z^2} + k^2 q_n^2\right] e_n = 0 \ . \tag{101}$$

If we take the derivative with respect to x, then

$$\left[\frac{\partial^2 e_m'}{\partial z^2} + 2k^2 q_m q_m' e_m + k^2 q_m^2 e_m'\right] = 0 \ . \tag{102}$$

If $n \neq m$, we can combine these to give

$$k^2\left[q_n^2 - q_m^2\right] e_m' e_n$$

$$= - e_m' \frac{\partial^2}{\partial z^2} e_n + e_n \frac{\partial^2}{\partial z^2} e_m' - 2k^2 q_m q_m' e_n e_m \ , \tag{103}$$

or

$$\int_{-\infty}^{\infty} e'_m e_n \, dz = \frac{1}{k^2\left(C_n^2 - C_m^2\right)} \left[\int_{-\infty}^{\infty} \frac{\partial}{\partial z}\left(e_n \frac{\partial}{\partial z} e'_m - e'_m \frac{\partial}{\partial z} e_n\right) dz \right.$$

$$\left. + 2k^2 \int_{-\infty}^{\infty} q_m q'_m e_n e_m \, dz\right] . \qquad (104)$$

Consider the last integration in the bracket:

$$\int_{-\infty}^{\infty} q_m q'_m e_m e_n \, dz . \qquad (105)$$

Note that n^2 does not depend on x within a layer, and since we do not move across boundaries in the x-direction, we see that $q_m^2 = n^2 - 1 + c_n^2$ gives $q_m q'_m = C_m C'_m$ and thus Eq. (105) becomes:

$$C_m C'_m \int_{-\infty}^{\infty} e_m e_n \, dz = 0 \qquad (106)$$

since the modes are orthogonal, and so Eq. (104) becomes

$$\int_{-\infty}^{\infty} e'_m e_n \, dz = \frac{1}{k^2\left(C_n^2 - C_m^2\right)} \left\{e_n^i(h)\left[\frac{\partial e_m^{o'}(h)}{\partial z} - \frac{\partial e_m^{i'}(h)}{\partial z}\right]\right.$$

$$+ \frac{\partial e_n^i(h)}{\partial z}\left[e_m^{i'}(h) - e_m^{o'}(h)\right] + \left[\frac{\partial e_m^{g'}(0)}{\partial z} - \frac{\partial e_m^{o'}(0)}{\partial z}\right]$$

$$\left. + \frac{\partial e_n^g(0)}{\partial z}\left[e_m^{o'}(0) - e_m^{g'}(0)\right]\right\} . \qquad (107)$$

Here the superscripts i, o, and g indicate the field calculated in the ionosphere, waveguide and ground respectively. We have made use here of the continuity of e and $\partial e/\partial z$ at the boundaries. Now, $e'(z)$ is also continuous at both boundaries, and $\partial e'/\partial z$ are continuous at $z = 0$. So Eq. (107) reduces to

$$\int_{-\infty}^{\infty} e'_m e_n \, dz = \frac{1}{k^2\left(C_n^2 - C_m^2\right)} e_n(h) \left[\frac{\partial e_m^{o'}(h)}{\partial z} - \frac{\partial e_m^{i'}(h)}{\partial z}\right] , \tag{108}$$

but we can show that

$$\frac{\partial e_m^{o'}(h)}{\partial z} = iC'_m C_m k \left(Z_{gm} + ikh\right) e_m(h) , \tag{109}$$

$$\frac{\partial e_m^{i'}(h)}{\partial z} = i \frac{C'_m}{C_m} k \left[q_{im}^2 \left(Z_{im} + Z_{gm} + ikh\right) - \frac{C_m^2}{q_{im}}\right] e_m(h) . \tag{110}$$

So substituting these in Eq. (108)

$$\int_{-\infty}^{\infty} e'_m e_n \, dz = \frac{1}{k^2\left(C_n^2 - C_m^2\right)} e_n(h) e_m(h) i \frac{C'_m}{C_m} k$$

$$\times \left(C_m^2 - q_{im}^2\right)\left(Z_{im} + Z_{gm} + ikh\right) , \tag{111}$$

but making use of Eq. (96) gives

$$K_{mn} = \frac{1}{\Lambda_n} \frac{1}{\left(C_n^2 - C_m^2\right)} e_n(h) e_m(h) \left(1 - n_i^2\right) h' . \tag{112}$$

The case of K_{nn} is handled in the same way as the earlier case. That is

$$K_{nn}(x) = \frac{1}{2} \frac{\Lambda_n'}{\Lambda_n} \ . \tag{113}$$

To calculate K_{mn} for the TM case, we write Eq. (36) as

$$K_{mn} = \frac{1}{\Lambda_n} \int_{-\infty}^{\infty} \frac{1}{n^2} h_n(z) h_m'(z) \, dz \ , \tag{114}$$

where $h_n(z)$ is defined in Eqs. (72) to (74). As before, we can write equations analogous to Eqs. (102) and (103). Thus we can write:

$$\int_{-\infty}^{\infty} \frac{1}{n^2} h_n(z) h_m'(z) \, dz$$

$$= \frac{1}{k^2\left(C_n^2 - C_m^2\right)} \left[\int_{-\infty}^{\infty} \left(\frac{1}{n^2} \frac{\partial}{\partial z} h_n \frac{\partial}{\partial z} h_m' - h_m' \frac{\partial}{\partial z} h_n \right) dz \right.$$

$$\left. + \int_{-\infty}^{\infty} \frac{1}{n^2} q_m q_m' h_n h_m \, dz \right] \ . \tag{115}$$

Again the last integral reduces to

$$C_m C_m' \int_{-\infty}^{\infty} \frac{1}{n^2} h_n h_m \, dz \ , \tag{116}$$

which we have shown is zero. The first integral is done by breaking the integration into the three ranges, and so:

$$\int_{-\infty}^{\infty} \frac{1}{n^2} h_n h'_m \, dz \; , = \frac{1}{k^2\left(C_n^2 - C_m^2\right)} \left\{ h_n^i(h) \left[\frac{\partial h_m^{o'}(h)}{\partial z} - \frac{1}{n_i^2} \frac{\partial h_m^{i'}(h)}{\partial z} \right] \right.$$

$$+ \frac{\partial h_n^i(h)}{\partial z} \left[h_m^{i'}(h) - h_m^{o'}(h) \right] + \left[\frac{1}{n_g^2} \frac{\partial h_m^{g'}(h)}{\partial z} - \frac{\partial h_m^{o'}(h)}{\partial z} \right]$$

$$\left. + \frac{\partial h_m^g(h)}{\partial z} \left[h_m^{o'}(0) - h_m^{g'}(0) \right] \right\} . \qquad (117)$$

Here we have made use of the fact that h and $1/n^2 \times \partial h/\partial z$ are continuous at the boundaries and that $h(0) = 1$. As it turns out, $1/n^2 \times \partial h'/\partial z$ and h' are also continuous at $z = 0$. It can be shown that

$$h_m^{i'}(h) = h_m^{o'}(h) - \frac{n_i^2 - 1}{n_i^2} \frac{C'_m}{C_m} \left(\frac{1}{\Xi_{gm}} - \frac{1}{\Xi_{im}} \right) h_m^i(h) \; , \qquad (118)$$

and

$$\frac{\partial h_m^{o'}(h)}{\partial z} = - i \frac{C'}{C} k h_m^i(h) \left[Z_i \left(1 + \frac{1}{\Xi_g} \right) - c^2 \frac{1}{Z_i \Xi_i} \right]$$

$$+ C_m^2 k^2 h' h_m^i(h) \; , \qquad (119)$$

$$\frac{\partial h_m^{i'}(h)}{\partial z} = - \left[q_i k \frac{C'_m}{C_m} \left(\frac{1}{\Xi_{gm}} - \frac{1}{\Xi_{im}} \right) + i \frac{C_m C'_m}{n_i^2 q_i^2} k - C_m^2 k^2 h' \right] h_m^i(h) \; . \qquad (120)$$

Substituting these equations into Eq. (117) gives, for $m \neq n$:

$$K_{mn} = \frac{1}{\Lambda_n} \frac{1}{\left(C_n^2 - C_m^2\right)} \frac{n_i^2 - 1}{n_i^2} \left[C_m^2 - 1 + \frac{1}{n_i^2} q_{in} q_{im} \right]$$

$$\times h_m(h) h_n(h) h' \ . \qquad (121)$$

To find K_{nn} we can use the same logic as in Eq. (91). Note that, in this case, the conductivities are not functions of x. Results using these equations are presented in Sec. 3.

NIGHT PROPAGATION.

In this section we discuss propagation under nighttime ionospheres. We derive a method to quickly find the directional dependence of the attenuation, and we derive the height gain functions.

It is clear from the susceptibility matrix $\hat{M}$ (Eq. 17) that the effect of the earth's magnetic field on propagation is contained in the ratio of the magneto-ionic parameters, Y and U. For any given frequency Y is a constant in the range 25 to 150, if the frequency is 60 to 10 kHz; U, however, changes with altitude.

During ambient day or disturbed conditions, very low frequency electromagnetic waves are reflected from the ionosphere at altitudes where the electron-neutral collision frequency ν is much larger than the wave frequency ω. Hence:

$$|U| = \left|1 - i \frac{\nu}{\omega}\right| \simeq \left|\frac{\nu}{\omega}\right| \gg 1 \ , \qquad (122)$$

and so,

$$\left|\frac{Y}{U}\right| \ll 1 \ .$$

This means that the effect of the earth's magnetic field is small. At night, however, the waves are reflected at higher altitudes, and ν decreases exponentially with a scale height of about 6.7 km. At about 85 km, ν becomes on the order of ω. (The exact height of course depends on ω.)

If we write

$$Y = \frac{\omega_g}{\omega} , \tag{123}$$

where ω_g is called the gyro frequency and is about 9.3×10^6 s^{-1}, then

$$\frac{Y}{U} = \frac{\omega_g}{\omega - i\nu} \simeq i \frac{\omega_g}{\nu} , \tag{124}$$

for any altitude below about 80 km. If we use the standard model for collision frequency:

$$\nu = 1.8 \times 10^{11} \, e^{-z/(6.67 \text{ km})} s^{-1} , \tag{125}$$

then ν is on the order of ω_g around 66 km. This means that we can regard $\mathcal{Y} \equiv Y/U$ as independent of frequency below 80 km. Let us look at the other extreme where

$$Y \simeq \frac{\omega_g}{\omega} >> 1 . \tag{126}$$

Each element in the susceptibility matrix $\hat{M}$ (Eq. 17) has a denominator of $1 + \mathcal{Y}^2 \simeq \mathcal{Y}^2$. Since the numerator of the elements of $\hat{M}$ are proportional to either $\mathcal{Y}^2$ or $\mathcal{Y}$, the elements of $\hat{M}$ reduce to either 0 or a value on the order of 1, depending on the direction cosines. Again, these are independent of frequency. Thus, it appears we can find a parameter $\mathcal{Y}$ which, like σ_i, is independent of frequency and characterizes the propagation medium.

We write the susceptibility matrix (Eq. 17) as:

$$\hat{M} = -\frac{X}{U}\,\frac{1}{1-y^2}\begin{bmatrix} 1-l^2y^2 & -in y - lmy^2 & imy - lny^2 \\ iny - lmy^2 & 1-m^2y^2 & -ily - mny^2 \\ -imy - lny^2 & ily - mny^2 & 1-n^2y^2 \end{bmatrix}. \tag{127}$$

As an example of what this matrix looks like, Fig. 17 plots the $\hat{M}$ with the -X/U term divided out, as a function of height. We assume that the direction of propagation is from west to east (ϕ = 90 deg), that the magnetic dip angle is 60 deg, and ν is given by Eq. (125).

Note that below about 50 and above 80 km, the propagation conditions (at least with respect to the magnetic effects) are constant, and that the major changes in conditions occur between 60 and 70 km.

We plot the real part of $\hat{M}$ in Fig. 17 since the imaginary part is very small, and we want to emphasize the sign of the elements of $\hat{M}$. Although we have used 30 kHz to plot the figures, the shape of the plots is in fact almost independent of frequency.

If we had plotted east to west propagation (ϕ = 270 deg) then the M_{13}, M_{31}, M_{23}, and M_{32} elements would change sign. This causes a change in the value of the propagation constant C, which satisfies the modal condition. This difference in C is reflected in a very noticeable difference in the attenuation rate. In order to predict this attenuation within our propagation models, we must derive an expression for the modal equation.

MAXWELL'S EQUATIONS.

In order to determine the modal equation for night propagation, we need to determine the fields within an anisotropic layer. As in the isotropic case, once the form of the fields in the ionosphere is found we can connect them to the fields in the regions below the ionosphere and then find the relationship among the fields that is

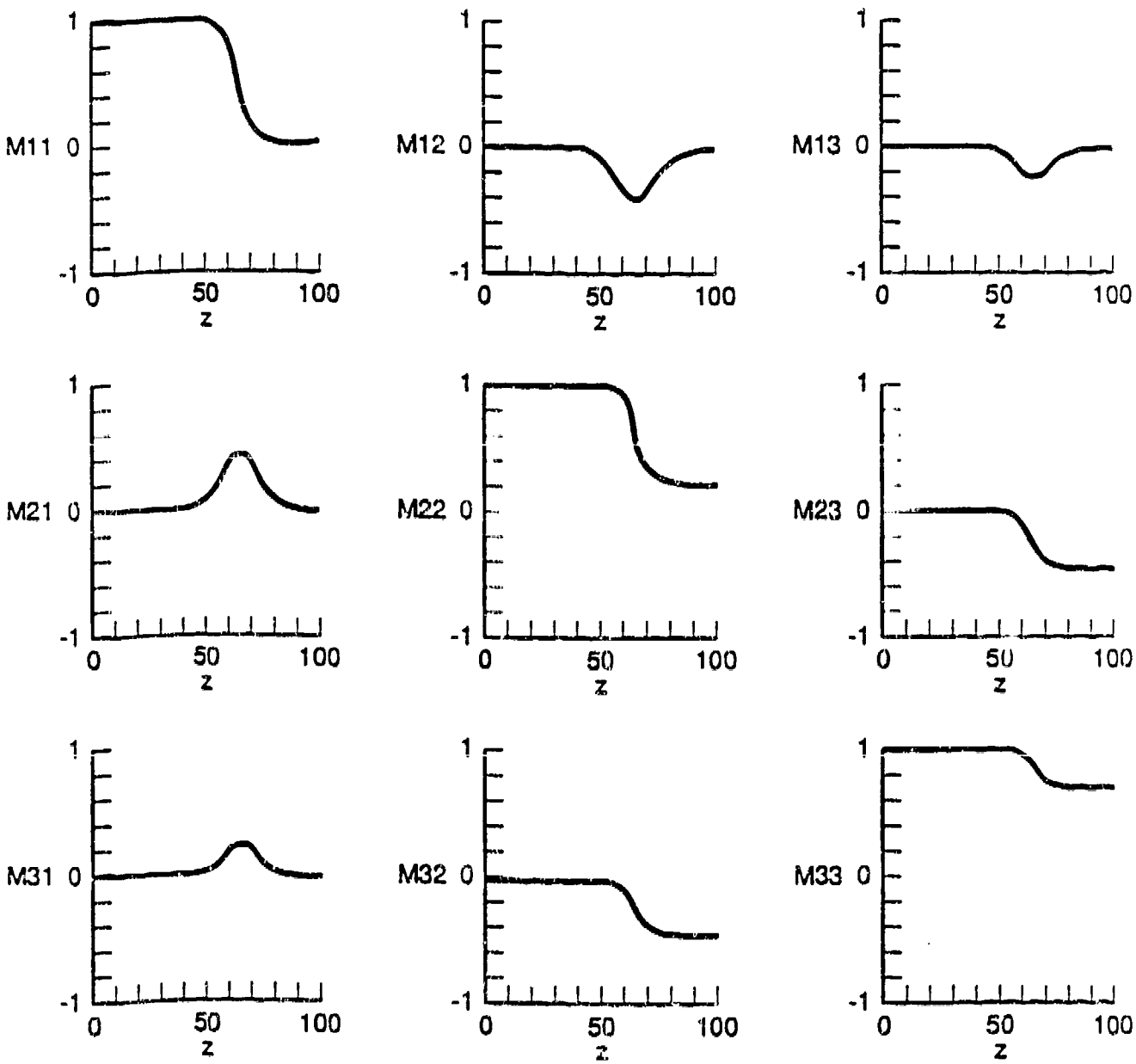

Figure 17. Elements of $\hat{M}$ as a function of altitude.

required for a mode of the waveguide to exist. This relationship is expressed, of course, in the modal equation. To do this we use reflection coefficients. A field within the wave guide will be reflected at both the top, or ionosphere, and bottom, or ground, boundaries. The reflection coefficient R expresses how these reflections occur. The requirements of a mode will then give us a relationship among the reflection coefficients that will be a form of the modal equation.

To find the fields in an anisotropic layer, we will follow Budden [1964] and introduce a vector $\vec{v}$ whose four components are four independent fields in the layer; this will lead to a simple matrix form for Maxwell's equations. To do this, note that if we eliminate E_z from Eqs. (19) and (20) we can write:

$$\hat{T}\vec{v} = -\frac{1}{ik}\frac{\partial}{\partial z}\vec{v} \ , \tag{128}$$

where

$$\vec{v} = \begin{pmatrix} E_x \\ -E_y \\ H_y \\ H_x \end{pmatrix} \ , \tag{129}$$

and

$$\hat{T} = \begin{pmatrix} \frac{-SM_{31}}{1+M_{33}} & \frac{SM_{32}}{1+M_{33}} & 0 & \frac{C^2+M_{33}}{1+M_{33}} \\ 0 & 0 & 1 & 0 \\ \frac{M_{23}M_{31}}{1+M_{33}} - M_{21} & C^2+M_{22} - \frac{M_{23}M_{32}}{1+M_{33}} & 0 & \frac{SM_{23}}{1+M_{33}} \\ 1+M_{11} - \frac{M_{13}M_{31}}{1-M_{33}} & \frac{M_{13}M_{32}}{1+M_{33}} - M_{12} & 0 & \frac{-SM_{13}}{1+M_{33}} \end{pmatrix} . \tag{130}$$

If we write $\vec{v}(z) = \vec{v}_o \exp(-ikqz)$ then Eq. (128) becomes

$$(\hat{T} - q\hat{I})\,\vec{v}(z) = 0 \ . \tag{131}$$

For solutions to exist, it must be true that

$$\mathrm{del}(\hat{T} - q\hat{I}) = 0 \ . \tag{132}$$

This is in fact Booker's quartic equation. In general, there are four solutions for q. Two of these represent up-going waves with Im $q < 0$ and two represent down-going waves with Im $q > 0$. Since we assume that the ionosphere is a conducting half-space, there can exist no down-going waves. Thus there are only the two up-going solutions which we denote by q_i, $i = 1, 2$. This means Eq. (131) has two eigenvectors which we represent by $\vec{v}^{(i)}$:

$$\vec{v}^{(i)} = \begin{pmatrix} E_x^i \\ -E_y^i \\ H_x^i \\ H_y^i \end{pmatrix}, \quad i = 1,2 \ . \tag{133}$$

The solution of Eq. (132) for q_i and Eq. (131) for $\vec{v}^{(i)}$ is straightforward and does not concern us further. Once we find q_i and $\vec{v}^{(i)}$, we must connect the results to the other layers. To do this, we use Budden's definition of the reflection coefficient. We next consider the fields to be represented by plane waves. That is any field component can be written as a constant times exp(-ik(Sx+qz)). The value of q will depend on the layer the field is in, but Snell's law says that the fields depend on x in the same way in each layer, i.e. exp(-ikSx). We will suppress this term in the following. Thus the fields here are really just height gains times a constant.

The following notation will be used to denote the fields in the ionosphere, waveguide, and ground:

1) the four fields in the ionosphere are: $\vec{E}^{(j)}(z)$ and $\vec{H}^{(j)}(z)$, $j = 1,2$,
2) the two fields in the waveguide are: $\vec{e}(z)$ and $\vec{h}(z)$, and
3) the two fields in the ground are: $\vec{e}^{g}(z)$ and $\vec{h}^{g}(z)$.

Let $\vec{U}$ represent the up-going electric field in the wave guide, and

$$\vec{U} = \begin{pmatrix} e_{\parallel}^{U} \\ e_{\perp}^{U} \end{pmatrix} . \tag{134}$$

Here we resolve the wave into a component that is perpendicular to the x-z plane $\vec{e}_{\perp}^{U}$, (recall that this plane contains the wave normal), and a component in the x-z plane, $\vec{e}_{\parallel}^{U}$. And, similarly, let

$$\vec{D} = \begin{pmatrix} e_{\parallel}^{D} \\ e_{\perp}^{D} \end{pmatrix} . \tag{135}$$

We define the reflection coefficient of the ionosphere ($\hat{R}^{ion}$) such that, at $z = h$,

$$\vec{D} = \hat{R}^{ion}\, \vec{U} \tag{136}$$

and

$$\hat{R}^{ion} = \begin{pmatrix} {}_{\parallel}R_{\parallel}^{ion} & {}_{\parallel}R_{\perp}^{ion} \\ {}_{\perp}R_{\parallel}^{ion} & {}_{\perp}R_{\perp}^{ion} \end{pmatrix} . \tag{137}$$

(In the following, we drop the superscript ion when there is no possibility of confusion.) Note that

$$\vec{e}_{\parallel} = \vec{e}_x + \vec{e}_z \ , \tag{138}$$

$$\vec{e}_{\perp} = \vec{e}_y \ , \tag{139}$$

and that the total field is the sum of the up- and down-going fields. Consider Fig. 18 which shows a plane wave incident on the ionosphere from below at an angle θ, and its reflected wave. Since we have a plane wave, it is easy to show that $e_{\parallel} = h_y$. Thus,

$$e_x = - \frac{1}{ik} \frac{\partial}{\partial z} h_y = - \frac{i}{ik} \frac{\partial}{\partial z} h_y^o \ \exp (\pm ikCz) \ , \tag{140}$$

where the sign in the exponent depends on whether we have an up-going (-) or a down-going (+) wave. Thus we can write

$$e_x^{total} = e_x^U + e_x^D = C(e_{\parallel}^U - e_{\parallel}^D) \ , \tag{141}$$

also

$$e_y^{total} = e_y^U + e_y^D = e_{\perp}^U + e_{\perp}^D \ . \tag{142}$$

From Maxwell's equations we know

$$h_x = \frac{1}{ik} \frac{\partial}{\partial z} e_y^o \exp (\pm ikCz) \ , \tag{143}$$

so,

$$h_x^U = - Ce_y^U \ ; \quad h_x^D = Ce_y^D \ , \tag{144}$$

and

$$h_x^{total} = h_x^U + h_x^D = - e_y^U C + e_y^D C = - C(e_{\perp}^U - e_{\perp}^D) \ . \tag{145}$$

Also, we have

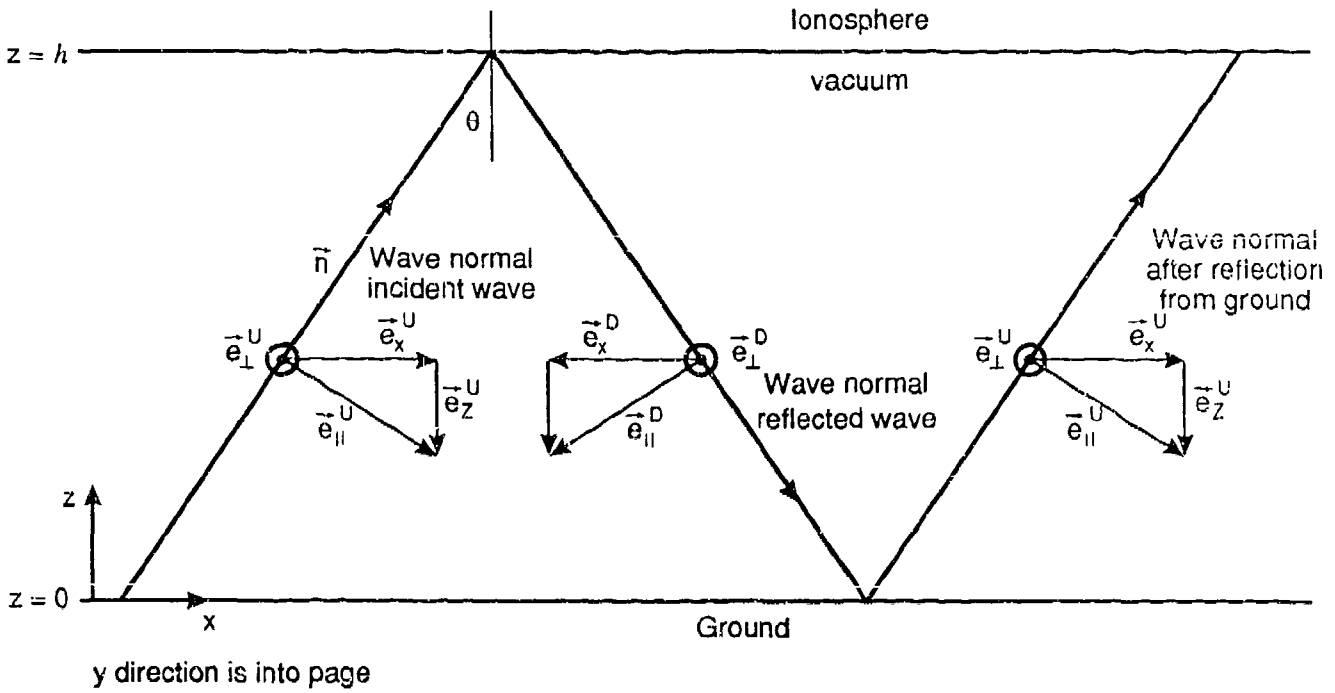

Figure 13. Plane wave incident on sharply bounded ionosphere and ground plane.

$$h_y^{total} = e_{\parallel}^{U} + e_{\parallel}^{D} \quad . \tag{146}$$

Now using Eqs. (135) and (136) we can write

$$e_{\perp}^{D} = {}_{\perp}R_{\perp}\, e_{\perp}^{U} + {}_{\perp}R_{\parallel}\, e_{\parallel}^{U} \tag{147}$$

$$e_{\parallel}^{D} = {}_{\parallel}R_{\parallel}\, e_{\parallel}^{U} + {}_{\parallel}R_{\perp}\, e_{\perp}^{U} \quad . \tag{148}$$

The boundary conditions are that e_x^{total}, e_y^{total}, h_x^{total}, h_y^{total} must be continuous at $z = h$. Thus we get at $z=h$

$$e_x^{total} = Ce_{\parallel}(1 - {}_{\parallel}R_{\parallel}) - C_{\parallel}R_{\perp}\, e_{\perp} = \kappa_1 E_x^{(1)} + \kappa_2 E_x^{(2)}, \tag{149}$$

$$e_y^{total} = e_{\perp}(1 + {}_{\perp}R_{\perp}) + {}_{\perp}R_{\parallel}\, e_{\parallel} = \kappa_1 E_y^{(1)} + \kappa_2 E_y^{(2)} \quad , \tag{150}$$

$$h_x^{total} = - Ce_{\perp}(1 - {}_{\perp}R_{\perp}) + C_{\perp}R_{\parallel}\, e_{\parallel} = \kappa_1 H_x^{(1)} + \kappa_2 H_x^{(2)} \quad , \tag{151}$$

$$h_y^{total} = e_{\parallel}(1 + {}_{\parallel}R_{\parallel}) + {}_{\parallel}R_{\perp}\, e_{\perp} = \kappa_1 H_y^{(1)} + \kappa_2 H_y^{(2)} \quad , \tag{152}$$

where the superscript U is dropped, since both $e_{\parallel}$ and $e_{\perp}$ are now only up-going. Here κ_1 and κ_2 are constants that reflect the fact that the eigenvectors are known only within an arbitrary value. We can solve this set of equations for two cases. If we let $e_{\parallel}(h) = 1$ and $e_{\perp}(h) = 0$, the results are

$${}_{\parallel}R_{\parallel}^{ion} = \frac{1}{D}\left\{\left[CE_y^{(1)} - H_x^{(1)}\right]\left[CH_y^{(2)} - E_x^{(2)}\right] - \left[CE_y^{(2)} - H_x^{(2)}\right]\left[CH_y^{(1)} - E_x^{(1)}\right]\right\} \quad , \tag{153}$$

$${}_{\perp}R_{\parallel}^{ion} = \frac{2C}{D}\left[E_y^{(1)}\, H_x^{(2)} - E_y^{(2)}\, H_x^{(1)}\right] \quad , \tag{154}$$

where the E and H field components are determined at $z = h$, and

$$D = \left[CE_y^{(1)} - H_x^{(1)}\right]\left[CH_y^{(2)} + E_x^{(2)}\right] - \left[CE_y^{(2)} - H_x^{(2)}\right]\left[CH_y^{(1)} + E_x^{(1)}\right] . \tag{155}$$

If we let $e_{\parallel}(h) = 0$ and $e_{\perp}(h) = 1$, then

$$ {}_{\perp}R_{\perp}^{ion} = \frac{1}{D}\left\{\left[CE_y^{(1)} + H_x^{(1)}\right]\left[CH_y^{(2)} + E_x^{(2)}\right] - \left[CE_y^{(2)} + H_x^{(2)}\right]\left[CH_y^{(1)} + E_x^{(1)}\right]\right\} , \tag{156}$$

$$ {}_{\parallel}R_{\perp}^{ion} = + \frac{2C}{D}\left[E_x^{(2)}\, H_y^{(1)} - E_x^{(1)}\, H_y^{(2)}\right] . \tag{157}$$

Now consider the reflection coefficient from the ground. Since the ground is isotropic, there can be no conversion for e_y to h_y and vice versa, so

$$\hat{R}^{gnd} = \begin{pmatrix} {}_{\parallel}R_{\parallel}^{gnd} & 0 \\ 0 & {}_{\perp}R_{\perp}^{gnd} \end{pmatrix} . \tag{158}$$

Reflection from the ground converts a downward-going wave into an upward-going wave, so

$$\hat{R}\vec{U} = \vec{D} . \tag{159}$$

The situation is also shown in Fig. 18. Here the fields in the waveguide at $z = 0$ are:

$$e_x^{total} = -Ce_{\parallel}^{D}\,(1 - {}_{\parallel}R_{\parallel}) , \tag{160}$$

$$e_y^{total} = e_\perp^D (1 + {}_\perp R_\perp) \ , \tag{161}$$

$$h_x^{total} = Ce_\perp^D (1 - {}_\perp R_\perp) \ , \tag{162}$$

$$h_y^{total} = e_\parallel^D (1 + {}_\parallel R_\parallel) \ . \tag{163}$$

In the ground, we know from Eqs. (63) and (74) that

$$e_y^g = \exp (ikq_g z) \ , \tag{164}$$

$$h_y^g = \exp (ikq_g z) \ , \tag{165}$$

and from Maxwell's equation we know that

$$h_x^g = \frac{1}{ik} \frac{\partial}{\partial z} e_y = q_g e_y \ , \tag{166}$$

$$e_x^g = - \frac{1}{ik} \frac{1}{n_g^2} \frac{\partial}{\partial z} h_y = - \frac{q_g}{n_g^2} h_y \ . \tag{167}$$

Thus we get at the boundary, $z = 0$ (and dropping the superscript D)

$$Ce_\perp(1 - {}_\perp R_\perp) = q_g \ , \tag{168}$$

$$e_\perp(1 + {}_\perp R_\perp) = 1 \ , \tag{169}$$

and

$$- Ce_\perp(1 - {}_\parallel R_\parallel) = - q_g/n_g^2 \ , \tag{170}$$

$$e_{\parallel}(1 + {}_{\parallel}R_{\parallel}) = 1 \ . \tag{171}$$

This gives

$${}_{\parallel}R_{\parallel}^{gnd} = \frac{C - q_g/n_g^2}{C + q_g/n_g^2} \ , \tag{172}$$

and

$${}_{\perp}R_{\perp}^{gnd} = \frac{C - q_g}{C + q_g} \ . \tag{173}$$

These are the Fresnel formulas. Note that in the case of an isotropic ionosphere, we would have equations of the same form for $\hat{R}^{ion}$.

For a mode to exist, the doubly reflected up-going field (represented on the right of Fig. 18) must be the same as the initial up-going field (on the left.) This restricts the allowed values of C and so gives the modal equation for the anisotropic case. First we write the up-going field at any location in the waveguide as:

$$\vec{U}(z) = \begin{bmatrix} h_y^U(z) \\ e_y^U(z) \end{bmatrix} = \begin{bmatrix} h_y^U(0) \\ e_y^U(0) \end{bmatrix} e^{-ikqz} \tag{174}$$

$$= \vec{U}_o e^{-ikqz} \ , \tag{175}$$

and in the same way we can write the down-going wave at any altitude as

$$\vec{D}(z) = \vec{D}_o \ e^{ikqz} \ . \tag{176}$$

Here $\vec{U}_o$ and $\vec{D}_o$ represent constant vectors, $\vec{U}_o$ is arbitrary, but $\vec{D}_o$ can be determined. We know

$$\hat{R}^{ion}\,\vec{U}(h) = \vec{D}(h) \ , \tag{177}$$

and

$$\hat{R}^{gnd}\,\vec{D}(0) = \vec{U}(0) \ . \tag{178}$$

We can write Eq. (177) as

$$\hat{R}^{ion}\,\vec{U}_o\,e^{-ikCh} = \vec{D}_o\,e^{ikCh} \ . \tag{179}$$

Multiplying both sides by $\hat{R}^{gnd}$ and using Eq. (178) yields

$$\hat{R}^{gnd}\,\hat{R}^{ion}\,\vec{U}_o\,e^{-ikCh} = \hat{R}^{gnd}\,\vec{D}_o\,e^{ikCh}$$

$$= \vec{U}_o\,e^{+ikCh} \ . \tag{180}$$

Thus we get:

$$(\hat{R}^{gnd}\,\hat{R}^{ion}\,e^{-2ikCh} - \hat{I})\,\hat{U}_o = 0 \ . \tag{181}$$

This requires

$$\det(\hat{R}^{gnd}\,\hat{R}^{ion}\,e^{-2ikCh} - \hat{I}) = 0 \ , \tag{182}$$

or

$$({}_{\parallel}R_{\parallel}^{ion}\;{}_{\parallel}R_{\parallel}^{gnd}\;e^{-2ikCh} - 1)\;({}_{\perp}R_{\perp}^{ion}\;{}_{\perp}R_{\perp}^{gnd}\;e^{-2ikCh} - 1)$$

$$- {}_{\perp}R_{\perp}^{gnd}\;{}_{\parallel}R_{\parallel}^{gnd}\;{}_{\parallel}R_{\perp}^{ion}\;{}_{\perp}R_{\parallel}^{ion}\;e^{-4ihCh} = 0 \ , \tag{183}$$

which is the anisotropic modal equation. This equation is solved quickly for C, once the parameters of the ionosphere are found from a full wave calculation in one direction. Then Eq. (183) is used to determine C, and hence the attenuation for any other direction. An example of this is given in Sec. 3. [Note that in the case of an isotropic ionosphere substitution of Eqs. (172) and (173), along with the similar forms for $\hat{R}^{ion}$, would give the TM modal equation, Eq. (77), written in slightly different form multiplied by the TE modal equation, Eq. (67).]

ANISOTROPIC HEIGHT GAIN FUNCTIONS e(z), h(z).

As in the isotropic case, e(z) and h(z) are the height functions for the transverse component of the E and H fields. Their form is

$$e(z) = \begin{cases} e_1 e^{-iq_i^{(1)}kz} + e_2 e^{-iq_i^{(2)}kz} & \text{for } z > h \ , \quad (184) \\ e_3 e^{-iCkz} + e_4 e^{iCkz} & \text{for } 0 \le z \le h \ , \quad (185) \\ e^{+iq_g kz} & \text{for } z < 0 \ . \quad (186) \end{cases}$$

and

$$h(z) = \begin{cases} h_1 e^{-iq_i^{(1)} kz} + h_2 e^{-iq_i^{(2)} kz} & \text{for } z > h \ , \quad (187) \\ h_3 e^{-iCkz} + h_4 e^{iCkz} & \text{for } 0 \le z \le h \ , \quad (188) \\ e^{iq_g kz} & \text{for } z < 0 \ . \quad (189) \end{cases}$$

where $q_i^{(1)}$, $q_i^{(2)}$ are the two solutions of the Booker quartic in the ionosphere, $q_g^2 = n_g^2 - 1 + C^2$, and the e_j and h_j, j = 1 to 4, are

constants. Note that, as in the isotropic case, we normalize both the TE and TM height gains to 1 at z = 0.

The constants, e_1, e_2, h_1, h_2 can be determined in terms of the anisotropic transmission coefficients, which are derivable from Eqs. (149) to (152). However, the height gains in the ionosphere are not needed to determine normal nighttime propagation so we do not discuss them further.

To determine the constants in the waveguide, we note that since the down-going wave is in the waveguide,

$$\vec{D} = \begin{pmatrix} h_4 \, e^{iCkz} \\ e_4 \, e^{iCkz} \end{pmatrix} . \tag{190}$$

Then we can write

$$h_4 = {}_{\parallel}R_{\parallel} \, h_3 \, e^{-2iCkh} + {}_{\parallel}R_{\perp} \, e_3 e^{-2iCkh} , \tag{191}$$

$$e_4 = {}_{\perp}R_{\parallel} \, h_3 \, e^{-2iCkh} + {}_{\perp}R_{\perp} \, e_3 e^{-2iCkh} . \tag{192}$$

We make the following equations less complex by redefining the reflection coefficients to include the exp(-2iCk*h*) term. The ionosphere reflection coefficients as defined by Eq. (136) are the ratio of fields at $z = h$. Including the exponential term defines the coefficients as ratios of fields at z = 0. Thus we can say that R^{ion} is referenced on the ground. We denote this by writing $R^{ion}(0) \equiv R^{ion}(h) \, e^{-2iCkh}$. We also know that at z = 0, we have

$$h_3 + h_4 = 1 , \tag{193}$$

$$e_3 + e_4 = 1 . \tag{194}$$

Thus we can solve Eqs. (191) to (194) to give

$$h_3 = \frac{1}{D_R}\left[1 + {}_{\perp}R_{\perp}^{ion}(0) - {}_{\parallel}R_{\perp}^{ion}(0)\right] , \tag{195}$$

$$e_3 = \frac{1}{D_R}\left[1 + {}_{\parallel}R_{\parallel}^{ion}(0) - {}_{\perp}R_{\parallel}^{ion}(0)\right] , \tag{196}$$

where

$$D_R = \left[1 + {}_{\perp}R_{\perp}^{ion}(0)\right]\left[1 + {}_{\parallel}R_{\parallel}^{ion}(0)\right] - {}_{\parallel}R_{\perp}^{ion}(0)\,{}_{\perp}R_{\parallel}^{ion}(0) \tag{197}$$

which defines the height gains wherever we need them.

APPENDIX B

LIST OF ACRONYMS

Acronym	Meaning	Page
CCIR	International Radio Consultative Committee	8
C-G	cloud-to-ground	5
DMSP	Defense Meteorological Satellite Program	11
ELF	extremely low frequency	1
FOV	field of view	17
GLO	global lightning occurrence	8
I-C	In-cloud	5
ISS	Ionosphere Sounding Satellite	17
LF	low frequency	1
OSO	Orbiting Solar Observatory	10
PSR	Pacific-Sierra Research Corp.	1
RF	radio frequency	4
RMS	root mean square	30
SI	International System of Units	53
TD	thunderstorm days	1
TE	transverse electric	2
TM	transverse magnetic	4
VLF	very low frequency	1
WGL	Westinghouse Georesearch Laboratory	1
WKB	Wentzel-Kramers-Brillouin	2
WMO	World Meteorological Organization	8

APPENDIX C

LIST OF SYMBOLS

In this appendix, we list the symbols used in the text. The page number below indicates the first page on which the symbol is used. Equation numbers are also given when a quantity is defined by an equation. Several symbols are defined in Table 3 in Appendix A, they are also indicated below.

Symbol	Description	Page
A	- area over which debris is spread (in km^2)	34
a_e	- radius of the earth	29
$A_n(x)$	- represents a generalized forward going wave in the transition region	55
$a_n(x)$	- Amplitude function of forward wave for, Eq. (39)	58
$B_n(x)$	- represents a generalized backward going wave in the transition region	55
$b_n(x)$	- an amplitude function associated with the reflected (backward going) wave, Eq. (40)	58
$C_n(x)$	- propagation parameter - cosine of the complex eigenangle for n^{th} mode.	50
D	- a denominator, Eq. (155)	86
D_R	- a denominator used to find height gains, Eq. (197)	92
$\vec{D}$	- a downgoing electric field in free space, Eq. (135)	82
$\vec{E}$, E_x, E_y, E_z	- an electric field and its components.	50
e	- charge of the electron, Table 3	53
$e_n(z)$	- TE height gain function, Eq. (62)	63

Symbol	Description	Page
e_1, e_2, e_3, e_4	- constants used to determine the height gain of E_y in the general anisotropic case, Eq. (184)-(186)	90
$\vec{F}$	- a generalized field combining either the TE (E_y, H_x, H_z) or TM field components (H_y, E_x, E_z)	50
f_c	- critical frequency (MHz)	17
$f_n(z)$	- generalized height gain function	55
$f_t(z)$	- height gain factor of the transmitter	29
$f_r(x,z)$	- height gain factor for the receiver	29
g (superscript)	- denotes a quantity in the ground	
$g_n(z)$	- a function orthogonal to the generalized height gain function f_n	56
$G_{nm}^{(j)}(x)$	- represents in some sense the energy scattered from the m^{th} to the n^{th} mode by the j^{th} order scattering process, Eq. (50)	61
$\vec{H}$, H_x, H_y, H_z	- a renormalized magnetic field and its components	50
$\vec{H}_e$	- geomagnetic field - in mks units, Table 3	53
h_o	- height of the ionosphere at start of transition zone	36
h_1, h_2, h_3, h_4	- constants used to find height gain of H_y in the general anisotropic case, Eqs. (187)-(189)	90
$h(x)$	- height of the ionosphere at position x	36
$h_n(z)$	- TM height gain function, Eq. (72)	65
$\hat{I}$	- the identity matrix	52
i (superscript)	- denotes an ionospheric quantity	
k	- the wave number = 2π/wavelength	54
$K_{nm}(x)$	- a function that expresses the amount of mode coupling, Eq. (36)	57

Symbol	Description	Page
l	- a direction cosine of the geomagnetic field, Eq.(12)	50
$\hat{M}$	- the susceptibility matrix - a 3×3 matrix, Eq.(17)	52
m	- mass of electron, Table 3	53
m	- a direction cosine of the geomagnetic field, Eq.(13)	50
m (subscript)	- indicates the m^{th} mode	
M_G	- land/ocean modification factor	26
M_E	- terrain elevation modification factor	26
M_L	- latitude source modification factor	26
M_S	- storm severity modification factor	26
N	- electron number density ($1/m^3$), Table 3	53
$\vec{n}$	- wave normal, see Fig. 16	51
n	- a direction cosine of the geomagnetic field, Eq. (14)	50
n (subscript)	- mode number, Eq. (18)	54
N_c	- flashes per unit area and time for in-cloud lightning	23
N_g	- flashes per unit area and time for cloud-to-ground lightning	23
n^2, n_g^2, n_i^2	- the square of the index of refraction, in general, in the earth, or in the ionosphere for the isotropic case.	52
$N_{\ell d}$	- Number of lightning discharges/km^2-month	10
N_{TD}	- Number of thunderstorm days/month	10
o (superscript)	- denotes a quantity in free space	
P	- radiated power	29
∥ (subscript)	- indicates a component parallel to the x-z plane	82

Symbol	Description	Page
$\perp$ (subscript)	- indicates a component perpendicular to x-z plane	82
$Q_n(x)$	- the total mode-coupling factor, Eq. (7)	32
$Q_n^{(j)}(x)$	- the mode-coupling scattering factor, Eq. (59)	62
$Q_{nm}^{(j)}(x)$	- represents j^{th} order scattering of energy from n^{th} to m^{th} mode	32
$Q_{nn}^{(j+1)}(x)$	- represents energy scattered back into the n^{th} mode from all other modes, for j^{th} order scattering	32
q	- the Booker quartic, $q^2 = n^2 - 1 + C^2$ in an isotropic region	56
$\hat{R}$, $\hat{R}^{ion}$, $\hat{R}^{gnd}$	- the reflection coefficient matrix (a 2 × 2 matrix), Eq. (136)	82
$_{\parallel}R_{\parallel}$, $_{\parallel}R_{\perp}$, $_{\perp}R_{\parallel}$, $_{\perp}R_{\perp}$	- elements of the reflection coefficient matrix, Eq. (137)	82
R_n	- reflection factor for n^{th} mode, indicates the amount of reflection of a wave from a region of changing propagation conditions.	55
$S_n(x)$	- the complex sine of the eigenangle for the n^{th} mode	29
t	- time in seconds	34
$\hat{T}$	- 4 x 4 matrix, which expresses Maxwell's equations in an anisotropic region, Eq. (130)	80
U	- magneto-ionic parameter, Table 3	53
$\vec{U}$	- an upgoing electric field in free space, Eq. (134)	82
$\vec{v}$	- generalized field 4-vector, Eq. (128)	80
W	- measure of the ionizing intensity of nuclear debris, Eq. (8)	34
X	- magneto-ionic parameter, Table 3	53
x	- distance along the direction of propagation	52

Symbol	Description	Page
Y	- magneto-ionic parameter, Table 3	53
y	- renormalized magneto-ionic parameter, Eq. (11)	45
Y_F	- fission yield in megatons	34
Z	- magneto-ionic parameter, Table 3	53
z	- altitude	54
Z_0	- characteristic impedance of free space	53
Z_i, Z_g	- dimensionless impedance for the ionosphere and ground respectively	63
$\alpha_n(x)$	- an excitation function, Eq. (44)	59
β	- the Wait and Spies inverse scale height parameter used in exponential ionosphere models as $\exp(\beta(z-h'))$.	43
Γ_n	- value of the forward moving wave on ground i.e., the excitation factor	55
Γ_t, Γ_r	- excitation factors	29
$\gamma_{mn}(x)$	- a cross coupling function, Eq. (46)	60
Δh	- Change in ionosphere height	37
Δx	- length of transition zone	37
δ	- geomagnetic field dip angle	50
δ_{nm}	- the delta function, $\delta_{nm} = 1$ if $n = m$, else $\delta_{nm} = 0$	56
$\vec{\nabla}$	- the gradient	
$\vec{\nabla}\cdot$	- the divergence	
$\vec{\nabla}\times$	- the curl	
ϵ_0	- electric permittivity of free space, Table 3	53
ϵ_r	- relative permittivity of the ground, Eq. (15)	52

Symbol	Description	Page
ζ	- ratio of in-cloud to cloud-to-ground flashes, Eq. (5)	26
θ	- angle wave normal makes with the vertical, i.e. angle of incidence	50
κ	- a constant,	29
κ_1, κ_2	- constants	85
λ	- latitude in degrees (north latitudes are positive, south, are negative)	23
$\Lambda_n(x)$	- a normalizing function, Eq.(30)	56
μ_0	- magnetic permeability of free space, Table 3	53
Ξ	- $C^2(n^2 + 1) - 1$	70
ν	- electron collision frequency 1/s, Table 3	53
σ_i, σ_g	- the conductivity of the ionosphere and the ground	52
τ	- an integration variable, Eq. (48)	
ϕ	- azimuth of propagation	50
χ	- integration variable, used to denote distance along the propagation direction	
$\Omega_n(x)$	- attenuation function	29
ω	- $2\pi \times$ frequency	53
ω_g	- gyro frequency $\approx 9.3 \times 10^6$ s^{-1}	77
(1),(2) (superscripts)	- denotes quantities associated with one of the two upward-going fields in an anisotropic ionosphere	

DISTRIBUTION LIST

DNA-TR-88-239-V1

DEPARTMENT OF DEFENSE

DEFENSE COMMUNICATIONS AGENCY
ATTN: A310 P CROWLEY
ATTN: A320 C STANSBERRY
ATTN: A320 W SHERMAN

DEFENSE INTELLIGENCE AGENCY
ATTN: RTS-2B

DEFENSE NUCLEAR AGENCY
3 CYS ATTN: RAAE
4 CYS ATTN: TITL

DEFENSE TECHNICAL INFORMATION CENTER
12CYS ATTN: DTIC/FDAB

DEPARTMENT OF THE NAVY

NAVAL OCEAN SYSTEMS CENTER
ATTN: CODE 542, F SNYDER
ATTN: CODE 542, J FERGUSON

NAVAL RESEARCH LABORATORY
ATTN: CODE 4193 F KELLY

NAVAL UNDERWATER SYSTEMS CENTER
ATTN: CODE 3411, J KATAN

DEPARTMENT OF THE AIR FORCE

AIR FORCE ELECTRONIC WARFARE CENTER
ATTN: LT M MCNEELY

AIR UNIVERSITY LIBRARY
ATTN: AUL-LSE

ROME AIR DEVELOPMENT CENTER, AFSC
ATTN: EEAA J TURTLE

WEAPONS LABORATORY
ATTN: NTAAB
ATTN: SUL

DEPARTMENT OF ENERGY

SANDIA NATIONAL LABORATORIES
ATTN: TECH LIB 3141

DEPARTMENT OF DEFENSE CONTRACTORS

JOHNS HOPKINS UNIVERSITY
4 CYS ATTN: R LUNNEN

KAMAN SCIENCES CORPORATION
ATTN: B GAMBILL
ATTN: DASIAC
ATTN: R RUTHERFORD

KAMAN SCIENCES CORPORATION
ATTN: DASIAC

MISSION RESEARCH CORP
ATTN: TECH LIBRARY

MITRE CORPORATION
ATTN: C SMITH, III
ATTN: J VALIGA

PACIFIC-SIERRA RESEARCH CORP
2 CYS ATTN: C WARBER
2 CYS ATTN: E FIELD JR
ATTN: H BRODE, CHAIRMAN
2 CYS ATTN: L KIES

R & D ASSOCIATES
ATTN: C GREIFINGER

RAND CORP
ATTN: C CRAIN

SCIENCE APPLICATIONS INTL CORP
ATTN: G-5-2, E MCKAY

STANFORD UNIVERSITY
ATTN: A FRASER-SMITH
ATTN: U INAN

TELECOMMUNICATION SCIENCE ASSOCIATES
ATTN: R BUCKNER